

# **Droplet Interface Bilayers: Microfluidic methods to model pharmacokinetics in artificial cell membranes**

by

**Elanna B. Stephenson**  
**B.Sc., University of Alberta, 2015**

A dissertation submitted in partial fulfillment of the  
requirements for the degree of

**DOCTOR OF PHILOSOPHY**

in the Department of Chemistry

©Elanna B. Stephenson, 2021  
University of Victoria

This work is licensed under a Creative Commons Attribution-  
NonCommercial 4.0 International License (CC BY-NC 4.0)



We acknowledge and respect the łək'wəḡən peoples on whose traditional territory the university stands, and the Songhees, Esquimalt and ƳSÁNEĆ peoples whose historical relationships with the land continue to this day.

# **Droplet Interface Bilayers: Microfluidic methods to model pharmacokinetics in artificial cell membranes**

by

Elanna B. Stephenson

B.Sc., University of Alberta, 2015

## **Supervisory committee**

Dr. Katherine Elvira, Supervisor

Department of Chemistry

Dr. Cornelia Bohne, Departmental Member

Department of Chemistry

Dr. Martin Boulanger, Outside Member

Department of Biochemistry



# Abstract

Modern drug development is an astronomically expensive and time consuming undertaking. Because of this, studying the pharmacokinetic properties of drugs *in vitro* has become an integral step early in the process of drug development, with the goal of preventing costly failures late in the process, and dangerous side effects. Artificial phospholipid bilayers known as droplet interface bilayers (DIBs) have the potential to be used for these pharmacokinetics assays, combining the low cost of cell-free assays with the ability to more closely mimic structures found in life than current cell-free *in vitro* techniques. Combined with the reproducibility, ease of use, and low reagent consumption found with microfluidic methods, disruptive new low cost techniques for assessing pharmacokinetics in drug development may be possible using DIBs as an artificial cell membrane model.

In this work, I establish the potential of DIBs to be used as a pharmacokinetics modelling platform, and advance the use of microfluidic methods for carrying out pharmacokinetics assays in drug discovery. I first developed a new microfluidic platform for the formation of DIBs, which sought to solve some of the shortcomings of

current microfluidic methods for DIB formation (Chapter 2). This device is the first that can be used to form DIB networks from dissimilar droplets in parallel, without use of active controls, and with droplet contact gentle enough to enable use of biomimetic lipid mixtures. I examine for the first time the behaviour of phospholipids on microfluidic devices, and characterise the interaction that they have with a common material used to construct microfluidic devices (Chapter 3). Not only has this interaction never been studied before, but my unexpected findings indicate a new area requiring further study in order to advance the adoption of DIBs on microfluidic devices. In collaboration with my colleague Jaime Korner, I use my newly developed microfluidic platform to carry out an on-chip permeation assay for the first time using biomimetic lipid formulations and bespoke compartments modelled after the human intestine. We demonstrate that this on-chip assay has predictive accuracy greater than that of a current widely used cell-free technique (Chapter 4). Finally, I demonstrate that a DIB based microfluidic platform enables, and is critical for, characterising the effect of structural features such as membrane asymmetry on drug permeation. With this, I find measurable, previously unknown effects of membrane asymmetry on the absorption of the chemotherapy drug doxorubicin, highlighting a possible contributing factor to chemoresistance in some cancers (Chapter 5). I find, and demonstrate throughout the body of this work that microfluidic methods and DIBs can not only provide alternatives to current cell-free *in vitro* pharmacokinetics assays, but that they can exceed the performance of existing assays, and be used for entirely new ways of examining pharmacokinetics. Through building bespoke artificial cell membranes from the ground up, I hope to demonstrate herein the great potential of these powerful

new cell-free methods.

# Contents

<b>Supervisory committee</b>	<b>ii</b>
<b>Abstract</b>	<b>iii</b>
<b>Contents</b>	<b>vi</b>
<b>List of Tables</b>	<b>xiii</b>
<b>List of Figures</b>	<b>xiv</b>
<b>Acknowledgements</b>	<b>xix</b>
<b>1 Introduction</b>	<b>1</b>
1.1 Pharmacokinetics and drug discovery . . . . .	2

---

1.2	Artificial membranes for pharmacokinetics . . . . .	5
1.3	Droplet interface bilayers (DIBs) as model artificial membranes . . . .	10
1.4	Droplet microfluidics: a versatile tool for DIB formation . . . . .	13
1.5	Research motivation . . . . .	19
<b>2</b>	<b>Design of a microfluidic platform for DIB formation</b>	<b>21</b>
2.1	Microfluidic methods for DIB formation . . . . .	22
2.2	Layered devices: DIB formation on a rail . . . . .	27
2.3	Droplet steering, control, and alternating droplets . . . . .	30
2.4	Parallel rails: a new approach to DIB formation . . . . .	37
2.5	Experimental details . . . . .	40
2.5.1	Materials . . . . .	40
2.5.2	Device fabrication and solution preparation . . . . .	41
2.5.3	Operation of devices utilising syringe pumps . . . . .	41
2.5.4	Operation of devices utilising syringe pumps . . . . .	42
<b>3</b>	<b>Phospholipids facilitate water adsorption and failure of surface properties</b>	

<b>on PDMS microfluidic devices</b>	<b>44</b>
3.1 Introduction . . . . .	45
3.2 Materials and methods . . . . .	52
3.2.1 Microfluidic device fabrication . . . . .	52
3.2.2 Equipment for <i>in situ</i> experiments . . . . .	52
3.2.3 Contact angle measurements . . . . .	53
3.2.4 Interfacial tension measurements . . . . .	53
3.2.5 Fluid dynamics simulations with COMSOL® . . . . .	54
3.2.6 Droplet length experiments . . . . .	57
3.2.7 Time-resolved surface properties experiments . . . . .	60
3.3 Results and discussion . . . . .	61
3.3.1 Phospholipids do not assemble at the fluid interface fast enough to impact droplet formation . . . . .	61
3.3.2 Establishment of a visual means to quantify contact angle <i>in situ</i>	68
3.3.3 Lipid containing solutions exhibit enhanced wetting . . . . .	71
3.4 Future work . . . . .	75

3.5	Notes and acknowledgements . . . . .	76
<b>4</b>	<b>A bespoke microfluidic pharmacokinetic compartment model for drug absorption using artificial cell membranes</b>	<b>77</b>
4.1	Abstract . . . . .	78
4.2	Introduction . . . . .	79
4.3	Materials and methods . . . . .	86
4.3.1	Materials . . . . .	86
4.3.2	Design and fabrication of the microfluidic platform . . . . .	87
4.3.3	Preparation of lipid solutions . . . . .	88
4.3.4	Operating parameters of the microfluidic platform . . . . .	89
4.3.5	Fluorescence data collection . . . . .	90
4.3.6	Quantification of microfluidic device performance . . . . .	91
4.4	Results and discussion . . . . .	92
4.4.1	A new <i>in vitro</i> model for intestinal absorption . . . . .	92
4.4.2	Correlation to cell-based assays . . . . .	97
4.4.3	Control experiments . . . . .	98

---

4.5	Conclusions . . . . .	100
4.6	Conflicts of interest . . . . .	102
4.7	Acknowledgements . . . . .	102
<b>5</b>	<b>Biomimetic artificial cells to model the effect of membrane asymmetry on chemoresistance</b>	<b>103</b>
5.1	Abstract . . . . .	104
5.2	Introduction . . . . .	105
5.3	Experimental . . . . .	108
5.4	Results and discussion . . . . .	110
5.5	Conclusions . . . . .	115
5.6	Conflicts of interest . . . . .	116
<b>6</b>	<b>Conclusions and future work</b>	<b>117</b>
	<b>References</b>	<b>121</b>
	<b>Appendices</b>	<b>165</b>



**Appendix A Droplet Interface Bilayers: How can they achieve their full potential? 166**

A.1 Abstract . . . . .	167
A.2 Introduction . . . . .	167
A.3 Designing and building DIBs as biomimetic model membranes . . . . .	171
A.4 DIBs to quantify molecular kinetics . . . . .	177
A.5 DIBs to study integral membrane proteins . . . . .	180
A.6 DIBs as scaffolds for electrophysiological measurements . . . . .	184
A.7 The future and potential of DIBs . . . . .	187
A.8 Funding . . . . .	192

**Appendix B Electronic Supplementary Information: A bespoke microfluidic pharmacokinetic compartment model for drug absorption using artificial cell membranes 193**

B.1 Fluorescence measurements and data normalisation . . . . .	195
B.2 Calibration curves . . . . .	197
B.3 Control experiments . . . . .	201

B.4 Heating platform . . . . .	202
B.5 Video of device operation . . . . .	205

**Appendix C Electronic Supplementary Information: Biomimetic artificial  
cells to model the effect of membrane asymmetry on chemoresistance 207**

C.1 Materials and methods . . . . .	210
C.2 Droplet and bilayer size measurements . . . . .	210
C.3 Time lapses of bilayer curvature . . . . .	214
C.4 Original fluorescence images . . . . .	219
C.5 Fluorescence intensity measurements and flux calculations . . . . .	221
C.6 Acknowledgements . . . . .	223

# List of Tables

3.1	Interfacial tensions used in the COMSOL <sup>®</sup> model. . . . .	58
4.1	Composition of the buffers used for each pharmacokinetic compartment. . . . .	89
4.2	Statistical data used to quantify device performance. . . . .	92
C.1	Detailed compositions of lipid formulations. . . . .	209
C.2	Interfacial tension data for lipid solutions. . . . .	216

# List of Figures

1.1	<b><i>In-vitro</i> pharmacokinetic models relevant to this work.</b>	3
1.2	<b>Common artificial membrane models.</b>	7
1.3	<b>Process of DIB formation.</b>	11
1.4	<b>Device geometries used for droplet formation in droplet microfluidics.</b>	16
1.5	<b>Breakdown of trends in the field of DIBs by year.</b>	18
2.1	<b>Literature examples of microfluidic DIB formation.</b>	24
2.2	<b>Chamber broadening devices.</b>	28
2.3	<b>Branching rail based devices.</b>	29
2.4	<b>Flow rate manipulation for droplet control.</b>	31

2.5	Formation and trapping of alternating droplets. . . . .	33
2.6	Alternating droplets formed using a pressure pump. . . . .	35
2.7	Parallel rail based DIB formation. . . . .	38
3.1	Operation and failure modes of a T-junction. . . . .	50
3.2	Graphical representation of COMSOL <sup>®</sup> model, and key dimensions. . . . .	51
3.3	Derivation of formula for device contact angle from Young's equation. . . . .	56
3.4	Results of droplet length experiments. . . . .	62
3.5	Calibration curve for <i>in situ</i> contact angle determination. . . . .	69
3.6	The effect of lipid presence on device longevity. . . . .	72
4.1	A new type of pharmacokinetic compartment model. . . . .	80
4.2	Design of the "slow microfluidic" platform for the formation of ABC droplet triplets. . . . .	82
4.3	Images of fluorophore diffusion. . . . .	93
4.4	Fluorophore diffusion over time. . . . .	94
4.5	Fluorophore absorption over time. . . . .	95

4.6	<b>Fluorophore flux over time. . . . .</b>	96
5.1	<b>Design of the microfluidic platform, and DIB formation process. . .</b>	107
5.2	<b>Relative curvature of asymmetric, blend, and symmetric DIBs. . .</b>	112
5.3	<b>Diffusion of DOX across asymmetric, blend and symmetric bilayers is shown over time. . . . .</b>	113
5.4	<b>Flux of DOX over time for asymmetric, blend and symmetric DIBs.</b>	115
A.1	<b>DIBs in relation to other artificial membranes, their shape, and on-chip formation methods . . . . .</b>	170
A.2	<b>Literature applications of fluorescence in DIBs. . . . .</b>	181
A.3	<b>Literature examples of DIB formation using automation. . . . .</b>	191
B.1	<b>Fluorescence intensity measurements. . . . .</b>	195
B.2	<b>Artificial cell membrane surface area calculations. . . . .</b>	196
B.3	<b>Droplet volume calculations. . . . .</b>	197
B.4	<b>Calibration curve for fluorescein in the intestinal space compartment buffer. . . . .</b>	198

B.5	Calibration curve for fluorescein in the enterocyte compartment buffer. . . . .	199
B.6	Calibration curve for fluorescein in the blood compartment buffer.	200
B.7	Control experiments. . . . .	201
B.8	Three-dimensional constructed (left) and exploded (right) view of the heating platform. . . . .	203
B.9	Thermal camera images of the heating platform containing a microfluidic device both when the platform is covered (left) and uncovered (right). . . . .	204
B.10	Heating platform temperature readings. . . . .	205
C.1	Chemical structures of compounds used. . . . .	208
C.2	Relative curvature measurements. . . . .	211
C.3	Bilayer size measurements. . . . .	212
C.4	Droplet volume measurements. . . . .	213
C.5	Evolution of asymmetric bilayer curvature over time. . . . .	214
C.6	Evolution of blend bilayer curvature over time. . . . .	214
C.7	Evolution of symmetric bilayer curvature over time. . . . .	215

---

<b>C.8 Effect of SM on bilayer curvature. . . . .</b>	<b>217</b>
<b>C.9 Relationship between interfacial tension and SM concentration. .</b>	<b>218</b>
<b>C.10 RGB images for the asymmetric bilayers shown in Figure 5.3. . . .</b>	<b>219</b>
<b>C.11 RGB images for blend bilayers shown in Figure 5.3. . . . .</b>	<b>219</b>
<b>C.12 RGB images for symmetric bilayers shown in Figure 5.3. . . . .</b>	<b>220</b>
<b>C.13 Original RGB images for expansions shown in Figure 5.3. . . . .</b>	<b>220</b>



# Acknowledgements

When I first started my master's degree four years ago, I did not anticipate that I would be here, now, preparing to defend my PhD. It has been quite the journey getting here, through all of the ups and downs, and a year long ordeal that shall remain nameless started by a bat that had a sniffle. I owe a lot of the successes in getting here to many, many people in my life. First of all, I would like to thank my supervisor Katherine, both for giving me the chance to be here, and for being an all around fantastic supervisor and mentor. Having your mentorship and guidance throughout the past few years hasn't just enabled the work to happen, but you've also enriched my education and gone above and beyond to set me on the path to a rewarding career. Thank you as well to everyone who has come and gone from the group over the years (far too many to list!), but I would especially like to thank Kaitlyn, Jaime, and Alejandro. You've been more than coworkers and colleagues, you've been good friends, and you've made the day to day a lot more fun than it would have been otherwise! I would like to thank my friend, roommate, landlord, and personal Dota 2 coach Ryan. You've been a fantastic enabler of all kinds of bicycle related suffering in my off hours, and have made home

feel like home. You, as well as Don and Mary Lynne gave me the chance to even be here in Victoria and for that I am very grateful. Thank you to my Mom, my Dad, and to my sister Kelsey for their support throughout the past few years, and for reading every manuscript that I sent your way, no matter how befuddling it might have been! And finally, thank you to my wife Alex, not just for your endless support and encouragement, but for the seemingly infinite patience you've had through all of these busy weeks and late nights. All of you haven't just made this work possible, but have made the past four years something special. I dedicate this work to all of you, thank you for everything, and thank you for the memories.

# Chapter 1

## Introduction

This chapter presents the background material informing the direction of the work contained herein, as well as the motivation for my research. Presented are a high level summary of the field of pharmacokinetics and relevant drug discovery methods, artificial membrane systems currently in widespread use, and an introduction to the fields of droplet microfluidics and droplet interface bilayers (DIBs). DIBs are becoming an increasingly varied field as they emerge as a new type of artificial bilayer. For this reason I have included a far more detailed perspective review written collaboratively with my colleague, Jaime Korner, and my supervisor, Katherine Elvira in Appendix A, describing recent advances in the DIB field. This has been submitted to Nature Chemistry (revisions submitted on July 7, 2021).

## 1.1 Pharmacokinetics and drug discovery

Drug development is an incredibly costly and time consuming process. Typical modern drug development timelines exceed 10 years.<sup>1,2</sup> Furthermore, by averaging the total development cost of a sample of compounds over those eventually receiving approval, capitalized R&D cost per approved drug can be estimated at \$2558 million (2013 US dollars).<sup>1</sup> The United States Food and Drug Administration (FDA) describes three key steps for drug development before applying for FDA approval, these being discovery and development (step 1), preclinical research (step 2), and clinical research (step 3, itself divided into phase I, II and III clinical trials).<sup>3</sup> By examining the ratio of pre-human (step 1 and 2) to total R&D costs, DiMasi *et al.* estimate a pre-human capitalized cost per approved compound of \$1098 million.<sup>1</sup> Because of this, failures late in the drug development pipeline can be extremely costly.

Pharmacology, or the study of drugs, is divided into two primary branches: pharmacodynamics, and pharmacokinetics. Pharmacodynamics is concerned with studying the effect that a drug has on the body, and searching for druggable targets which may be used to treat a clinical condition. Conversely, pharmacokinetics refers to the effects of the body on a drug, its absorption, distribution, metabolism and excretion (ADME),<sup>4</sup> and potentially toxic effects resulting from this. Prior to the introduction of screening for undesirable ADME properties early in the drug discovery process, unsafe pharmacokinetics or inability of a drug to reach its target was a common source of failures late in the drug development pipeline.<sup>5</sup> For example, interactions with drug transporters, proteins responsible for uptake and efflux of drugs, may lead to danger-

ous drug-drug interactions if not detected before clinical trials.<sup>6</sup> Poor absorption from the gastrointestinal tract, or failure to cross the blood brain barrier may also lead a drug effective *in vitro* or tested by direct injection in animal models being rendered ineffective in the clinic.<sup>5</sup> An extremely effective drug from a pharmacodynamics perspective may be considered entirely useless if it cannot reach its target under real-world conditions.

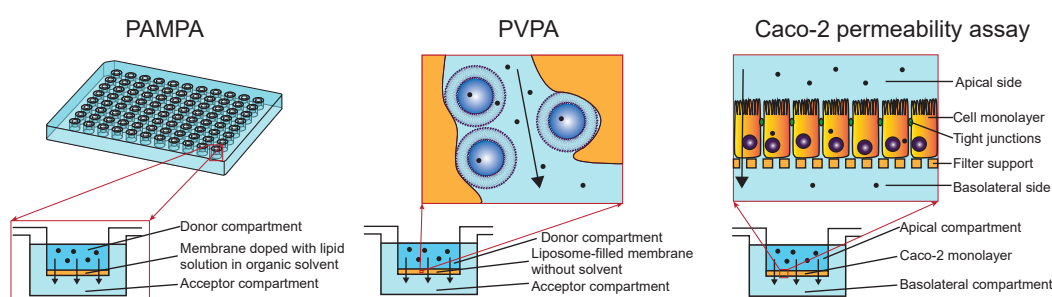


Figure 1.1: ***In-vitro* pharmacokinetic models relevant to this work.** The pharmacokinetic models shown are typically run in 96 well plates, with a second set of wells above which function as the donor compartment. In the case of PAMPA, the two sides are separated from each other by a membrane saturated with a solution of lipids in organic solvent. In the case of PVPA, the membrane is instead loaded with liposomes which become trapped within the membrane. In a Caco-2 permeability assay, a cell monolayer is grown on the filter support, and serves as an analog to the cells of the intestinal lining. The apical side is analogous to the interior of the intestinal space, and the basolateral side analogous to the tissues below the intestinal epithelial cells.

Numerous cell-free and cell-based methods have been developed for screening the pharmacokinetic properties of drugs *in vitro* early in development.<sup>7–9</sup> *In vitro* studies are attractive due to their relatively high throughput as compared with *ex vivo* or *in vivo* tests in animals, and their considerably lower associated cost. Because of this, they are useful in the early stages of drug discovery, where *ex vivo* or *in vivo*

methods would be cost prohibitive.<sup>3</sup> The methods relevant to this work are parallel artificial membrane permeation assays (PAMPA),<sup>10</sup> phospholipid vesicle-based permeation assays (PVPA),<sup>11</sup> and Caco-2 permeability assays.<sup>12</sup> See Figure 1.1 for a graphical depiction of each method. In PAMPA, an artificial filter support (polymer membrane) is doped with phospholipids dissolved in an organic solvent such as dodecane, and is used to separate a donor compartment from an acceptor compartment in a 96 well plate. Drug is dosed in the donor compartment, and time dependent data from these wells are then used to quantify rates of drug diffusion.<sup>10</sup> PVPA, similar to PAMPA, involves loading a filter support with liposomes of phospholipids.<sup>11</sup> Unlike PAMPA, the pores of the filter support are filled with liposomes in aqueous solution using centrifugation, whereas PAMPA soaks the filter with phospholipids dissolved in solvent. PVPA generally shows somewhat better performance than PAMPA at predicting *in vivo* permeability in that it more closely correlates with those obtained using cell culture.<sup>9</sup> The presence of bilayers in the filter support loaded liposomes, as well as the absence of organic solvent drive the greater performance of PVPA relative to PAMPA. Finally, in the case of Caco-2 based assays, cells from the Caco-2 cell line are cultured on a plate in a single layer, forming a structure very similar to intestinal epithelial cells.<sup>12</sup> Diffusion and transporter-mediated efflux across this layer of cells can then be quantified.

The metric by which performance of *in vitro* assays are evaluated is *in vitro-in vivo* correlation, the degree to which results of these absorption assays correlate to real world absorption in animal models or humans. While *in vitro-in vivo* correlation with modern forms of these assays has improved with refinements made since their

discovery,<sup>9</sup> there are several shortcomings to these methods. Real cell membranes include features such as membrane asymmetry, pores, and transporters, and therefore a model that cannot include these features is simplistic, and potentially fails to predict *in vivo* absorption that is affected by these factors.<sup>13</sup> In the case of PAMPA and PVPA, there is very little structural similarity between the membrane formed and an actual cell membrane, entirely precluding inclusion of these structural features. Caco-2 permeability assays, while generally excellent analogues for the intestinal lining,<sup>14</sup> introduce many of the same shortcomings as other methods requiring cell culture. Time scales to culture cells can be long, and the cost associated with culture can be high.<sup>9</sup> Furthermore, data from cell lines can be complicated by their expression of many different kinds of membrane proteins, pores, and transporters, so isolating the precise mechanism of absorption can be difficult.<sup>8</sup> Cultured cells may also express incorrect quantities of transporters,<sup>14</sup> making their behaviour different from that encountered in real intestinal linings. Using a different cell line, such as Madin-Darby canine kidney (MDCK) cells can help improve *in-vitro in-vivo* correlation in some cases, but still presents many of the same challenges as Caco-2 cells for modelling intestinal drug absorption.<sup>14</sup>

## 1.2 Artificial membranes for pharmacokinetics

Cellular membranes are complex mixtures of phospholipids structured as a bilayer, separating the interior and exterior of a cell.<sup>15</sup> These bilayers serve as a scaffold upon

which transmembrane and membrane bound proteins reside, and as a semi-permeable barrier that allows the diffusion of small molecules such as water, oxygen, and carbon dioxide. An asymmetric distribution of phospholipids between the inner and outer leaflets is maintained by a set of proteins known as flippases and floppases.<sup>16</sup> Artificial membranes seek to artificially mimic both the structure and composition of a cellular membrane. Artificial membranes provide a possible solution to the shortcomings of contemporary cell-free and cell-based absorption assays by not only providing a true analogue for a real cellular membrane, but also by doing so without costly, time-consuming cell culture.

The two most common forms of artificial membrane in use today are planar black lipid membranes (BLMs),<sup>17</sup> and liposomes;<sup>18</sup> their structures are shown in Figure 1.2. In a BLM, a layer of phospholipids is painted over a small aperture between two aqueous compartments, in a manner similar to the thin layer of soap seen in a bubble blower wand.<sup>19</sup> BLMs have been in use for several decades, and have been used to gain insight into the behavior of several ion channels.<sup>20</sup> Liposomes are a form of artificial vesicle, a compartment of aqueous liquid enclosed by a phospholipid bilayer, which consists of at least one self contained layer, or lamella, of phospholipid bilayer.<sup>21</sup> Liposomes have achieved widespread adoption for pharmacokinetic modelling with transporters embedded in vesicles.<sup>22</sup> Lipid nanoparticles are modern engineered derivatives of liposomes, which are typically neutral at physiological pH (while liposomes are charged), and typically contain additives such as polyethylene glycol and lipids to assist with cell binding.<sup>23</sup> These modern liposome derivatives are used as drug delivery vehicles to improve the cellular absorption of chemotherapy drugs,<sup>24</sup> and for intracellular de-



livery of synthetic mRNA, such as in the Moderna and Pfizer-BioNTech COVID-19 vaccines.<sup>25,26</sup>

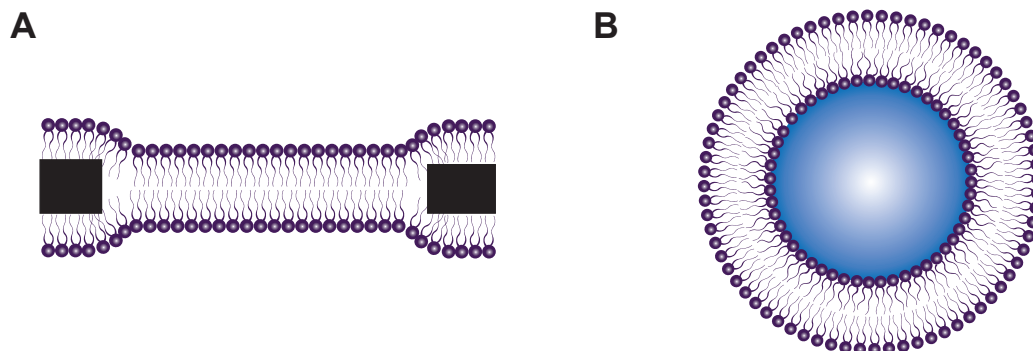


Figure 1.2: **Common artificial membrane models.** A) A black lipid membrane (BLM), also called a bilayer lipid membrane, is planar in structure, and spread across the opening of an aperture (black rectangles). Both sides of the bilayer are accessible to the experimenter. B) A liposome is a spherical structure of phospholipids enclosing an interior compartment. Only the exterior face of the liposome is accessible, preventing direct manipulation of the conditions in the interior space.

Two key concepts in relation to the pharmacokinetics of a drug are referred to throughout this work: flux ( $j$ ), and apparent permeability ( $P_{app}$ ), both of which are used to describe the phenomenon of mass transport. Flux quantifies the rate at which a given quantity of a molecule passes through a given area,<sup>27</sup> in the context of pharmacokinetics this is generally a membrane of some variety.<sup>28</sup> The equation for flux is shown in Equation 1.1, where  $I$  refers to rate of change of a quantity ( $q$ ) over time ( $t$ ), and  $A$  refers to the area of the membrane. Flux for a given compound varies in magnitude depending on the size concentration gradient, in accordance with Fick's law of diffusion.<sup>27</sup> As a result of this, flux must be normalized by concentration to give apparent permeability ( $P_{app}$ ).  $P_{app}$  quantifies the ability of a substance to cross a barrier, and allows comparisons between different substances and conditions.<sup>28</sup> The formula

for  $P_{app}$  is shown in Equation 1.2, and like flux,  $\frac{dq}{dt}$  refers to the change of quantity over time,  $A$  refers to the area of the barrier, and  $C_0$  is the initial concentration of the substance in the donor compartment. Because of this overlap in terms,  $P_{app}$  may be written in terms of flux ( $j$ ), and this is also shown in Equation 4.2.

$$\begin{aligned} j &= \frac{I}{A} \\ I &= \frac{dq}{dt} \end{aligned} \tag{1.1}$$

$$\begin{aligned} P_{app} &= \frac{dq}{dt} \times \frac{1}{AC_0} \\ P_{app} &= \frac{j}{C_0} \end{aligned} \tag{1.2}$$

Despite their widespread use, and (in the case of liposomes) broad range of applicability, these forms of artificial membrane have drawbacks that prevent their use for certain applications in pharmacokinetic analysis. BLMs are delicate, difficult to form, and tend to have short lifetimes.<sup>29</sup> This short lifetime has precluded the use of BLMs for studying membrane processes that occur over longer timescales, and the difficulty in their formation has stymied their application in higher throughput membrane formation methods like microfluidics.<sup>30</sup> Liposomes do not provide easy access to their interior space, meaning transmembrane diffusion rates must be measured through leakage of a substance previously loaded inside them. Needing to load drug into liposomes be-

fore measuring leakage means drugs that readily cross the bilayer (namely, promising drug candidates<sup>31</sup>) cannot practically be examined by this method, and it is therefore limited to studying induced leakage of an entrapped self-quenching fluorescent dye.<sup>32</sup> Self-quenching fluorescent dyes inhibit their own fluorescent emission at high concentrations, and their drop in concentration upon leakage from a liposome causes them to begin fluorescing, showing efficacy of substances designed to disrupt membrane integrity. Given that rates of diffusion across phospholipid bilayers can be influenced by curvature, the tendency towards liposomes being far smaller than the cellular scale means that they may give misleading results when used for diffusion assays.<sup>33</sup> While larger liposomes may be formed to side-step this issue, the largest liposomes typically do not exceed  $2.5\text{ }\mu\text{m}$ ,<sup>21</sup> and commercially available membranes for the formation of liposomes from one of their largest suppliers do not exceed  $1\text{ }\mu\text{m}$ .<sup>34</sup> While possible to form bilayers exhibiting asymmetry using both methods, this is non-trivial and uncommon. BLMs require careful manipulation of two separate wells of lipids, which are then painted across an aperture in a delicate process.<sup>35</sup> Asymmetric liposomes may be formed by several methods, but each carries their own caveats, either in difficulty, inability to incorporate certain features like membrane proteins, or incorporation of impurities.<sup>36</sup>

### 1.3 Droplet interface bilayers (DIBs) as model artificial membranes

Droplet interface bilayers (DIBs) are a more recent innovation for the formation of artificial phospholipid bilayers.<sup>37,38</sup> The process of DIB formation begins with at least two aqueous droplets in a bath of immiscible oil. If phospholipids are included in the aqueous phase (lipid-in), or in the oil phase (lipid-out), the amphiphilic phospholipids will behave as a surfactant, self-assembling at the surface of each droplet in a monolayer. The polar headgroups are directed towards the droplet interior, and the non-polar lipid tails face towards the oil. Once a fully assembled monolayer is formed on the droplet surfaces, the droplets can be brought together in a controlled manner, and the two monolayers will zip together to form an artificial bilayer, a DIB, separating the two aqueous compartments.<sup>30</sup> See Figure 1.3 for a graphical depiction of the process of DIB formation.

DIBs are a relatively unexplored form of artificial bilayer in comparison to BLMs and liposomes, and their application to pharmacokinetic modelling is currently in its infancy. Unlike BLMs, DIBs are easy to form, and remain stable over longer periods.<sup>30</sup> DIBs also enable easy formation of asymmetric bilayers.<sup>39</sup> DIBs have been used to demonstrate transmembrane diffusion of the fluorescent drug fluorescein,<sup>40</sup> a process reliable enough to be used for verification of DIB formation in lieu of capacitance measurements, the original method.<sup>37</sup> This common diffusion experiment demonstrates the ability DIBs to mimic the permeability characteristics of cell mem-

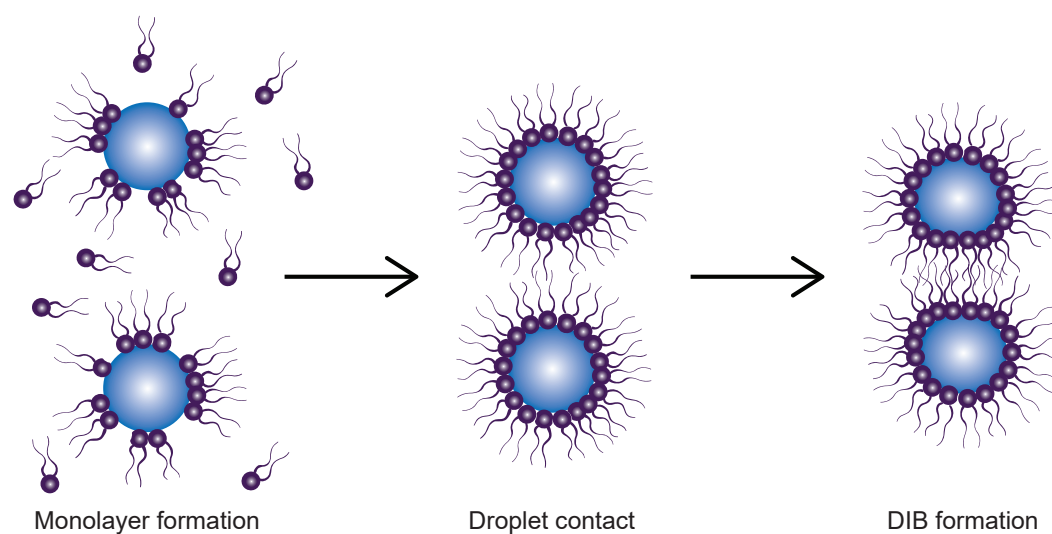


Figure 1.3: **Process of DIB formation.** DIB formation begins with a monolayer self assembling at the interface between aqueous and oil phases. Shown here, the lipids are in the surrounding oil (lipid-out), but the phospholipids may also be loaded in the aqueous phase (lipid-in). Following monolayer formation, the droplets must be brought in contact gently as to avoid droplet coalescence. Finally, the lipid tails will zip together, forming a DIB.

branes and other artificial membranes. Ultraviolet (UV)-fluorescence microscopy has also been used to observe and quantify the permeability of a DIB to caffeine,<sup>41</sup> further demonstrating that DIBs are amenable to the task of carrying out pharmacokinetic permeability assays with pharmacologically active compounds. Particularly exciting is that ATP driven active transport by bacterial lactose permease transporters has been demonstrated in a DIB, both through reconstitution of *E. Coli* expressed protein, and cell-free *in vitro* transcription and translation (IVTT) directly into the bilayer.<sup>42</sup> This work opens the door to DIB based cell-free assays of transporter activity, and hints at what the future could hold for DIBs as a pharmacokinetic tool. While these methods have mostly been limited to fluorescent compounds, more recent work has demonstrated the use of liquid chromatography mass spectrometry (LC-MS) to theoretically quantify the diffusion of any compound across a DIB.<sup>43</sup> Despite the demonstrated potential of DIBs to serve as an *in vitro* pharmacokinetic tool, these works<sup>41–43</sup> represent the only reported application of DIBs for this purpose.

Despite their usefulness, large gaps exist in our knowledge of how to make DIBs more closely resemble biological cell membranes, a necessary step for accurate pharmacokinetic assays. While natural membranes consist of complex mixtures of several phospholipid types, the vast majority of DIB literature makes use of the synthetic phospholipids 1,2-dioleoyl-sn-glycero-3-phosphocholine (DOPC), and 1,2-diphytanoyl-sn-glycero-3-phosphocholine (DPhPC). With membrane permeability relying heavily on their composition,<sup>44</sup> more biomimetic mixtures of lipids are needed to provide good *in vitro-in vivo* correlation. The lack of work using biomimetic lipids has been cited as one of the key weaknesses holding back widespread adoption of

DIBs.<sup>45</sup> Furthermore, no examples of asymmetric bilayers composed entirely of naturally derived lipids have been previously reported in the literature, meaning the effect of asymmetry on membrane permeability cannot be accounted for. It is also worth noting that DIBs have only been used for studying pharmacokinetics of a handful of compounds, with fluorescein comprising the majority of papers studying diffusion across a DIB. Perhaps the greatest obstacle towards widespread adoption of DIB based methods however, is the low throughput of traditional DIB formation methods.<sup>36</sup> In these traditional methods, DIBs are formed by contacting droplets in an oil bath using micromanipulators,<sup>38</sup> a highly skill dependant process which can take minutes for each DIB. Further information on the field surrounding DIBs may be found in Appendix A, a collaborative perspective review which has been submitted to Nature Chemistry.

## **1.4 Droplet microfluidics: a versatile tool for DIB formation**

Microfluidic lab-on-a-chip technologies provide the ideal solution to the greatest obstacles preventing widespread adoption of DIBs. For DIBs to become a more widely used form of artificial bilayer, they must be formed in a reproducible fashion as fast as possible, and not require the relatively high level of skill inherent in the use of micromanipulators. Microfluidics refers to the study of quantities of fluid on scales measured in micrometres. Devices produced in our laboratory typically have chan-

nels (structures resembling pipes in which fluids are pumped) with dimensions around 100  $\mu\text{m}$ , the width of a human hair. When working with liquids on these scales, the interplay of viscosity, density and dimensions of the channel means fluid flow takes place exclusively in the laminar regime.<sup>46</sup>

The interplay of forces in a microfluidic channel can be described using the Reynolds number ( $Re$ ), a dimensionless value describing the ratio of inertial to viscous forces, which can be calculated as shown in Equation 1.3.<sup>47</sup> In this equation,  $\rho$  refers to fluid density,  $u$  to fluid velocity, and  $L$  to the characteristic dimension of the channel, and these three values compose the inertial term;  $\mu$  refers to the dynamic viscosity of the fluid, and it composes the viscous term. At low  $Re$  ( $<1500$ ), laminar flow is observed, and at higher  $Re$  this transitions to turbulent flow. Microfluidics experiments take place at  $Re < 250$ . In turbulent flow, the flow regime typically observed on larger scales, chaotic mixing and movement of fluids leads to unpredictable behaviour and irregular dispersion of forces which are difficult to control; for example, in an emulsion made in a homogeniser (essentially a blender), a wide dispersity of particle sizes across whole order of magnitude may occur.<sup>48</sup> In laminar flow, the path taken by the fluid falls in a series of parallel lines without turbulence and becomes far more consistent; this predictable behavior may be harnessed to create consistent and reproducible conditions on the device.

$$Re = \frac{\rho u L}{\mu} \quad (1.3)$$



Droplet microfluidics is a subdiscipline within the field of microfluidics which uses microfluidic devices to form microscopic, self-contained units of one fluid in another. The frequently spherical units, or droplets, of one liquid are referred to as the dispersed phase, and the other liquid that forms and carries these droplets is referred to as the continuous phase. The field of droplet microfluidics aims to use droplets formed with these specialised geometries for carrying out large numbers of self-contained experiments using droplets as if they were microscopic roundbottom flasks. Droplets have been applied to perform chemical synthesis,<sup>49</sup> quantitative analysis,<sup>50</sup> and biochemical synthesis such as polymerase chain reactions (PCR)<sup>51,52</sup> to name only a few. The consistency of the sheer forces present in laminar flow may be taken advantage of to form droplets with a relatively low dispersity of sizes using specialised device geometries which are shown in Figure 1.4. Depending on method and fluids used, droplet diameters ranging from 10  $\mu\text{m}$  to 1 mm have been reported in the literature.<sup>53</sup> Exceptionally fast rates of droplet formation, as high as 5.3 kHz, have also been reported.<sup>53</sup> The T-junction and flow-focusing geometries are amenable to being formed on a flat, microfabricated device using lithographic methods, and the co-flow design is typically found in devices made out of capillaries. All of the work presented here was done using lithographic methods and devices made out of the silicone polydimethylsiloxane (PDMS). While some work over the course of the past 4 years has been carried out using flow-focusing geometries, the vast majority relied on the use of T-junctions, and no examples of flow-focusing droplet formation geometry are presented herein. A detailed description of the lithographic methods used (soft lithography and UV-photolithography) are presented in Chapter 4.

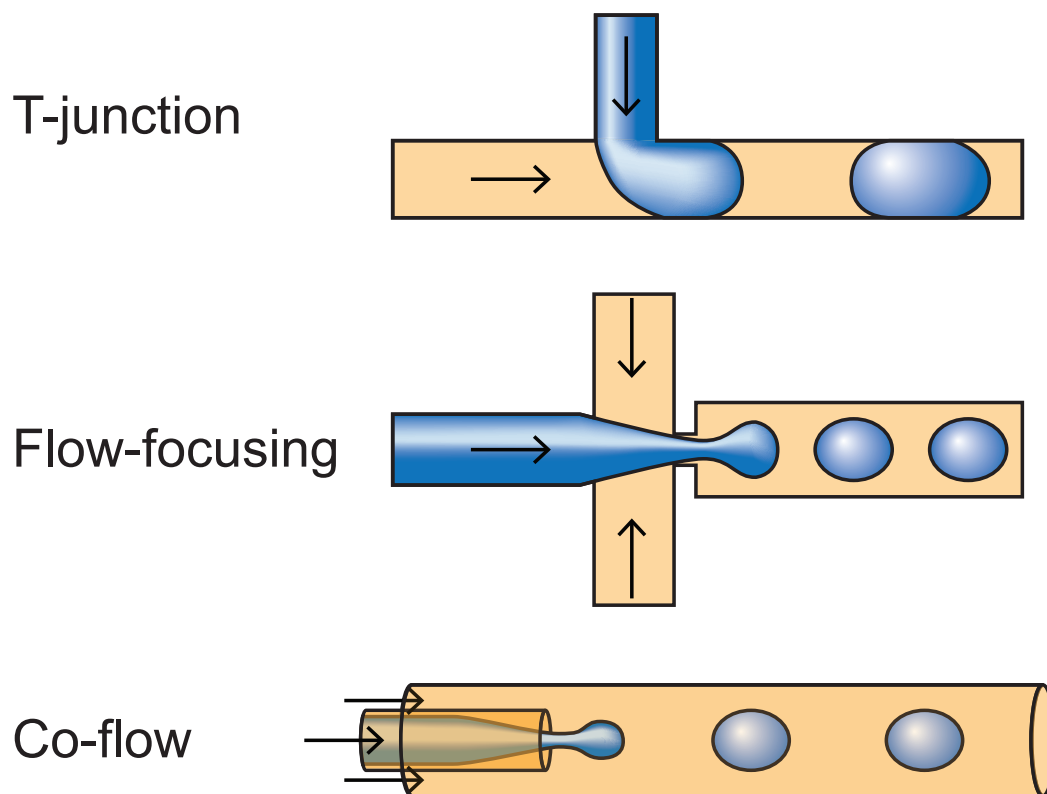


Figure 1.4: **Device geometries used for droplet formation in droplet microfluidics.** The T-junction and flow-focusing designs are most commonly associated with devices fabricated using soft lithography, and the channel cross section is therefore typically rectangular due to the nature of the fabrication technique. Co-flow designs are most commonly associated with devices utilizing capillaries, and as a result, the channel cross section is typically circular. Blue denotes the dispersed phase, which in this work is always aqueous. Orange denotes the continuous phase, which in this work is always an oil. Direction of fluid flow is indicated by arrows.

This ability to form large numbers of monodisperse droplets rapidly has made droplet microfluidics an increasingly popular platform for carrying out DIB experiments. Of the 94 papers where DIBs were used over the past two decades, 32 % of them formed DIBs using microfluidic methods, and this proportion is steadily increasing as can be seen in Figure 1.5. High throughput formation of DIBs has been achieved using microfluidics, with it being possible to form hundreds or even thousands of DIBs in the span of a minute.<sup>40</sup> While the throughput achieved by the devices presented herein is lower than the highest throughput DIB forming devices, the rate of DIB formation achieved (referred to here as “medium” throughput) is far greater than what is achievable by traditional methods, in part due to the faster rate of monolayer formation seen in droplets formed on a microfluidic device.<sup>54</sup> In the case of devices made using PDMS and soft-lithography, the material cost of a single microfluidic device is small, especially compared to the costs associated with cell culture. Finally, the skill required to operate a microfluidic device is considerably lower than that required to operate micromanipulators, and automation may be used to operate devices. This low skill requirement, higher rate of DIB formation, and low per-unit cost in comparison to traditional methods has likely been driving the growing interest in droplet microfluidics for DIB formation.

Despite the potential of microfluidic devices to produce DIBs in a high throughput manner, relatively few microfluidic approaches to DIB formation are high throughput, or even “medium” throughput. The approaches used for DIB formation on microfluidic devices are discussed in detail in Chapter 2, along with their strengths and shortcomings.

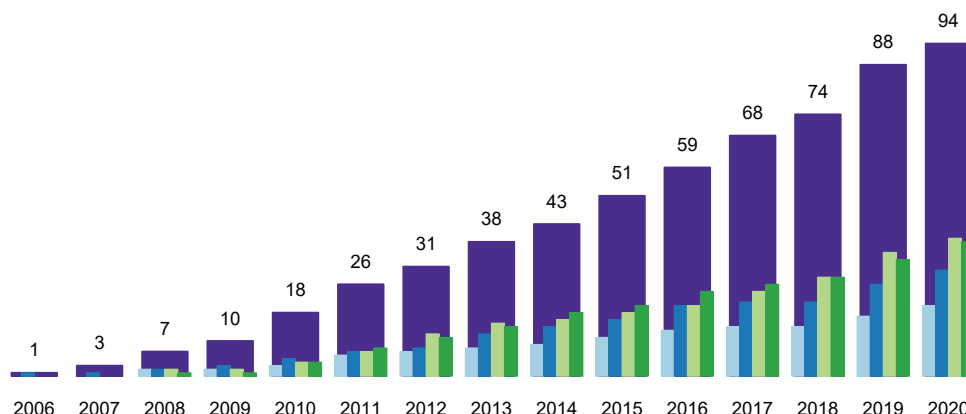


Figure 1.5: **Breakdown of trends in the field of DIBs by year.** Papers were compiled by one of our undergraduate students, and methods used by each categorized for publication as electronic supplementary information with the review shown in Appendix A. Total number of papers is shown as the large, violet bars, with numbers above for scale. The small bars are described in order from left to right. Light blue shows the number of publications carrying out exotic insertions of material into the DIB, meaning any protein or small molecule other than the two most commonly used proteins  $\alpha$ -hemolysin and alamethicin. Dark blue shows the number of publications using microfluidic methods, which initially comprise a small percentage of DIB publications before becoming more widespread. Light green shows the number of publications using exotic lipids, this being lipids other than the synthetic phospholipids DPhPC and DOPC. Dark green shows publications using fluorescence or spectroscopy in their experimental methods, as opposed to the only other analytical method widely employed in the literature: electrical recordings using a patch clamp amplifier.<sup>37</sup> Fluorescence methods provide the most accessible means to quantify pharmacokinetics with DIBs, and are the only methods used in this work.

## 1.5 Research motivation

This work seeks to establish the potential of DIBs as a pharmacokinetics modelling platform, and advance the use of microfluidic methods for carrying out pharmacokinetics assays for drug discovery. A new approach to DIB formation was the first step of this process, with the aim of producing a PDMS microfluidic device allowing cell-sized networks of DIBs to be formed without the use of on-chip electronic components, and with features such as very gentle droplet contact enabling the use of biomimetic lipid mixtures. No such device existed before this work, and no previous examples of using biomimetic phospholipids on a microfluidic device had been reported. The design process for this microfluidic device is detailed in Chapter 2, and served as the critical foundation to the rest of the pharmacokinetics work presented herein. Despite PDMS being the most common material in microfluidic devices for DIB experiments, nothing is known about the ways in which PDMS interacts with phospholipids. Answers to questions about the ways in which phospholipids interact with PDMS were therefore sought utilising a mix of computational and real-world data, and this may serve to inform the designs of future work using microfluidic devices for DIB formation. This work may be found in Chapter 3. Using my newly developed microfluidic platform, I sought to demonstrate that DIBs may not only be used to construct models of the cell, but that they can outperform current cell-free assays such as PAMPA in this task. This work culminated in a collaborative publication in *Lab on a Chip* carried out with my colleague Jaime Korner,<sup>55</sup> and this may be found in Chapter 4. I sought to also show that DIBs can be used for tasks previously

not demonstrated with other artificial membranes, such as examining the effect of asymmetry on membrane permeability to a drug. This work also sought to use a DIB based pharmacokinetic assay to study the diffusion of a currently used chemotherapy drug for the first time, exploring the effect of malignant changes in cancerous cells on their pharmacokinetics, a non-trivial task using existing artificial membrane methods. This work led to a publication in Chemical Communications,<sup>13</sup> and may be found in Chapter 5.

## **Chapter 2**

# **Design of a microfluidic platform for DIB formation**

Presented here is the foundational work for my research: the iterative process of device engineering that was instrumental in the microfluidic platform used for my publications in Chapters 4 and 5. All work is my own, though initial designs were based on current knowledge in the group as shown in Figures 2.2A and 2.3A. In this chapter I show a representative slice of the work I carried out, with several more redundant designs not included in the interest of keeping the narrative concise. Each piece of experimental data is, however, the product of an intensive process of design, cleanroom fabrication, device fabrication, testing, and incorporation of information learned into new designs. In total, 20 devices were designed and characterised. The aim of this work was to produce a robust, reconfigurable microfluidic device which could be used

widely within the group for a variety of applications. This was achieved, and multiple publications from our research group have already utilised these designs so far.<sup>13,55</sup>

## 2.1 Microfluidic methods for DIB formation

With the aim of my research being to establish the potential of DIBs for studying pharmacokinetics, my initial goal to design a microfluidic device for this purpose had a few key requirements. I sought to create a device which was able to make DIBs between cell sized droplets of dissimilar composition, that was able to contact droplets as gently as possible, that was reusable, that was reproducible, and that did not require the use of complex fabrication or operation techniques. Pharmacokinetic absorption experiments inherently require the presence of at least two compartments to observe a drug moving from one to the other, meaning I required at least two dissimilar droplets in a network on the device. As I intended to use naturally derived lipids for this purpose, gentle droplet contact would serve to make the device robust enough for lipids which might form a more delicate monolayer and bilayer. Making the droplets cell sized also would serve to make the system as biomimetic as possible. The requirement for multiple experimental replicates meant that a device which was not reusable would both make data acquisition more difficult, and fail to demonstrate the practicality of a DIB based pharmacokinetics assay. In the same way, a lack of reproducibility would fail to demonstrate the usefulness of the methods I was developing. The decision to avoid complex fabrication and operation techniques was both practical (due to only having



access to facilities for photolithography), and meant to make the techniques accessible to as many researchers as possible both within and outside of our group. Ultimately the device I engineered met all of these requirements, and proved robust enough to be used and reconfigured for the work shown in Chapter 4<sup>55</sup> and Chapter 5.<sup>13</sup>

Key methods for the formation of DIBs using microfluidic devices have significant overlap with other methods used in droplet microfluidics for droplet trapping,<sup>56</sup> merging,<sup>57</sup> and control.<sup>58</sup> They ultimately aim to enable precise control of size and location of droplets on the device. Droplet formation for DIB formation may be carried out using geometries called T-junctions,<sup>37</sup> flow-focusing junctions,<sup>59</sup> and in glass capillaries<sup>40</sup> as described in Chapter 1. Following droplet formation, a key feature of microfluidic devices for DIB formation is the use of a meander section where the microfluidic channel switches back on itself, extending the length of the channel and allowing time for a lipid monolayer to form.<sup>60</sup> Following equilibration, droplets must be slowed or trapped to allow them to come in contact and form a DIB. Key methods of doing this without active components are with pillar sections<sup>41</sup> (Figure 2.1A), rails<sup>60</sup> (Figure 2.1B), and hydrodynamic traps<sup>61</sup> (Figure 2.1C). More complex approaches may make use of solenoid valves to guide droplets directly with active control,<sup>62,63</sup> in a manner similar to using micromanipulators (see Figure 2.1D). Devices using solenoid valves do not typically have fluid pumped through them continuously like methods relying on device geometry, instead using timed sequences of flow applied from several inlets to precisely control the formation and location of droplets.

While microfluidic methods for forming DIBs work reliably for the most com-

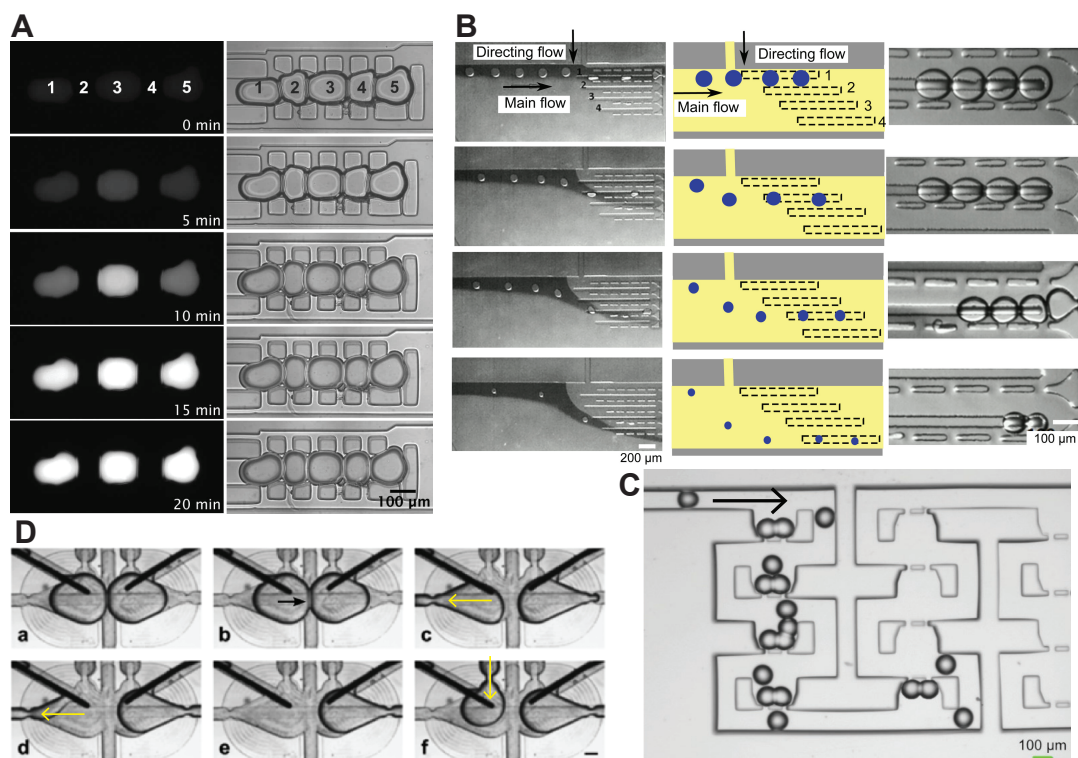


Figure 2.1: **Literature examples of microfluidic DIB formation.** A) A device utilizing a pillar structure referred to as a shift register to trap droplets for DIB formation.<sup>64</sup> An alternating series of ABAB droplets is trapped in the pillar section, allowing diffusion to occur and a fluorescent reporter (seen as white) to be activated. B) A device using a set of parallel rails and pillar sections to trap a series of droplets for DIB formation.<sup>65</sup> Notable is the use of an inlet for flow to direct the droplets towards the chosen rail, labelled as directing flow. C) A set of hydrodynamic traps which capture droplet pairs to allow for DIB formation.<sup>61</sup> Droplets are pumped in from the top left. D) DIB formation in a device using solenoid valves to actively load and unload droplets for DIB formation.<sup>62</sup> Flow direction in each step is shown with a yellow arrow. The DIB can be seen forming in a and b (indicated by black arrow), followed by the unloading of leftmost droplet (steps c-e), and the subsequent injection of a new droplet from the top in step f, highlighting the precise control possible using active controls. All images have either been reproduced with permission (B and C), or under the terms of the Creative Commons license (A and D).<sup>66</sup>

monly used lipids, several shortcomings limit their application to pharmacokinetic experiments. I found experimentally that pillar sections (Figure 2.1A) and hydrodynamic traps (hydrodynamic referring to the continuous phase still being in motion, see Figure 2.1C) may cause droplets to come in contact at high speed, their functionality depends on the viscosity and surface tensions present for a set of fluids, and the sharp edges of their structure may disrupt the monolayer formed between the oil and water. These factors may contribute to droplet coalescence, or failure of a device designed for one set of oils and lipids to be used with different types of oils and lipids. Hydrodynamic traps create operational complexity, as many designs require that droplets be unloaded from the traps by reversed flow,<sup>61</sup> or may not even provide a means to unload droplets after the experiment is completed.<sup>65</sup> Inability to unload droplets from a microfluidic device in this way prevents the reuse of the same device for more than one experimental replicate, significantly increasing cost and requiring frequent device changes. All microfluidic devices are sensitive to dust and particulates, but the geometry of traps and pillars are particularly prone to trapping dust and particles, preventing the reliable operation of the device. While robust, solenoids and other active on-chip controls create fabrication and operational complexity, and are not much faster than traditional methods utilising micromanipulators.<sup>63</sup> Finally, most non-solenoid methods reported in the literature rely on interleaving of droplets from two parallel droplet generators to form DIBs in series.<sup>61,64,67</sup> Interleaving is a verb that in this context refers to the process of combining multiple parallel droplet streams into a single droplet stream that follows a consistent sequence in series. The resulting droplet stream is described herein with the adjective alternating, which for two

droplets of compositions A and B would mean the resulting droplet stream follows the repeating sequence ABAB. De-interleaving, as the name implies, refers to splitting an alternating droplet stream back up into multiple parallel streams. I have found that this negatively impacts reproducibility due to interleaving errors, and while it is possible to differentiate droplets of different compositions with fluorescence or dyes, it may be more difficult to generalise this to other techniques such as LC-MS for detection due to inability to visually discern correct experimental conditions, limiting the possibilities for future development. A method of forming DIBs with differing compositions, without relying on correct interleaving of dissimilar droplets, or use of active controls like valves and solenoids is therefore desirable to enable reproducible and accessible microfluidic DIB experiments.

Prior to this work, rails have been used to store DIBs on a microfluidic device, using a secondary oil inlet to guide droplets onto the rail.<sup>60</sup> My work sought to use rails in a way previously unreported: holding droplets in the center of a broadening chamber which gently brings the train of droplets together in series, or to guide together multiple separate streams of droplets and form DIBs between them in parallel. This chapter details the process used to pick this direction, and a new design of microfluidic device for the formation of DIBs. The final device developed does not rely on traps for DIB formation, can be stopped and started without reverse flow, does not require any active on-chip components, and allows DIBs to be formed between dissimilar droplets without relying on interleaving.

## 2.2 Layered devices: DIB formation on a rail

My initial work in designing a microfluidic device built upon the work of previous students in the group and Katherine Elvira. They sought to investigate the use of channel broadening as a means of slowing and contacting droplets. Given that flow rate on a microfluidic device is proportional to channel cross-section,<sup>47</sup> it follows that a steadily broadening chamber would lead to a progressive slowing of droplets, causing them to “pile up” and come together. This slow contact was predicted to be gentler and more controllable than smashing droplets together in a trap or pillar section, making it more suitable for DIB formation. Representative samples of the designs developed by Matt Noseworthy are shown in Figure 2.2. Another variant of both designs (not shown) was developed and tested which did not incorporate a meander, but these were deemed unsuitable for DIB formation due to lack of appropriate equilibration time.

I fabricated and tested Matt’s initial designs using a solution of DPhPC in aqueous buffer with a squalene continuous phase, and the results of this are shown in Figure 2.2. Figure 2.2A shows a device design incorporating both a pillar section and the broadening main chamber. This design rapidly showed that incorporation of pillar sections into this new design philosophy of a broadening main chamber was not going to function correctly. As seen in Figure 2.2B, within the first seconds of droplets entering the pillar section, the pillar section filled with droplets, and the droplets merged. This appeared to be due to the combination of excessive deceleration of the droplets leading to high speed contact and coalescence, and excessive friction on the sides of the pillars causing droplets to become permanently stuck inside the pillar section.

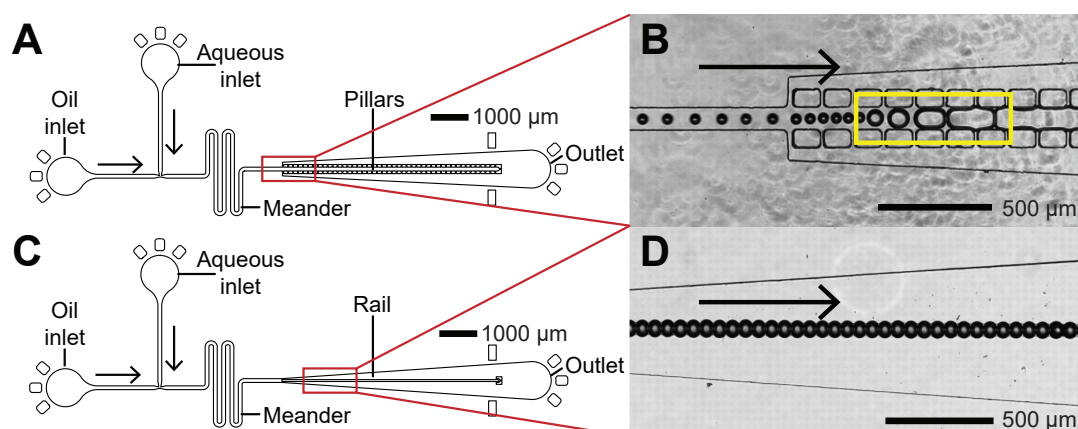


Figure 2.2: **Chamber broadening devices.** Shown here are the device designs for the initial channel broadening devices and their experimental behavior, direction of flow is indicated by arrows. A) Scale drawing of a pillar based device. B) A common failure mode seen in device A. Droplets can be seen piling up and coalescing in the highlighted region. C) Scale drawing of a rail based device. D) Droplet train formed on device C, which shows the potential of these types of devices to generate long strings of droplets and DIBs. Designs shown were developed by Matt Noseworthy.

Figure 2.2C however showed that a design incorporating a rail instead of pillars both allowed droplets to be held in line with each other, and allowed them to be brought together to enable DIB formation. A rail is a structural feature of a microfluidic device that relies on fabricating multiple layers on the device: a main layer bearing the channels and droplet formation geometry, and another layer containing the rail, which is essentially a narrow trough. Droplets are partially squeezed into this trough, which then serves to keep them pinned to the rail. Long trains of droplets could be formed using this method, with an example shown in Figure 2.2D. Interestingly, unintended presence of particulates in the oil phase made visualising its rate of flow possible, and revealed that oil flowed faster than the droplets; this suggested that droplet dragging in the rail was partially responsible for their slowed rate of movement and contact. The

dragging of the droplets appeared proportional to the length of droplet train formed, suggesting that progressive broadening of the main chamber was helpful but not critical to allowing droplets to come together.

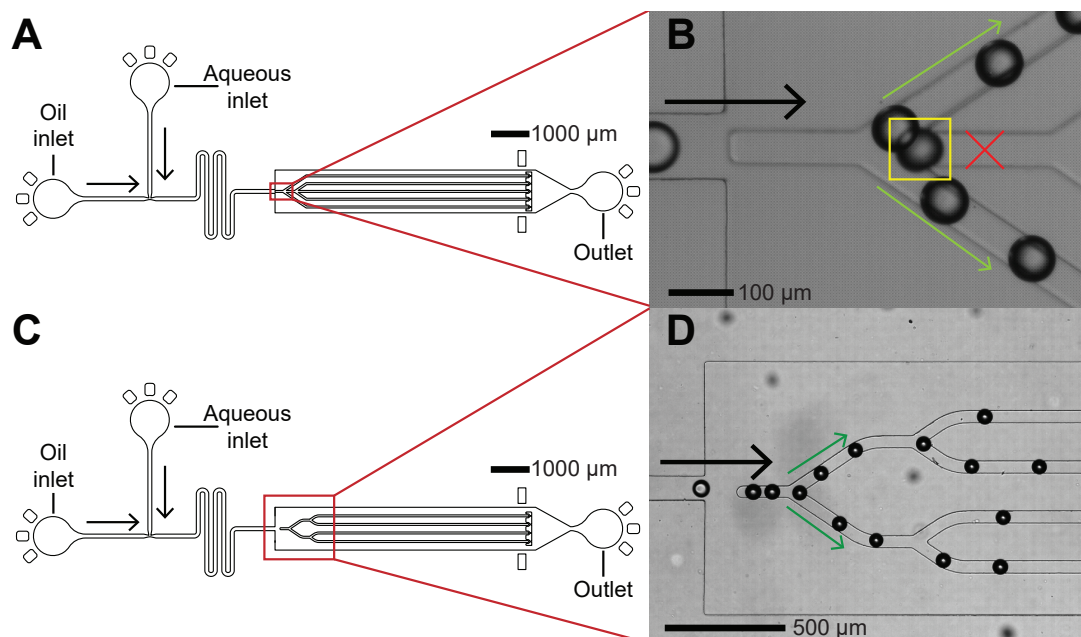


Figure 2.3: **Branching rail based devices.** Here we see devices using purely geometry to direct trains of droplets towards distinct paths. Direction of flow is shown with black arrows, and direction of droplet movement is shown with green arrows A) Scale drawing of a three branch per node DIB array generator, designed by Matt Noseworthy B) Common failure mode of device A, where a droplet becomes trapped on the rail geometry, as highlighted with a yellow box. The path indicated by the red X is now inaccessible, and the droplets are only allowed to traverse the top and bottom rails. C) Scale drawing of a binary tree type DIB array generator. D) Device C in operation, showing droplets being directed down the tree structure of the rails.

The idea of a broad but constant width main chamber was carried forward to rail based designs intended to form an array of droplets on multiple rails in parallel, which can be seen in Figure 2.3. At the time of development it was unknown if having a

single type of droplet on each rail, or an alternating series of droplets on each would perform better, but either scenario required the droplet stream entering the main chamber to have an alternating pattern of compositions to be useful for pharmacokinetics experiments. The work on these designs consisted of only a single droplet type for simplicity, with alternating droplet generation to be the focus of subsequent work. Figure 2.3A shows the initial design proposed by Matt Noseworthy, which I fabricated and tested. The results of these tests with DPhPC in buffer and squalene are shown in Figure 2.3B, where droplets would become trapped in the passage between nodes (the branch point), causing droplets to only be able to access the two side rails. Given the tendency of droplets to want to take one of two branching paths, I used the concept of a binary tree from computer science for a subsequent design, wherein each branching node has two child nodes. The resulting binary tree design is shown in Figure 2.3C. The device behaved as expected, with droplets reliably being switched between the two branching paths with a split close to 50/50 (Figure 2.3D). With the device working as expected, focus was shifted towards the generation of alternating droplet streams. However, subsequent work discussed in the following section revealed that accurately interleaving and de-interleaving droplets is a very challenging task.

## **2.3 Droplet steering, control, and alternating droplets**

I directed the focus for the next phase of my device development research towards reliably forming droplets of alternating composition by interleaving them. For this,



methods from the literature, as well as new approaches were employed. Ultimately, the conclusion reached by this body of work was that interleaving of droplets by any method leads to too high of an error rate to be relied upon for pharmacokinetic experiments, particularly for any system using more than two types of droplet, or where the droplets cannot easily be differentiated by visual or spectroscopic means.

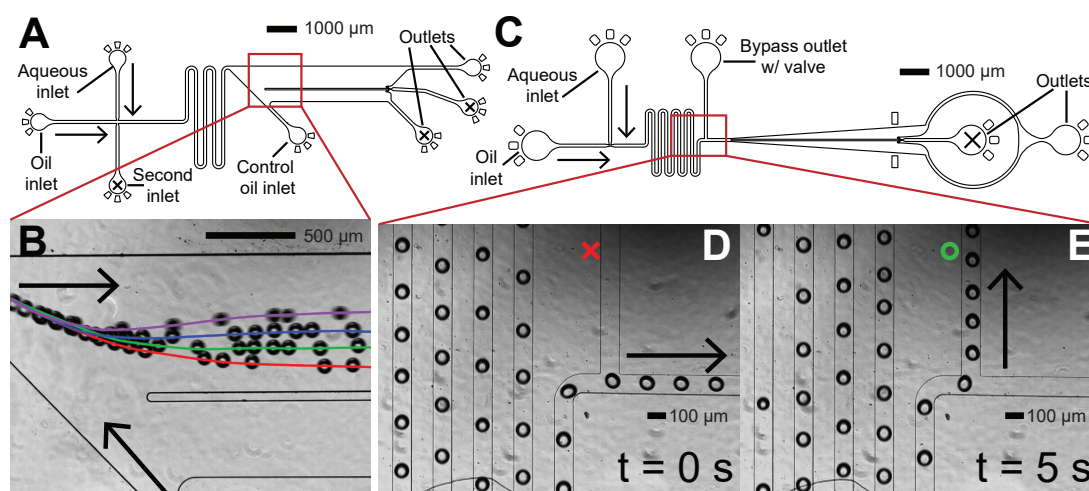
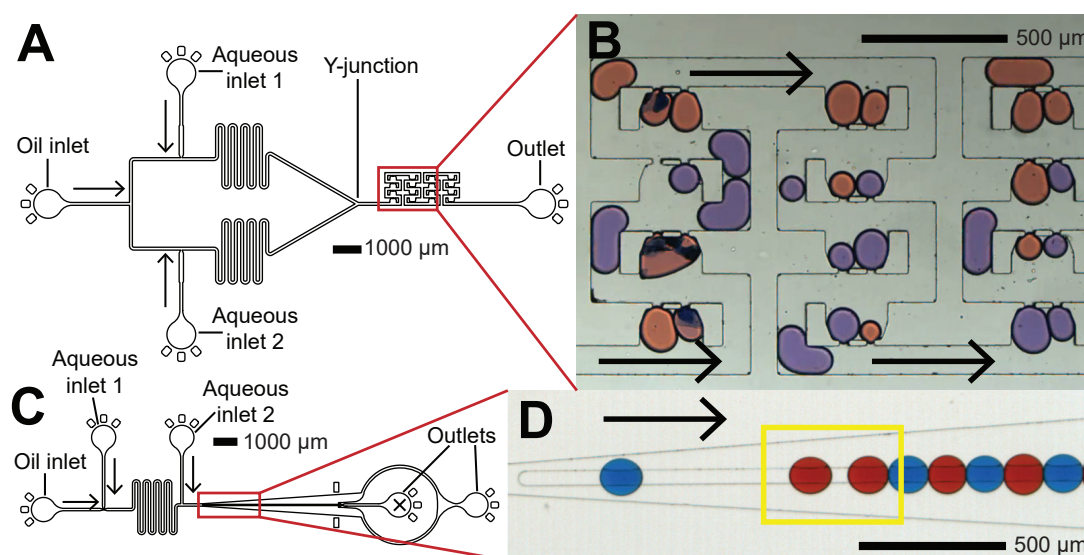


Figure 2.4: **Flow rate manipulation for droplet control.** Flow direction is indicated by black arrows, and inlets and outlets marked with a black X are unused for the shown experiments. A) A device designed for steering droplets towards a rail using a control oil inlet, similar to the device described by Carreras *et al.*<sup>65</sup> B) Composite image of device A in operation, with paths taken by droplets for each control inlet/main inlet flow rate ratio indicated by the coloured lines. The ratios of control flow rate to main inlet flow rate are: 0.25, shown in red; 0.5, shown in green; 1.0, shown in blue; 1.5, shown in violet. C) A device designed to use a valve to control droplet direction. D) Device C in operation, the bypass valve is closed as indicated by the red X, and droplets are directed solely towards the main chamber. E) Device C in operation 5 seconds after conditions shown in D. The bypass valve is open as indicated by the green circle, and the droplets exit the device through the bypass outlet.

The initial solution to interleaving errors within the chains of droplets was to include some form of on-chip error correction, or selection of good sets of droplets that

form the correct sequence. This work is shown in Figure 2.4. The design shown in Figure 2.4A was based on a methodology in the literature where a control port connected to the main chamber allowed droplets to be directed to a rail on demand.<sup>60,65</sup> Shown in this design but unused in this experiment is one of the most basic methods of forming alternating droplets, where two droplet generators are directly opposed to each other at a T-junction.<sup>67</sup> This method, despite its simplicity, was found to be highly unreliable. Included on the device as well is a port for unloading the rail, a feature which remained untested as research focus shifted towards other more promising designs. The composite image shown in Figure 2.4B shows the effect of changing the ratio of flows from both the inlet and control port (labelled). Laminar flow results in a predictable pattern to the droplets for a given flow rate. A design allowing for the removal of mismatched droplets via use of a valve is shown in Figure 2.4C. When closed, the valve prevents flow into the bypass channel, and forces them into the main chamber (Figure 2.4D). Opening the valve allows droplets to bypass the main chamber (Figure 2.4E), removing "bad" droplet sequences from the device, and allowing droplets in the main chamber to remain stopped in place as flow bypasses the main chamber. While the droplet selection features of both designs worked as expected, the response time was not fast enough to enable an immediate switch from one flow path to another, and these methods were abandoned in favor of a solution that does not require the selection of droplets.

The approach of interleaving droplets by having two droplet generators joined by a Y-junction was tested next. This method has been shown before in the literature to generate ABAB alternating droplets with DIBs.<sup>64</sup> I suspected that this approach



**Figure 2.5: Formation and trapping of alternating droplets.** Flow direction is indicated by black arrows, and the outlet indicated with an X unused for the shown experiment. Differently coloured aqueous solutions are pumped in at each T-junction for each. A) Device design using a Y-junction to allow interleaving of droplets from two droplet generators before trapping in a hydrodynamic trap as used by Nguyen *et al.*<sup>61</sup> B) Device A in operation. Note the large number of mismatched droplet sizes, and failure to match dissimilar droplets to each other in most of the traps. C) A device configured to allow alternating droplets to be formed from two T-junctions in series. D) Device C in operation, showing a train of ABAB droplets on the rail of the main chamber. Consistency in size and interleaving is notably higher than the device seen in B, but an interleaving error (highlighted) is still present.

may not be reproducible, or at least not to the extent required for my research. This was due to the high level of difficulty in perfectly matching droplet sizes and spacing, something required for perfect interleaving. Shown in Figure 2.5A is the design used to test this method, including an array of hydrodynamic traps<sup>61</sup> intended to store pairs of droplets for carrying out experiments. Despite its use in the literature, initial work revealed that the interleaving of droplets can indeed be difficult to reliably reproduce. Failure of most microfluidics literature to report statistics on the reproducibility of their droplet generation also made evaluating their potential for use in my research challenging. Figure 2.5B shows the relatively small number of droplets of dissimilar compositions that were successfully interleaved and trapped, with matched pairs being quite common. This was repeated with a design based on previous rail designs, shown in Figure 2.5C, which simply formed droplets at two T-junctions in series. While the success rate for this method appears to be higher (Figure 2.5D), as can be seen, even consistent droplet trains tended to have interleaving errors. While this could likely be improved with tuning of the design and more precise syringe pumps, it was unclear to what extent this would be possible given the variety of fluid and lipid properties present across the group, and the variability in surface properties of PDMS, both of which complicated the ability to match flow rates and droplet sizes. As a result, I chose to abandon this approach in favour of a more reproducible one.

I decided that a new pressure pump with an extremely fast response time would be beneficial to a new approach to DIB formation. All previous work had been carried out using syringe pumps, which have a slow response time on the order of many seconds, and pulsation in their flow at low flow rates due to the presence of step-

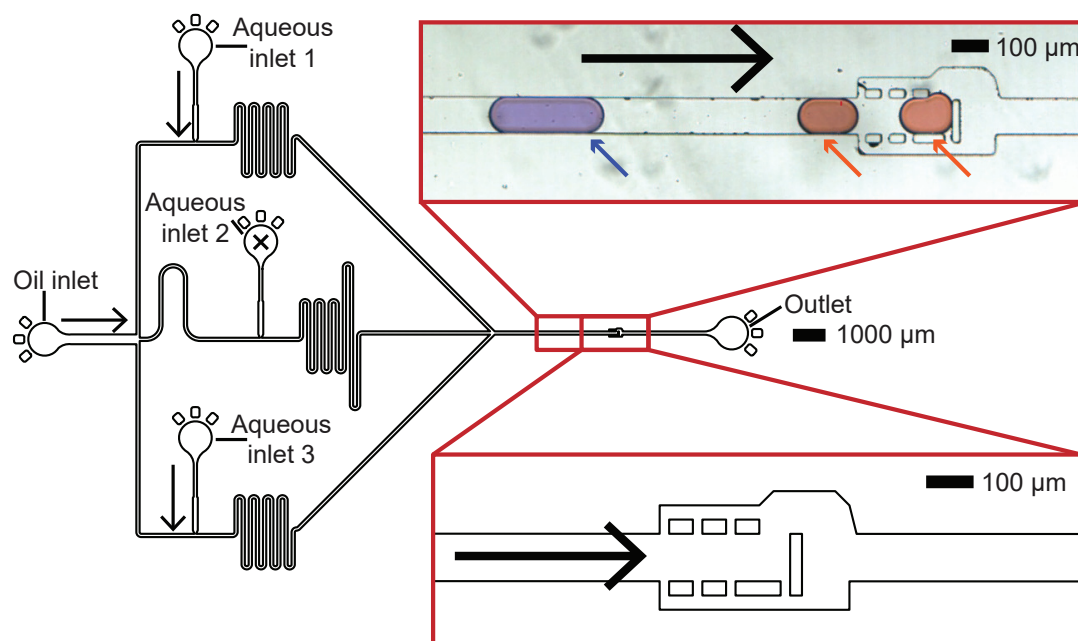


Figure 2.6: **Alternating droplets formed using a pressure pump.** A device designed for droplet on demand formation of alternating droplets for capture in a shift register structure similar to the one reported by Zagnoni *et al.*<sup>68</sup> Direction of flow is indicated with arrows, with oil being pumped in from the leftmost inlet, and differently coloured aqueous solution pumped in at the top and bottom inlets. A magnified view of the shift register is shown at the bottom. The device in operation can be seen at the top. Notable is the interleaving error which has occurred (orange arrows), as two orange droplets break the desired ABAB sequence. Also notable is the mismatch in size (blue arrow) between droplets from different inlets, showing the lack of consistency of droplet-on-demand formation using a pressure pump.

per motors. Use of a pressure pump enabled pulsation free flow for more consistent droplet size, and for the flow to be stopped suddenly, enabling levels of device control not possible with syringe pumps. Millisecond pulses of pressure may also be used to form droplets-on-demand. Droplet-on-demand refers to a droplet formation approach in droplet microfluidics which can form droplets purely as needed using some form of control. Alternating droplets could be formed either by applying a constant pressure as in Figure 2.5, or by applying momentary pulses of pressure to each fluid as shown in Figure 2.6. The constant pressure approach was tested with a Y-junction type device containing a trap section (Figure 2.5A) based on a design in the literature.<sup>68</sup> This proved ineffective, as shown in Figure 2.5B. The constant pressure approach was also tested with the design shown in Figure 2.5C. The two aqueous inlets are indicated, with the design shown being the same as in Figure 2.4B. Despite the differing path lengths, droplets could be injected at both points in the channel path when the device was run and still generate a stream of alternating droplets (Figure 2.5D). This approach performed better than the Y-junction, but still showed interleaving errors. The pulsed pressure approach to forming alternating droplets on-demand was tested last, with the design shown in Figure 2.6 utilising a trap section from the literature (expansion).<sup>68</sup> The inset photograph shows that despite the unprecedented level of precision and control present with droplet-on-demand formation using a pressure pump, errors in interleaving and inconsistent droplet sizes still frequently occur. These errors were also observed when performing droplet-on-demand formation with other device designs. While droplet-on-demand approaches have been used before with on-chip valves and solenoids,<sup>62</sup> I found that doing this with a pressure pump alone was still beyond the

capabilities of even the most responsive of pressure pumps.

With options for droplet selection and interleaving exhausted, and with even the most sophisticated of pumping equipment unable to form droplets on demand without active controls on-chip, it became clear that trains of alternating droplets were not suited to forming droplet networks for pharmacokinetics experiments. While previously employed in the literature, the high miss rate and reproducibility concerns for even ABAB alternating droplets made it clear that more complex networks were out of the question. It was at this point that an idea struck, and I decided that a responsive pressure pump enabled a completely new approach to forming alternating DIBs, without needing to interleave droplet streams.

## **2.4 Parallel rails: a new approach to DIB formation**

Until this point, all of the work that I had carried out assumed that some method of trapping droplets was critical to the operation of the microfluidic device; however, the acquisition of our new pressure pump had shown that flow could be stopped instantaneously, and restarted just as quickly. This meant that DIB formation and pharmacokinetic experiments could be carried out, so long as the flow could be stopped when droplets were in contact.

My work with parallel rail arrays informed the design of microfluidic device shown in Figure 2.7A, which was operated at a constant pressure for each inlet. A singular oil

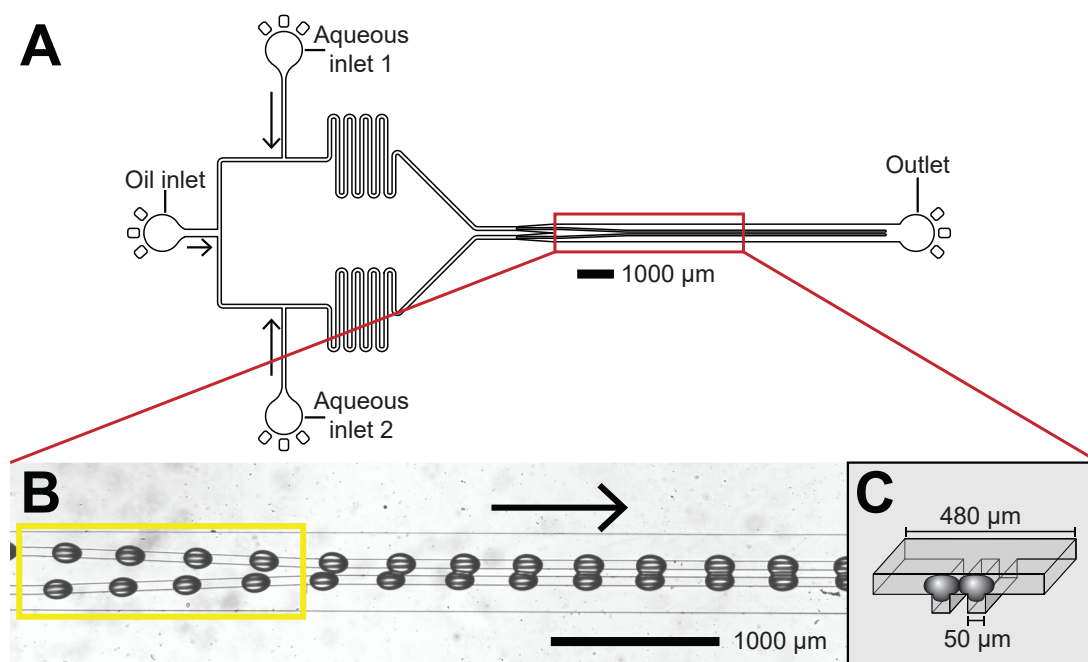


Figure 2.7: **Parallel rail based DIB formation.** Direction of flow is indicated with arrows. A) Device design for formation of droplet pairs on rails. Oil is pumped in from the far left inlet and aqueous solutions are pumped in from the top and bottom inlets. B) Device A in operation, showing the ideal condition of matched flow rates from all inlets, and the resulting synchronised droplet streams. The region where the rails are gently brought together is highlighted. C) Side view of the main chamber of the device with labelled dimensions. The rails appear as a trough, with the droplets being squeezed into the rail and guided along it.



inlet was used for this design for simplicity, and because more complex designs similar to the ones shown in 4<sup>55</sup> and 5<sup>13</sup> could be operated. The pressure pump was the source of this operational constraint, as it allowed the connection of only 4 fluid reservoirs. Separate streams of droplets could be formed in their own droplet generators (each connected to their own reservoir) before being brought into the main chamber of the device and loaded onto a set of parallel rails. Critical to the operation of this device are the matched lengths of the channels leading to the droplet generator and main chamber. A feature unique to a pressure pump is that flow rate is purely dependent upon the resistance to a fluid moving through a channel. As a result of this operational quirk, the channel lengths must be matched to get the same flow rate across the mirrored sides of the device. By bringing the rails in the main chamber together gradually, the droplets were brought into contact far more gently than possible with any of my previously tested methods, enabling consistent and reproducible DIB formation as seen in Figure 2.7B. While droplet trains may under ideal (perfectly balanced) circumstances be synchronised as in Figure 2.7B, a more commonly observed outcome is the slightly faster flow of one stream of slightly smaller droplets that drag less on the rail in the main chamber. As a result, often only momentary droplet contact occurs under less than ideal conditions, meaning capture of one or more DIBs requires the flow to be stopped quickly. This is how the devices were operated with the pressure pump: at the precise moment of droplet contact, the pressure to all inlets was removed, and data could then be collected.

To quantify performance of the device, statistical data was collected by recording 1 min of video in the main chamber of the device for  $n=4$  devices while running the

pressure pumps in constant pressure mode, and counting the number of droplet pairs brought in contact and the number of those pairs which formed DIBs. I found that  $88 \pm 7\%$  of droplets that entered the main chamber of the device formed usable DIB pairs. DIBs were formed at a rate of  $1.7 \pm 0.2$  Hz. While not as fast as high throughput methods of forming DIBs,<sup>40</sup> this rate of DIB formation greatly exceeds that of traditional methods, and of most of the microfluidic methods of forming DIBs found in the literature, making it sufficient for my work. In addition, the device inherently has no interleaving errors, as no interleaving is required.

This final design, and variants thereof forms the backbone of the remainder of my work. A three rail variant of this design was used for carrying out pharmacokinetic experiments meant to replicate the intestinal space. This collaborative work may be found in Chapter 4. With a robust approach for the formation of DIB pairs, I set my sights on a variant of this design which utilized longer meanders and two separate oil streams. I used this device to form asymmetric DIBs lipid out (with the lipids dissolved in the oil), and this work may be found in Chapter 5.

## 2.5 Experimental details

### 2.5.1 Materials

Devices were fabricated from Sylgard 184 (Ellsworth Adhesive) PDMS on PDMS coated glass microscope slides, and were prepared from an SU-8 3050 (MicroChem)

on boron-doped silicon (Silicon Materials) master. For all experiments depicting colorless droplets in this chapter, the dispersed phase consisted of  $10 \text{ mg mL}^{-1}$  DPhPC ( $\geq 99\%$ , Avanti) in an aqueous buffer consisting of  $10 \text{ mM}$  pH 7.6 HEPES ( $\geq 99.5\%$ , Millipore Sigma) and  $200 \text{ mM}$  KCl ( $\geq 99\%$ , Millipore Sigma). The continuous phase in these experiments consisted of squalene ( $\geq 98\%$  purity). For experiments depicting coloured droplets, a 1:2 mixture of fountain pen ink (Pilot Iroshizuku) and RO water was used for the dispersed phase, with a  $2.5\%$  solution of Picosurf<sup>TM</sup> (Sphere Fluidics) in FC-40 (Aldrich) as the continuous phase. All solutions were filtered through  $0.45 \mu\text{m}$  syringe filters before being introduced to the devices.

## **2.5.2 Device fabrication and solution preparation**

All devices were fabricated using a combination of photolithography and soft lithography. A detailed description of this process has been previously published,<sup>55</sup> and may be found in Chapter 4. Phospholipids in buffer were prepared via extrusion according to the procedure also detailed in Chapter 4.

## **2.5.3 Operation of devices utilising syringe pumps**

Examples of experiments utilising syringe pumps may be found in Figure 2.2, 2.3, 2.4, and 2.5D. In these experiments, solutions were dispensed onto the microfluidic device using Aladdin AL-1000 syringe pumps and  $1 \text{ mm}$  gastight syringes (Hamilton) through  $1/16''$  outer diameter,  $0.75 \text{ mm}$  inner diameter PTFE tubing (Chromatographic

Specialties). The following experimental conditions are depicted in this chapter:

- Figure 2.2B - oil flow rate:  $3.00 \mu\text{L min}^{-1}$ , aqueous flow rate:  $0.65 \mu\text{L min}^{-1}$ . In this experiment, chip has been prepared by surface treatment using 5% trichloro(1H,1H,2H,2H-perfluorooctyl)silane (Aldrich) in isopropanol.
- Figure 2.2D - oil flow rate:  $4.50 \mu\text{L min}^{-1}$ , aqueous flow rate:  $0.35 \mu\text{L min}^{-1}$ . In this experiment, chip has been prepared by surface treatment using 5% trichloro(1H,1H,2H,2H-perfluorooctyl)silane (Aldrich) in isopropanol.
- Figure 2.3B - oil flow rate:  $4.00 \mu\text{L min}^{-1}$ , aqueous flow rate:  $0.02 \mu\text{L min}^{-1}$ .
- Figure 2.3D - oil flow rate:  $3.00 \mu\text{L min}^{-1}$ , aqueous flow rate:  $0.05 \mu\text{L min}^{-1}$ .
- Figure 2.4B - main oil inlet flow rate:  $10.00 \mu\text{L min}^{-1}$ , aqueous inlet flow rate:  $0.25 \mu\text{L min}^{-1}$
- Figure 2.4D and E - oil flow rate:  $10.00 \mu\text{L min}^{-1}$ , aqueous flow rate:  $1.00 \mu\text{L min}^{-1}$ . The bypass valve is connected to a syringe withdrawing at a flow rate of  $10.00 \mu\text{L min}^{-1}$ .
- Figure 2.5D - oil flow rate:  $2.00 \mu\text{L min}^{-1}$ , aqueous flow rates:  $0.15 \mu\text{L min}^{-1}$ .

## 2.5.4 Operation of devices utilising syringe pumps

Examples of experiments utilising a pressure pump may be found in 2.5B, 2.6 and 2.7. In these experiments, pressure is applied to airtight tanks using an Elveflow OB1mk3

pressure controller, which pushes the solutions onto the microfluidic device through matched lengths of 1/16" outer diameter, 0.25 mm inner diameter PTFE tubing (Chromatographic Specialties). In order to ensure consistent backpressure, the lengths of tubing are primed by filling with solution before being connected to the device. Device backpressure varies from experiment to experiment and throughout an experiment, so operating conditions are generally reported as pressure ranges. With solutions of the viscosities tested, aqueous and oil solutions typically require similar or identical pressures for droplet formation.

The pump may be operated in either constant pressure or pressure profile mode. In pressure profile mode, the pressure applied to the tank may be controlled in a similar manner to a function generator, and the pressure profile may resemble a sine wave, a triangle wave etc. When being used for droplet-on-demand formation, the difference between the baseline and peak pressure can be referred to as pressure delta. The following experimental conditions are depicted in this chapter:

- Figure 2.5B - constant pressure mode, 85-95 mbar.
- Figure 2.6 - sine pressure profile, 180° out of phase, 30 mbar baseline pressure, pressure delta 2 mbar.
- Figure 2.7 - constant pressure mode, 120-140 mbar.

## Chapter 3

# Phospholipids facilitate water adsorption and failure of surface properties on PDMS microfluidic devices

Presented in this chapter is the portion of my research dedicated to studying the fundamental behaviour of phospholipids on microfluidic devices. I designed and carried out all *in situ* and *in silico* experiments shown herein. Ricardo Ramírez, a former Mitacs researcher in our group, developed and optimised the initial COMSOL model which would be adapted for this experimental work. I adapted this model to incorporate experimental contact angle and interfacial tension measurements using a derived equa-

tion, modified it to report additional values, and ran all of the simulations. Sean Farley, a graduate student and former undergraduate student in our group, carried out the interfacial tension measurements (shown in Table 3.1) both at the University of Victoria and at the University of British Columbia. Genie Lee and Kate Adolph-Hammond, both former undergraduate researchers in our group, carried out the contact angle measurements. The goal of this work is to for the first time study and characterise the effects of phospholipids on PDMS microfluidic devices, and resolve unanswered questions about device reliability by supplementing *in situ* data with computational data otherwise not possible to obtain *in situ*. With this I intend to explain not often discussed and previously unexplained phenomena seen during microfluidic DIBs experiments, behaviour which was also observed in collection of data for Chapter 4 and 5. This work will ultimately serve to advance the understanding of phospholipid behaviour on microfluidic devices: something entirely overlooked by the literature, and a critical prerequisite for more widespread adoption of DIB based microfluidic methods.

### 3.1 Introduction

When making droplets for DIB creation on a microfluidic device, it is common to form aqueous droplets within a hydrophobic oil carrier phase. Surface, or interface physics play a critical role in this process.<sup>69</sup> An interface refers to the boundary existing between two substances which are immiscible, and may exist between any combination

of solid, liquid, or gaseous substances.<sup>70</sup> In general usage, a surface is the same thing as an interface, but for clarity I will be using it here only to refer to the interface between a solid and liquid, and use the word interface for all other cases. In a system with two or more immiscible substances, each of these substances are often referred to as “phases”.

While laminar flow regimes predominate and the behavior of fluids becomes predictable at microfluidic scales, wetting properties of the fluids on the walls of the device and the interaction at the interfaces between fluids have profound effects on how droplets behave.<sup>71,72</sup> Wetting refers to how a liquid interacts with a solid surface; a surface is wetted if the liquid sticks to the surface.<sup>73</sup> Because fluid and surface properties have such a profound effect on the process of droplet formation, use of surfactants is common within the field of droplet microfluidics, and in some cases are critical to the operation of a device by stabilising emulsions or reducing interfacial tension at droplet generators.<sup>74</sup> Surface modification may also be employed to change the wetting characteristics of the walls of the device to make it more hydrophobic or hydrophilic.<sup>75</sup> Surface modification in this context refers to altering the characteristics of a surface, either chemically or physically, to change how it interacts with a liquid. Changing the hydrophilicity/hydrophobicity serves to support the carrier phase in forming droplets, and prevents phase flipping: a scenario where the continuous phase and dispersed phase change roles.<sup>76</sup> Interfacial tension (IFT) is a tensile (pulling) force observed at an interface or surface caused by the attraction of molecules to each other on each side of the interface, and is directed within the plane of the interface in all directions. While this is generally described in terms of minimising free energy of



the interface, IFT may conveniently be thought of as the force required to stretch a rectangular section of a film for a given length. The formula describing IFT is shown in Equation 3.1, with  $\gamma$  referring to IFT, and  $F$  and  $L$  referring to force and length respectively.<sup>77</sup>  $\gamma$  is effectively the force exerted over the length of the interface, and as the force is exerted in both directions, the measured force ( $F$ ) must be divided by 2 to give  $\gamma$ . A surfactant is a substance which serves to decrease IFT, and some surfactants may also behave as an emulsifier: a substance which stabilizes droplets of immiscible phases so that they do not coalesce. Decreasing IFT serves to ease the process of droplet formation, as high IFT prevents droplets from easily breaking off at a droplet generator and may lead to conditions where no droplets form and the two phases flow beside each other (co-flow) if the sheer forces of the droplet generator cannot overcome the IFT.<sup>78</sup>

$$\gamma = \frac{1}{2} \frac{F}{L} \quad (3.1)$$

Microfluidic devices are commonly made out of the polymer polydimethylsiloxane (PDMS). PDMS carries numerous advantages when being used for droplet microfluidic devices, particularly in its ease of manufacture with conventional photolithographic methods,<sup>79</sup> low per-unit cost of a device, and its compliant nature enabling flexible device features such as pneumatic valves.<sup>80</sup> The natural hydrophobicity of PDMS in theory serves to assist in the formation of aqueous droplets. In practice however, PDMS is a complex material which can present considerable challenges when used for droplet microfluidics. PDMS is gas permeable<sup>79</sup> and permeable to

oils such as hexadecane and squalene,<sup>81</sup> which allow evaporation of aqueous droplets and swelling of the device geometry respectively. In cases where adsorption of surfactants to the walls of the device is critical for stable droplet formation, excessive contact with water may lead to device failure by removal of the adsorbed surfactant.<sup>82,83</sup> The permeable, flexible nature of PDMS furthermore complicates permanent surface modification, as chemical surface modifications will become internalized within the PDMS structure as the surface moves and shifts, a process called reconstruction.<sup>84</sup> This process can be thought of as like sauce being stirred into spaghetti, which is analogous to the tangled flexible polymers of PDMS tumbling over each other and carrying their surface modifications below the surface with them.

When making DIBs, phospholipids also act as the surfactant for the oil/water system.<sup>74</sup> This is because formation of a DIB depends upon the amphiphilic nature of phospholipids and their emulsion stabilising properties. While phospholipids behave as a surfactant and emulsifier in the process of DIB formation, kinetics of monolayer formation for both lipid-out and lipid-in systems strongly suggest that they do not have time to assemble at the oil/water interface during the relatively fast process of droplet formation.<sup>54</sup> This phenomenon is referred to as dynamic surface tension, which refers to the process of IFT decreasing as surfactant migrates to the fluid interface; this process can often be slower than the rate of droplet formation.<sup>78</sup> Indeed, microfluidic devices for DIB formation frequently employ structural features such as meanders or switchbacks to increase the distance between the droplet generator and the point of droplet contact to ensure complete monolayer formation and reliable emulsion stabilisation, as described in Chapter 2

Despite the growing interest in using PDMS based microfluidic devices to form DIBs, the behavior of phospholipids as surfactants on microfluidic devices has been largely overlooked, and any interaction that they have with PDMS in a microfluidic device remains unstudied and poorly understood. Naturally derived soy lecithin has in one case been compared to the surfactants sorbitan monooleate (Span 80) and polyglycerol polyricinoleate (PGPR) for its effect on aqueous droplet size in a Y-junction and a T-junction,<sup>85</sup> but this study did not explore further than noting poor performance of lecithin compared to Span 80 and PGPR at promoting droplet formation. The factors effecting droplet formation can be difficult to study *in situ*, as the physical properties of the system can be difficult to tune with high precision. As a result of this, computational fluid dynamics (CFD) is an invaluable tool for investigating the process of droplet formation. In CFD, the Navier-Stokes equations, a set of partial differential equations describing fluid flow, are solved computationally (*in silico*). Commonly, the finite element method<sup>86</sup> is employed for this purpose, where geometry describing the system to be studied is broken down into a finite set of points, referred to as a mesh, in which to solve the equations numerically. In this work I employ COMSOL Multiphysics<sup>®</sup>, a general purpose physics software which can model two phase fluid flow in both two and three dimensional space. When supplemented with data describing the physical properties of fluids obtained experimentally, two phase CFD with software like COMSOL<sup>®</sup> provides a reliable approximation of the droplet formation behavior observed on a real microfluidic device, and has been widely employed for this purpose.<sup>69,72,76,87-89</sup> It is common to use two dimensional approximations of three dimensional devices, as a three dimensional model may take orders of magnitude

more computing power to solve than an equivalent two dimensional model; each additional dimension causes the number of points in the mesh to increase exponentially.<sup>90</sup>

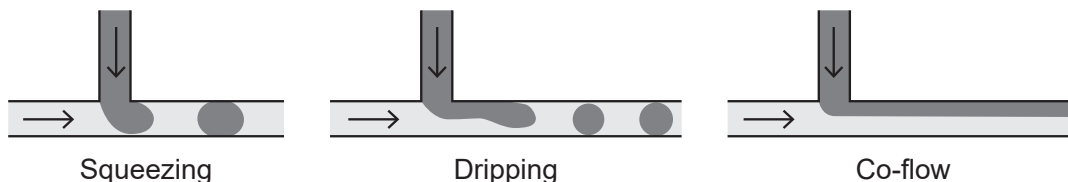
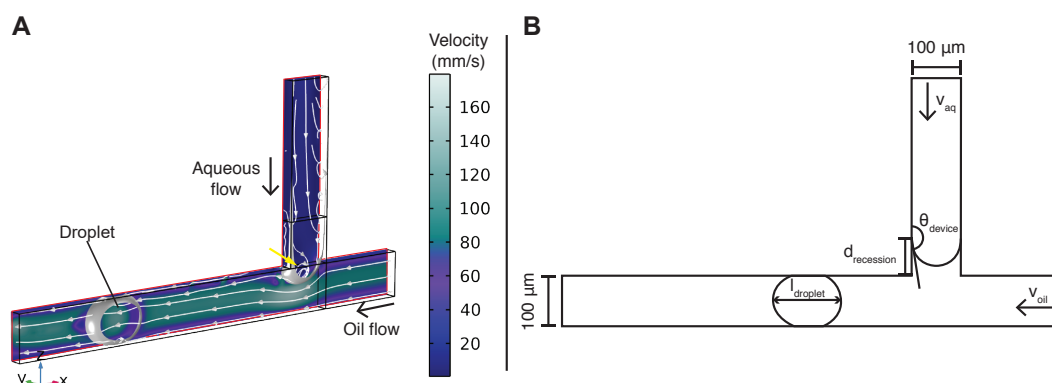


Figure 3.1: **Operation and failure modes of a T-junction.** Dark grey represents the aqueous phase, and light grey represents the oil phase. Arrows indicate the direction of flow. In the squeezing mode of droplet formation, shear forces cause a clean separation of the droplet without sticking to the walls of the device. In the dripping failure mode, the aqueous phase wets to the wall of the device for a length of the main channel before droplets drip off further down the channel. In the co-flow failure mode, shear forces are unable to overcome the surface tension and wetting effects, and the two phases flow alongside each other.

While not generally discussed in the literature, it has been my experience that phospholipids frequently present reliability and longevity challenges for devices made from PDMS. As experiments are carried out, the aqueous phase may begin to wet the walls of the device, leading to erratic droplet formation where the aqueous phase sticks to the walls of the channel and does not cleanly separate into droplets. Two failure modes are shown in Figure 3.1, with one referred to as “dripping”, and the other referred to as “co-flow”. Normally the shear forces present at a T-junction lead to a clean separation of a droplet from the aqueous phase without sticking to the wall, and this intended behaviour is referred to as “squeezing”. The dripping mode failure serves as the primary motivation for this work, as I for the first time examine the process of droplet formation for phospholipid containing solutions on a microfluidic device. I have studied this process using solutions containing the phospholipid DPhPC, which

is the most commonly used lipid for DIB formation. This work will serve to provide insight into the behaviour of phospholipids in DIB systems. Understanding the potential causes of device failure when working with phospholipids will serve to guide amelioration strategies when carrying out DIB experiments on microfluidic devices. Furthermore, quantifying how phospholipids behave as a surfactant during the process of droplet formation through their dynamic surface tension will serve to answer fundamental questions regarding how such devices function. These fundamentals will provide more rigorous guidelines for the typically qualitative process of microfluidic device design for forming DIBs.



**Figure 3.2: Graphical representation of COMSOL<sup>®</sup> model, and key dimensions.** A) Three dimensional perspective rendering of the model in COMSOL Multiphysics<sup>®</sup>, showing results for lipid-out droplet formation during droplet length experiments. The colored velocity field slice is on the same plane as the plane of symmetry which is highlighted in red, and a single droplet can be seen travelling down the channel. Streamlines are shown in with white arrows for direction, also showing convective mixing at the interface between the aqueous and oil phases (highlighted with yellow arrow) B) Key dimensions referred to throughout the text, used to quantify characteristics of droplets formed both *in silico* and *in situ*.

## 3.2 Materials and methods

### Lipid solution preparation

Solutions of DPhPC in either hexadecane or aqueous buffer (HEPES, KCl) were prepared as described previously in Chapter 4<sup>55</sup> from a  $25 \text{ mg mL}^{-1}$  stock solution of DPhPC in chloroform.

### 3.2.1 Microfluidic device fabrication

Microfluidic devices and flat surfaces were fabricated from PDMS as described previously in Chapter 4.<sup>13</sup> The device used was the same as described in Chapter 5, but access ports were punched following the meander section so as to only include the T-junction for study.

### 3.2.2 Equipment for *in situ* experiments

Microfluidic experiments were carried out by mounting the devices on the stage of a Nikon Eclipse Ti2-U inverted microscope. Hexadecane and buffer solutions were dispensed from 1 mL and 100  $\mu\text{L}$  Hamilton gastight syringes respectively on a CETONI neMESYS 290N syringe pump. Fluids were dispensed through lengths of 250  $\mu\text{m}$  inner diameter polytetrafluoroethylene (PTFE) tubing attached to the syringes by 30 gauge blunt luer lock needle tips. Microscope images were captured using a Phantom

VEO 710L high speed camera.

### **3.2.3 Contact angle measurements**

Contact angle measurements were carried out on a DataPhysics TBU90E goniometer by the static sessile drop method.<sup>91</sup> In this method, a drop of the solution to be measured is allowed to drip from a needle onto a surface where it comes to rest. A camera is then used to capture an image of the droplet from the side, and the angle of the tangent line where the droplet contacts the surface is measured. Measurements were carried out in air on a flat PDMS surface. Contact angle measurements were carried out by Genie Lee and Kate Adolph-Hammond.

### **3.2.4 Interfacial tension measurements**

Interfacial tension measurements were carried out on a DataPhysics TBU90E goniometer by the pendant drop method from a 20 gauge needle.<sup>92</sup> In the pendant drop method, a fluid is suspended from a downward facing needle as far as it can go before it drips off. A photo of the suspended droplet is taken from the side. The interfacial tension is then determined by fitting a curve to the profile of the droplet, and mathematically determining the forces inducing that shape, which are an equilibrium between gravity, buoyancy, and the interfacial tension. In all cases, droplets were allowed to equilibrate for 5 minutes before measurement to allow full monolayer formation. In the case of liquid/liquid interfacial tension measurements, the aqueous

droplet was suspended in a cuvette filled with the oil solution. Images were processed using OpenDrop 3.3.0.<sup>93</sup>

### 3.2.5 Fluid dynamics simulations with COMSOL®

The model was developed in COMSOL Multiphysics® 5.6 with the Microfluidics Module on a 64-bit Windows 10 workstation. To build the model, an example model provided in the COMSOL® software package<sup>94</sup> was used as the basis. This base model simulates two phase fluid flow in a microfluidic T-junction in three dimensional space. The fluid interface is modelled by the level-set method;<sup>76</sup> the level-set method is notable for allowing droplets to break off. In order to speed computation time, this model also utilizes a plane of symmetry to simulate only one half of the microfluidic channel. Ricardo Ramírez modified the model with the density and viscosities of hexadecane and water, and the physical dimensions of my microfluidic devices. He then tuned the parameters of the simulation to ensure fast computation times, a stable fluid interface, and that a solution could be converged to by the solver through an iterative process using COMSOL® LiveLink™ for MATLAB®. I modified this optimised model for use in this work. I derived a formula for contact angle of a wetted wall within COMSOL® from Young's equation, which uses contact angles for the oil and aqueous solutions obtained experimentally on PDMS in air. I then incorporated all literature and experimental data for contact angle and interfacial tension into the model, and substituted these as parameters for each experimental condition. The derived equation is shown in Equation 3.2. In this equation,  $\gamma$  refers to interfacial



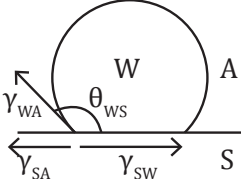
tension, with the two phases for that tension term indicated by the subscript terms Aq (aqueous), Air, and Oil.  $\theta_{Aq}$  and  $\theta_{Oil}$  indicate the contact angles for the aqueous and oil phases as measured on PDMS in air.  $\theta_{Device}$  is the angle at which the fluid interface contacts the walls of the microfluidic device.  $\alpha$ , the inner term of the contact angle calculation, must be between -1 and 1 or else no solution exists for  $\cos^{-1} \alpha$ , thus a piecewise function is used to ensure the model will always have a contact angle that exists, between  $180^\circ$  and  $0^\circ$ , in accordance with the complete non-wetting or wetting which would be expected for a real world system which has  $-1 < \alpha < 1$  respectively. The derivation for this formula is provided in Figure 3.3.

$$\alpha = \frac{\gamma_{AqAir} \cos \theta_{Aq} - \gamma_{OilAir} \cos \theta_{Oil}}{\gamma_{AqOil}}$$

$$\theta_{device} = \begin{cases} 180^\circ & \text{if } \alpha < -1 \\ \cos^{-1} \alpha & \text{if } -1 \leq \alpha \leq 1 \\ 0^\circ & \text{if } \alpha > 1 \end{cases} \quad (3.2)$$

The models were run in parallel on a Linux (v3.10) cluster operated by Compute Canada with a single compute node for each experimental condition and a time step resolution of  $1.25 \times 10^{-3}$  s and  $3.125 \times 10^{-4}$  s for the droplet length and contact angle sweep simulations respectively. The simulation was run over a time window of 0.05 s to 0.1 s depending upon the number of droplets required. All models were run with an oil flow rate ( $v_{oil}$ ) of  $8.333 \mu\text{L min}^{-1}$  and an aqueous flow rate ( $v_{aq}$ ) of  $1.25 \mu\text{L min}^{-1}$ .

**A**



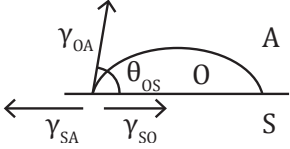
$$\gamma_{SA} = \gamma_{SW} + \gamma_{WA} \cos \theta_{WS}$$

$$- \gamma_{SW} \quad - \gamma_{SW}$$

$$\underline{\gamma_{SA} - \gamma_{SW}} = \gamma_{WA} \cos \theta_{WS}$$

$$\underline{\gamma_{SA} - \gamma_{SW}} = \gamma_{WA} \cos \theta_{WS}$$

**B**



$$\gamma_{SA} = \gamma_{SO} + \gamma_{OA} \cos \theta_{OS}$$

$$- \gamma_{SW} \quad - \gamma_{SW}$$

$$\underline{\gamma_{SA} - \gamma_{SW}} = \underline{\gamma_{SO} - \gamma_{SW}} + \gamma_{OA} \cos \theta_{OS}$$

$$\underline{\gamma_{SA} - \gamma_{SW}} = \gamma_{WO} \cos \theta_3 + \gamma_{OA} \cos \theta_{OS}$$

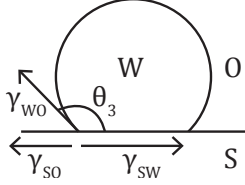
$$\gamma_{WA} \cos \theta_{WS} = \gamma_{WO} \cos \theta_3 + \gamma_{OA} \cos \theta_{OS}$$

$$\gamma_{WO} \cos \theta_3 = \gamma_{WA} \cos \theta_{WS} - \gamma_{OA} \cos \theta_{OS}$$

$$\cos \theta_3 = \frac{\gamma_{WA} \cos \theta_{WS} - \gamma_{OA} \cos \theta_{OS}}{\gamma_{WO}}$$

$$\theta_3 = \cos^{-1} \left( \frac{\gamma_{WA} \cos \theta_{WS} - \gamma_{OA} \cos \theta_{OS}}{\gamma_{WO}} \right)$$

**C**



$$\gamma_{SO} = \gamma_{SW} + \gamma_{WO} \cos \theta_3$$

$$- \gamma_{SW} \quad - \gamma_{SW}$$

$$\underline{\gamma_{SO} - \gamma_{SW}} = \gamma_{WO} \cos \theta_3$$

**Figure 3.3: Derivation of formula for device contact angle from Young's equation.**

Three conditions were used for the derivation. The first condition, A, depicts a water droplet (W) on a solid surface (S) in air (A). The second condition, B, depicts an oil droplet (O) on a solid surface (S) in air (A). Finally, condition C depicts a water droplet (W) in contact with a solid surface (S), but surrounded by oil (O). According to Young's equation, the contact angle ( $\theta$ ) results from an equilibrium between the three interfacial tension force vectors ( $\gamma$ ) where the three phases meet.  $\theta_3$  corresponds to the on-device contact angle. First, Young's equation for all 3 conditions is written out, and the force vector for the interfacial tension between the solid and water ( $\gamma_{SW}$ ) is subtracted from both sides of each. In the resulting equations, the double underlined portion is then substituted into B, in order to eliminate the difficult to measure  $\gamma_{SO}$  from the equations. Equations A and B are both equal to  $\gamma_{SA} - \gamma_{SW}$  (underlined), and therefore are then set equal to each other to eliminate both terms. The resulting equation can then be rearranged to solve for  $\theta_3$ .

A visualisation of the results of a droplet length experiment can be seen in Figure 3.2A, where a droplet has formed in the channel and is indicated. Figure 3.2B shows the key dimensions for the model which will be referred to throughout this text.

### 3.2.6 Droplet length experiments

#### COMSOL<sup>®</sup> simulation of no lipid, lipid-in and lipid-out systems

COMSOL<sup>®</sup> models were prepared with the contact angle and interfacial tension for three systems: hexadecane and water (no lipid), hexadecane and 10 mg mL<sup>-1</sup> DPhPC in buffer (lipid-out), and 10 mg mL<sup>-1</sup> DPhPC in hexadecane and buffer (lipid-in). The surface tension and contact angle for lipid solutions is dependent on the amount of phospholipid which has assembled in a monolayer at the interface/surface, which is a time dependent process. The physical properties data therefore had been collected with time to allow for the surface tension and contact angle to reach equilibrium state. The models incorporated this equilibrium state data to reflect the properties of a system with a fully formed monolayer. The models therefore displayed an idealised version of the morphological changes which could be observed if monolayer formation was faster than droplet formation, and therefore if the surfactant properties of the lipid played a role in this process. Literature values of dynamic viscosity ( $\mu$ ) and density ( $\rho$ ) for hexadecane ( $\mu=3.04$  mPa s,  $\rho=0.770$  g cm<sup>-3</sup>),<sup>95</sup> and COMSOL<sup>®</sup> material library values for water ( $\mu=1.00$  mPa s,  $\rho=1.000$  g cm<sup>-3</sup>) were used. Changes to density for both phases with DPhPC dissolution were ignored, as the mass of DPhPC

dissolved in a  $10 \text{ mg mL}^{-1}$  solution did not exceed 1.5% of the liquid mass, and very large (order of magnitude) changes to density are needed to make a significant difference in the process of droplet formation.<sup>89</sup> Similarly, given the low relative concentration of phospholipid, any changes to viscosity were ignored as they were likely to be considerably smaller than the doubling or halving of magnitude typically needed to measurably effect droplet formation.<sup>96</sup> Interfacial tensions ( $\gamma$ ) for each combination of phases are shown in 3.1, with all values not from the literature collected by Sean Farley. The results of the simulations were post-processed using ImageJ (version 1.52D) to measure the length of the droplets, with channel width as a known reference length ( $100 \mu\text{m}$ ) to calibrate the measurement tool.

Table 3.1: **Interfacial tensions used in the COMSOL<sup>®</sup> model.** Interfacial tensions were determined between the two phases corresponding to the column and row. Values from literature have citations, all others were collected by Sean Farley. Buffer was treated as interchangeable with pure water.

Substance	Air	Hexadecane	Buffer	Hex, DPhPC	Buf, DPhPC
Air		28.12	71.94 <sup>97</sup>	26.05	47.35
Hexadecane	28.12		55.2 <sup>98</sup>		10.89
Buffer	71.94 <sup>97</sup>	55.2 <sup>98</sup>		21.04	
Hex, DPhPC	26.05		21.04		11.47
Buf, DPhPC	47.35	10.89		11.47	

### ***In situ* characterisation of droplets formed with and without lipid**

Microfluidic devices were run under the same conditions that were modelled *in silico*. To ensure the closest similarity in surface properties to the conditions seen *in silico*, only the first 5 droplets formed during each run were used for droplet length measure-

ments. To collect footage of the first 5 droplets, flow on the aqueous pump was first reversed for 90 s to draw the aqueous phase back inside the inlet tubing. Forward flow was then restored, ensuring that the aqueous phase would be flowing at the correct velocity when it once again reached the device and reached the T-junction. The high speed camera was triggered upon formation of the first droplets. Measurements of droplet length were carried out in Phantom CineViewer 3.5.792.0 using the channel width as a known reference length (100  $\mu\text{m}$ ) to calibrate the measurement tool.

### **Statistical analysis of data**

A three level (for the three experimental conditions) one-way analysis of variance (ANOVA) was performed on the *in silico* droplet length and *in situ* droplet length datasets separately, to determine if phospholipid presence had a statistically significant effect on droplet length *in silico* and *in situ*. A two level (for *in situ* and *in silico*) one-way ANOVA was performed to compare each *in situ* droplet length population to its *in silico* counterpart collected under the same conditions, and determine if there was a statistically significant difference between predicted and actual droplet lengths. A two level (for *in situ* and *in silico*) one-way ANOVA was also carried out to compare each lipid-containing *in situ* condition to the no lipid *in silico* condition, to establish if addition of lipid made the droplet length measurably different from that predicted for a no lipid system. For all statistical analyses, the threshold for statistical significance was set at  $p < 0.05$ .

### 3.2.7 Time-resolved surface properties experiments

#### *In silico* sweep of observable contact angles

To determine the relationship between on-device contact angle ( $\theta_{device}$ ) and the degree to which the fluid interface recedes following droplet formation ( $d_{recession}$ ), seven COMSOL<sup>®</sup> models were prepared. Instead of calculating  $\theta_{device}$  using Equation 3.2, these seven models were each hard coded with a numerical contact angle. The chosen contact angles were evenly distributed over the range 120° to 180°, encompassing the full range of values which had been previously determined with Equation 3.2. All models were run using IFT for a hexadecane/water system (55.2 mN m<sup>-1</sup> lit.<sup>98</sup>) to reflect the lack of effect of DPhPC on IFT observed in the droplet length experiments.

#### Device failure time characterisation

Device failure time characterisation was carried out for no lipid, lipid-in and lipid-out at four  $v_{oil}$  each: 33.333  $\mu\text{L min}^{-1}$ , 16.667  $\mu\text{L min}^{-1}$ , 8.333  $\mu\text{L min}^{-1}$ , and 4.167  $\mu\text{L min}^{-1}$ . To keep the flow rate ratio of the phases the same,  $v_{aq}$  for each  $v_{oil}$  was 5.000  $\mu\text{L min}^{-1}$ , 2.500  $\mu\text{L min}^{-1}$ , 1.250  $\mu\text{L min}^{-1}$ , and 0.625  $\mu\text{L min}^{-1}$  respectively.

To quantify time until failure, video footage was recorded with the high speed camera beginning when the first droplets formed, as described for the droplet length experiments. However, rather than collecting only the first 5 droplets, footage was

collected until device failure: when  $d_{recession}$  was too small to observe. The time until failure was determined as the time elapsed between two points: the first frame where the fluid interface reached the T-junction, and the first frame where  $d_{recession}$  appears to be zero.

### 3.3 Results and discussion

#### 3.3.1 Phospholipids do not assemble at the fluid interface fast enough to impact droplet formation

##### Experimental design and criteria of model validity

Validity of the model was verified according to two criteria: if it accurately predicted droplet length under control conditions, and if droplet length was a suitable responding variable for addition of lipid (manipulated variable). The first criteria was verified by treating the no lipid experimental condition as the control. For this control, if the *in situ* and *in silico* droplet lengths were not significantly different (two level ANOVA), this criteria for validity was met. To address the second criteria for validity of the model, it was determined if addition of lipid caused a measurable change in droplet length *in silico* (three way ANOVA). If there was a significant difference between the no lipid, lipid-out and lipid-in droplet lengths, this criteria was met. If the model satisfied both criteria for validity, it would be treated as accurately reporting

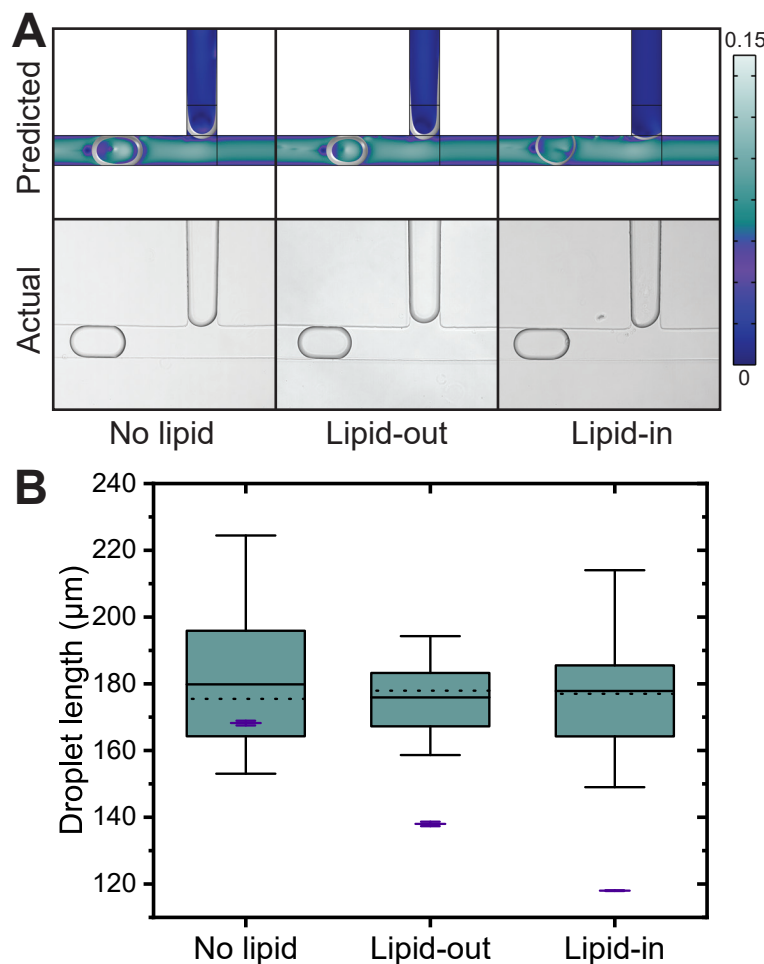


Figure 3.4: **Results of droplet length experiments.** A) Representative examples of droplets formed *in silico* (top) and *in situ* (bottom). Color scale for velocity is the same between *in silico* replicates and is reported in meters per second. *In situ* data did not appear qualitatively different from each other. B) Distribution of droplet lengths observed, with box and whisker plots for *in situ* data ( $n=24$  for each) and predicted lengths superimposed as violet mean and standard deviations ( $n=2$  for each, see future work). Mean is shown on the box and whisker plot as a solid line, and median as a dotted line. As observed qualitatively, there is no clear difference in the typical length of droplets formed under the different *in situ* conditions. The predicted droplet lengths for the no lipid system overlapped with the range of all the *in situ* droplet populations, and is the only condition to do so.



the droplet lengths which would be observed for the idealized conditions (fully formed monolayer) present in the experimental (lipid-out, lipid-in) models. Precedent exists for this idealised model of droplet formation, as previous computational works relating droplet size to interfacial tension typically assume that interfacial tension is a fundamental property of the fluid system, rather than a time-dependent process induced by a surfactant.<sup>69,72,89,99</sup>

To study the behavior of DPhPC *in situ*, I needed to determine if addition of lipid caused a measurable effect on droplet length. This would be done by comparing droplet lengths for the no lipid, lipid-out and lipid-in conditions (three way ANOVA). Next, I would determine if the behaviour of the lipid containing solutions *in situ* reflected that predicted by the idealized model. For each experimental condition, two level ANOVA between the *in silico* and *in situ* results would serve to determine this. This would also indicate whether DPhPC behaved like it would under the idealized *in silico* conditions, and therefore whether DPhPC assembled at the fluid interface fast enough to impact droplet formation *in situ*.

### **COMSOL<sup>®</sup> model satisfies criteria for validity**

Representative samples of both *in silico* and *in situ* data may be seen in Figure 3.4A. In these, a droplet is shown following its formation at the T-junction both *in silico* (predicted) and *in situ* (actual). Two level ANOVA between the *in silico* and *in situ* droplet lengths for the control (no lipid) condition showed no statistically significant difference between them. This satisfied the first criteria of validity, in that the model

accurately predicted droplet length for the control conditions. Three level ANOVA between *in silico* conditions revealed a statistically significant difference between the no lipid, lipid-out, and lipid-in conditions ( $p=7.4^{-6}$ ). This satisfied the second criteria for validity, in that droplet length was a suitable responding variable. More importantly, because the manipulated variables were the physical properties of the phases and interface, it demonstrated that the changes to these properties that would occur under idealized surfactant behaviour had a measurable impact on droplet length. The model was therefore deemed to be valid, and was then used to characterise the *in situ* data.

### **Real world phospholipid solutions behave as if no phospholipid is present**

With the validity of the model established, the *in situ* data could be analyzed. No statistically significant difference was observed between the three *in situ* conditions ( $p=0.72$ ), demonstrating that addition of DPhPC had no measurable effect on droplet length. Two level ANOVA showed statistically significant differences between the *in silico* and *in situ* data for both the lipid-in ( $p=2.0^{-5}$ ) and lipid-out ( $p=7.6^{-5}$ ) conditions. It therefore was determined that *in situ* droplet formation did not reflect that of the equivalent idealized model when lipids were present. It therefore followed that DPhPC does not assemble at the fluid interface fast enough to impact the process of droplet formation by changing the fluid properties as a surfactant. Instead, by carrying out the same two level statistical comparison between the *in situ* experimental (lipid-containing), and *in silico* control (no lipid) conditions, there was no statistically

significant difference observed for either lipid-out ( $p=0.27$ ) or lipid-in ( $p=0.43$ ). This demonstrated that both lipid-out and lipid-in systems behave indistinguishably from the predicted behaviour of a system containing no lipid. Box-and-whisker plots for the *in situ* data can be seen in Figure 3.4B, with *in silico* data superimposed on top. The high level of overlap between the *in situ* data and the *in silico* data for a no lipid system is clearly visible.

### **Analysis of the causes of *in silico* droplet formation behaviour**

The cause of the reduced droplet size observed for lipid containing solutions *in silico* is likely to be primarily due to their reduced interfacial tensions:  $21.04 \text{ mNm}^{-1}$  for lipid-out and  $10.89 \text{ mNm}^{-1}$  for lipid-in (both collected by Sean Farley) compared to the  $55.2 \text{ mNm}^{-1}$ <sup>98</sup> seen without lipid. The droplet lengths observed are proportional to the interfacial tensions present, as lipid-out has the shortest droplets and also the lowest interfacial tension. This is consistent with the literature, as it is known that interfacial tension plays a role in droplet size.<sup>71</sup> It is also known that droplet size decreases with increasing contact angle.<sup>99</sup> This contact angle effect is consistent with the decrease in droplet length observed in the lipid-out conditions, where  $\theta_{device}$  increased from  $157^\circ$  for no lipid to  $180^\circ$  for lipid-out, and the decrease in interfacial tension and increase in  $\theta_{device}$  both would work together to decrease droplet length. However, lipid-in exhibited the smallest droplet length, despite its contact angle being smaller at  $121^\circ$ . The greatest factor effecting droplet length therefore appears to be interfacial tension, as otherwise the contact angle decrease seen with the lipid-in

conditions would very likely lead to droplets being larger than observed, as the effects of contact angle and interfacial tension on droplet size are working in opposition to each other.<sup>71,99</sup> Additional control experiments examining the effect of contact angle in isolation for these reduced interfacial tensions would further solidify this claim, and these are detailed in the future work section.

## Experimental conclusions

The data collected so far served as the justification for me to simplify subsequent time-resolved surface properties experiments, as the effects of interfacial tension on the process of droplet formation could be ignored and assumed equivalent to a system containing no phospholipid. This would serve to simplify my *in silico* sweep experiment to only one dimension (contact angle), vastly decreasing the computational complexity, and making the calculation of a calibration curve feasible. This calibration curve could be used to quantify contact angle on the device visually. Previous work with the natural phospholipids found in soy lecithin support this decision to eliminate dynamic interfacial tension.<sup>85</sup> The inability of soy lecithin containing solutions to form droplets lipid-out at a Y-junction while Span 80 containing solutions did was explained in simplified terms by the poor mobility of lecithin in hexadecane, and therefore a slow drop in interfacial tension relative to Span 80. Alternatively, this may be due to slow monolayer formation lipid-out, previously proposed to be due to a high energetic barrier to the lipids assembling at the fluid interface.<sup>54</sup> Ushikubo *et al.* also noted that under real world conditions, a T-junction did not exhibit a mea-

surable difference in droplets formed for any of the surfactants tested, suggesting that droplet formation at a real T-junction is not necessarily dependent upon manipulation of interfacial tension by surfactants. Monolayer formation for phospholipids on a microfluidic device is generally considerably faster than that observed in bulk solution, due to the convective mixing of the droplet interior and exterior.<sup>54</sup> However the presence of meanders as necessary structures on microfluidic devices for DIB formation demonstrate the long time scales still required for appreciable monolayer formation to occur at the interface between phases. On my devices, droplet formation occurs on timescales of a few milliseconds, considerably less than the time typically spent in a meander. Data for Chapter 4<sup>55</sup> and Chapter 5<sup>13</sup> show that droplets spend several seconds in the meander. In summary, both the literature and my experimental findings confirm that the dynamic interfacial tension of DPhPC does not evolve fast enough to become a factor in droplet formation due to both its low speed of migration in solution and the high energetic barrier to monolayer formation, justifying its elimination as a variable for subsequent simulations.

My results confirm that the qualitative practice of fabricating meanders on microfluidic devices intended for DIB formation is justified. It also highlights the possible pitfalls in extrapolating computational data to the real world, as literature *in silico* determination of the relationship between interfacial tension and droplet size may be misleading when predicting a corresponding droplet size upon addition of surfactant. Instead, my data suggests that researchers should assume that droplet formation behaviour with lipids present will be indistinguishable from droplet formation behaviour without any surfactant at a T-junction, and therefore T-junctions should be designed

for a system containing no surfactant if targetting a specific droplet size. All subsequent model runs were therefore done with the interfacial tension of hexadecane and water ( $55.2 \text{ mN m}^{-1} \text{ lit.}^{98}$ ), and investigation of the effect of phospholipids on PDMS surface properties could begin.

### 3.3.2 Establishment of a visual means to quantify contact angle *in situ*

In order to examine the changes to surface properties during device operation *in situ*, I first had to establish a relationship between contact angle and a measurable reporter value that can be seen visually on a microscope. As seen in Figure 3.4B, droplet length under real world conditions is highly variable and does not have the precision to serve this purpose. Qualitatively, I had observed that as devices developed poor wetting properties *in situ*, the distance that the fluid interface receded following droplet formation appeared to grow shorter. Moreover, I observed that shortly after the recession distance reached zero, the fluid interface began to move further into and down the channel, a critical component of the transition to dripping mode device failure.<sup>82</sup> To test whether this recession distance ( $d_{\text{recession}}$ ) was a suitable reporter value I performed a one-dimensional sweep of device contact angles *in silico* ( $\theta_{\text{device}}$ ) over the range  $120^\circ$  to  $180^\circ$ , and ran each of the models over the window of time needed for three droplets to form. This range was chosen to accommodate the entire range of contact angles seen *in silico* during the droplet length experiments.

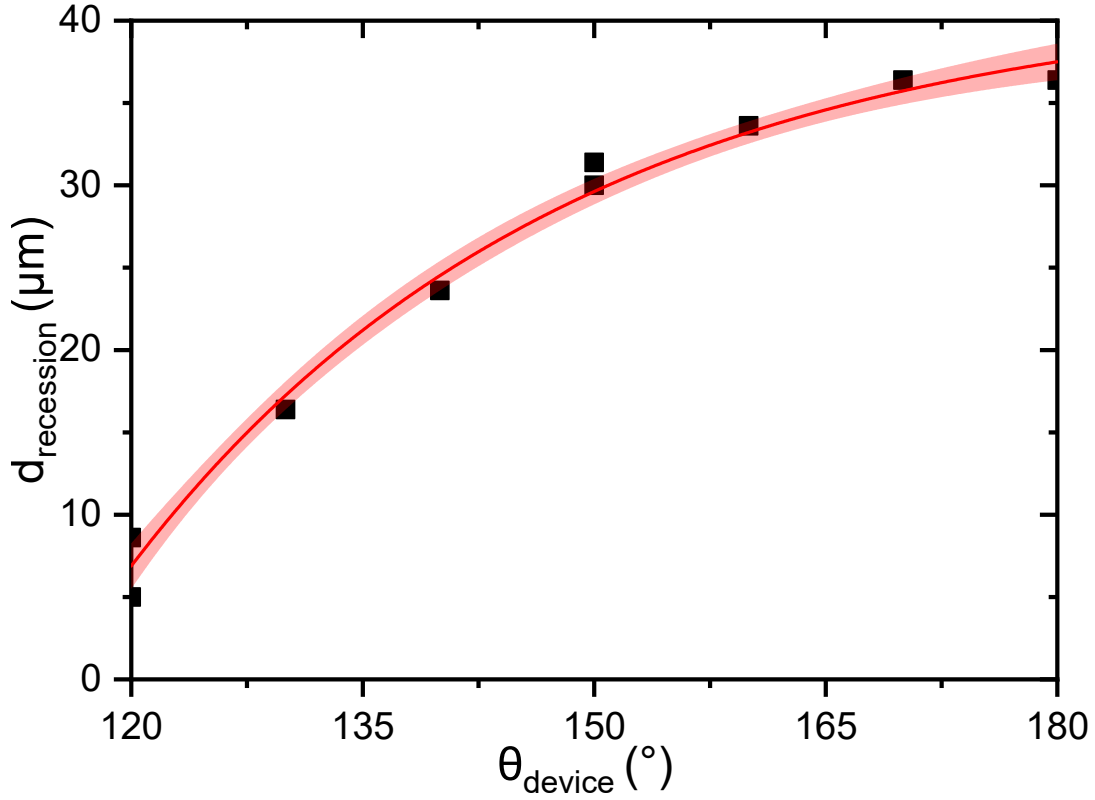


Figure 3.5: **Calibration curve for *in situ* contact angle determination.** This calibration curve shows the relationship between device contact angle ( $\theta_{device}$ ) and the distance receded ( $d_{recession}$ ) by the fluid interface following droplet formation *in silico*. Raw data ( $n=3$ ) is shown in black, curve fit and 95% confidence bands are shown in red. Curve is fitted to an asymptotic equation of the form  $y = a - bc^x$  and has  $R^2 = 0.99$ . The equation for  $d_{recession}$  is shown as Equation 3.3.

$$d_{recession} = 41.67259 - 2420.01548(0.96527^{\theta_{device}}) \quad (3.3)$$

My model showed a high level of correlation between  $\theta_{device}$  and  $d_{recession}$ , which can be seen in Figure 3.5. This figure shows both the raw data for  $d_{recession}$  measured at each  $\theta_{device}$ , as well as a fitted curve. A non-linear, positive relationship exists between  $\theta_{device}$  and  $d_{recession}$  over this range, showing that  $d_{recession}$  is a suitable means of quantifying contact angle visually on microscope images. Equation 3.3 shows the substituted formula for the curve fitted in Figure 3.5, relating  $d_{recession}$  to  $\theta_{device}$ .

The cause of the relationship likely lies in the dynamic process of droplet formation, referred to as breakup. Previous work by Li *et al.* on the mechanism of droplet breakup in a T-junction has shown that the forces contributing to the process are shear force from the oil phase, the interfacial tension, and the hydrostatic pressure drop from one side of the droplet to the other.<sup>69</sup> The point at which droplet breakup occurs is the point at which interfacial tension can no longer overcome the other two forces. Contact angle changes the shape of the fluid interface as it travels through a channel, with high contact angles creating a more curved interface, and lower contact angles having a smaller curvature. Li *et al.* determined that the pressure drop experienced by a droplet as it forms is proportional to the curvature of the interface, meaning lower contact angle systems experience less pressure. Furthermore, a more curved interface enters the channel sooner relative to its trailing edge, experiencing shear force earlier which grows proportionally to how far it extends into the oil channel. Both of these factors combine to encourage earlier droplet separation for higher contact angles, as



the stronger forces overcome the interfacial tension sooner. With earlier droplet separation, less time has passed for more of the aqueous phase to fill its inlet. The result of this is that for higher contact angles, early droplet separation leads to more oil being at the end of the inlet following droplet breakup, and higher observed  $d_{recession}$ .

With this quantitative relationship between  $d_{recession}$  and  $\theta_{device}$  established, I now have access to a means of characterising the surface properties of a microfluidic device during its operation purely visually using microscope images. With this, I will be able to examine the effect of DPhPC on contact angle evolution over time. This will for the first time allow me to gain insight into the mechanisms underpinning microfluidic device failure with phospholipid containing solutions, and guide future amelioration strategies when using microfluidic devices for DIB based pharmacokinetics assays. This work is detailed in the future work section of this chapter, with the following section providing a preliminary picture of the effects of DPhPC on rates of device failure.

### 3.3.3 Lipid containing solutions exhibit enhanced wetting

To determine rates of device failure for no lipid, lipid-out, and lipid-in conditions, I needed to observe my microfluidic devices in operation at several flow rates *in situ*. For this I collected video footage of a microfluidic T-junction from the point when the first droplet was formed, until the point that  $d_{recession}$  became too small to see (ie. approached zero). Using the relationship between  $d_{recession}$  and  $\theta_{device}$  established

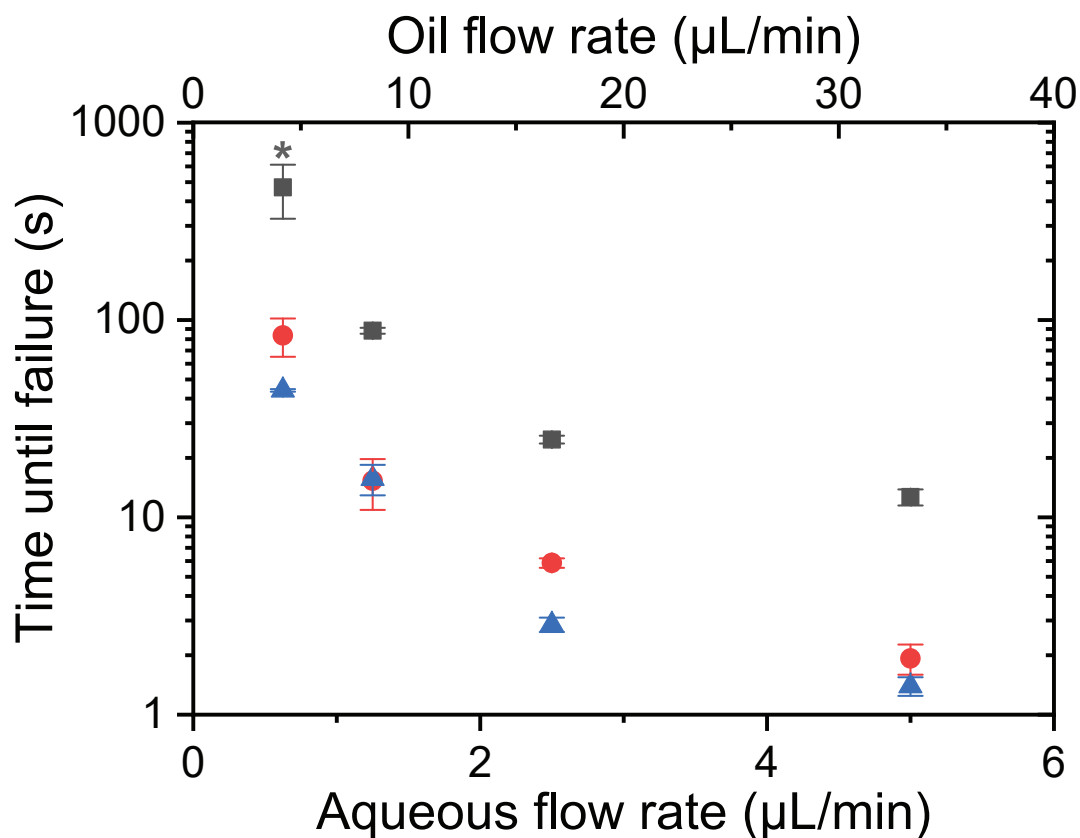


Figure 3.6: **The effect of lipid presence on device longevity.** Device longevity is quantified as time taken for dripping mode failure to occur *in situ*, determined by recession distance dropping to approximately zero. No lipid is shown in black squares, lipid-out in red circles, and lipid-in in blue triangles. The error bars denote standard deviation ( $n=2$ ). The ratio between oil and aqueous phase flow rates was the same across all conditions. While a typically greater longevity was observed for lipid-out conditions over lipid-in, solutions without lipids present had device longevity an order of magnitude greater. The data point marked with an asterisk did not reach failure for either replicate due to the reaching the maximum recording time on the camera. The value recorded is instead the duration of the recording from the first droplet formed to the end of the recording, meaning the actual time until failure is longer.

with my calibration curve, as well as the knowledge that this low  $d_{recession}$  precedes device failure, I could determine the effect that the presence of DPhPC has on time taken until failure: device longevity.

Surfactants are known to coat the walls of PDMS based microfluidic devices during their operation, contributing to their equilibrium surface properties.<sup>82</sup> It is also generally assumed that a surfactant in the aqueous phase has no effect on the surface properties. Given the dogma surrounding the importance of surfactants in creating the desired behaviour of a microfluidic device, I expected the presence of phospholipids to prolong longevity of the device. However I was surprised to find that not only did PDMS devices perform worse with lipid containing solutions at all flow rates, but that there was an order of magnitude decrease in expected lifetime for the device upon introduction of lipids, regardless of which phase the lipids were introduced in. As predicted by previous computational work,<sup>82</sup> increased flow rates lead to faster rates of device failure, likely due to the decreased time permitted between droplets for surface properties to be restored by oil flow. The results of my longevity determination at several flow rates for the no lipid, lipid-out and lipid-in conditions are shown in Figure 3.6. In this figure, the time taken for a device to reach failure is plotted on a logarithmic scale to show the order of magnitude difference for a device without lipid compared to the lipid containing conditions.

My data shows that the behaviour of lipid solutions in PDMS devices is inconsistent with that proposed by Debon *et al*, which predicted that surfactant adhesion to the PDMS device walls, and its subsequent removal by passing droplets was respon-

sible for the deterioration of PDMS hydrophobicity seen with faster rates of droplet formation.<sup>82</sup> Were loss of adsorbed surfactant responsible for deterioration of surface properties under my experimental conditions, lipid containing solutions would inherently provide greater performance than solutions in which no surfactant was present, and simultaneously lipid-out solutions would show improved performance relative to lipid-in solutions due to the lipid being in contact with, and adsorbed to the PDMS. While I did observe the faster rate of failure for lipid-in solutions, the across the board reduction in device lifetime for lipid containing solutions suggests another mechanism drives device failure for phospholipid containing solutions on PDMS microfluidic devices. It also strongly suggests that lipids dosed lipid-in are able to interact with and adsorb to the PDMS, an unexpected behaviour.

I propose instead that the adsorption of DPhPC to the PDMS permits the deterioration of surface properties by a different mechanism, with DPhPC serving as an amphiphilic mediator of water adsorption to the device walls. As PDMS is a hydrophobic network of crosslinked, non-polar dimethylsiloxane moieties, it follows that interaction with the non-polar lipid chains of the DPhPC is likely to be favorable. Indeed, PDMS is known to be exceptionally permeable to non-polar substances, a fact exploited for several analytical techniques.<sup>100</sup> This is in part assisted by the permeable nature of PDMS. If DPhPC were adsorbed to the walls of the device in this manner, the exposed, polar phosphatidylcholine moieties of the phospholipids would permit adsorption of water to the normally hydrophobic PDMS. This effect is likely due to water adsorption rather than the polar nature of phosphatidylcholine itself, as surface property deterioration only begins upon the introduction of water to the device. Fur-

thermore, initial surface properties were fully restored by flooding the device with oil for 3 min, which was carried out between collection of each video to enable the same T-junction to be used. It is known that introduction of water to PDMS can change its surface properties over time as the water is absorbed into PDMS surface.<sup>101</sup> It is by this mechanism alone that the lipid-free system would be expected to degrade. Further experiments to examine the change in contact angle over the course of device failure would provide more clues as to the mechanism of this process in the presence of phospholipids, and this is detailed in the future work section of this chapter.

### 3.4 Future work

Several areas of this work require additional data to confirm my findings and hypotheses. This is particularly the case for the *in silico* droplet length experiments, where computation time required for  $n=3$  droplets under all conditions is high. The no lipid, lipid-in and lipid-out runs for this section therefore all need to be re-run over a longer time window to ensure that 3 droplets are present in each run. Additional control experiments examining the effect of contact angle on droplet length at each set of interfacial tension values are necessary to fully confirm the primary driver of differing droplet length *in silico*. Further *in situ* experimental work for the time-resolved surface properties experiments is also required, as  $n=2$  replicates are insufficient.

The calibration curve shown in Figure 3.5 will be used to carry out the final portion of this work. I intend to use this calibration curve as a tool to quantify changes to

surface properties *in situ*, providing new insight into the changing surface properties of my microfluidic devices as failure occurs, and potentially providing clues as to the mechanism driving this process. In order to extract the recession distance for all data in a reasonable time frame at high temporal resolution, automated image processing of the captured video files must be employed in order to determine the distance in pixels from the channel to the fluid interface in all frames. This will serve to not only make this the first time in which the effects of lipids on microfluidic devices are quantified, but also the first use of this method to quantify surface property evolution over time *in situ*. As microfluidic devices with phospholipids may increasingly be used in the future to carry out pharmacokinetics assays, a greater understanding of the way in which phospholipids interact with these devices will serve to guide their engineering process.

### 3.5 Notes and acknowledgements

COMSOL<sup>®</sup> and COMSOL Multiphysics<sup>®</sup> are registered trademarks of COMSOL AB. The author is not affiliated with COMSOL AB and COMSOL AB has not authorized, sponsored, or approved this work. This research was enabled through support provided by WestGrid ([www.westgrid.ca](http://www.westgrid.ca)) and Compute Canada ([www.computecanada.ca](http://www.computecanada.ca)).

## Chapter 4

# **A bespoke microfluidic pharmacokinetic compartment model for drug absorption using artificial cell membranes**

This chapter serves as the first application of the microfluidic device I developed in Chapter 2 towards studying pharmacokinetics. The work carried out in this chapter was done in collaboration with my colleague Jaime Korner, and was published in Lab on a Chip as a joint first author paper under the title: *A bespoke microfluidic pharmacokinetic compartment model for drug absorption using artificial cell membranes*.<sup>55</sup> My individual contributions to this work are as follows: I designed and developed the

microfluidic device for the formation of ABC droplet triplets, collected the data for the calibration curves, and performed the data normalisation and data analysis. Jaime's individual contributions to this work are as follows: she developed the biomimetic lipid formulations for use in the microfluidic platform, performed the volume and surface area measurements, carried out the measurements of ROI and intensity, and collected the diffusion dataset which was used to prepare this paper. We both contributed equally to the following portions of this work: we performed half the control experiments each, conducted the triplet formation experiments for the quantification of device performance in duplicate, and gathered data for the fluorescence diffusion experiments in duplicate. A former undergraduate student, Alberto Escobar, designed and tested the heating platform used for this chapter and for the research presented in Chapter 5. The paper and its associated electronic supplementary information (included in Appendix B) were written collaboratively by Jaime, Katherine, and myself. This work demonstrated that DIBs could be used to construct artificial cell models using naturally derived biomimetic lipid blends, and that they could be used to model pharmacokinetics with greater accuracy than existing *in vitro* models such as PAMPA.

## 4.1 Abstract

Early prediction of the rate and extent of intestinal absorption is vital for the efficient development of orally administered drugs. Here we show a new type of pharmacokinetic compartment model that shows a threefold improvement in the prediction of



molecular absorption in the jejunum than the current state-of-the-art *in vitro* technique, parallel artificial membrane permeability assays (PAMPA). Our three-stage pharmacokinetic compartment model uses microfluidic droplets and bespoke, biomimetic artificial cells to model the path of a drug proxy from the intestinal space into the blood via an enterocyte. Each droplet models the buffer and salt composition of each pharmacokinetic compartment. The artificial cell membranes are made from the major components of human intestinal cell membranes (L- $\alpha$ -phosphatidylcholine, PC and L- $\alpha$ -phosphatidylethanolamine, PE) and sizes are comparable to human cells ( $\sim 0.5$  nL). We demonstrate the use of the microfluidic platform to quantify common pharmacokinetic parameters such as half-life, flux and the apparent permeability coefficient ( $P_{app}$ ). Our determined  $P_{app}$  more closely resembles that of actual intestinal tissue than PAMPA, which overestimates it by a factor of 20.

## 4.2 Introduction

In this paper, we present a new method for the *in vitro* quantification of passive drug diffusion. We have developed a microfluidic platform to create a new type of pharmacokinetic compartment model using artificial cell membranes created from a phospholipid mixture designed to mimic human cells. The measurement and prediction of pharmacologically relevant processes such as intestinal absorption are key to successful and efficient drug development.<sup>102,103</sup> New drugs take on average 10-15 years<sup>104</sup> to be developed and cost around 2.6 billion US dollars each.<sup>1</sup> Around 30% of drug

candidates fail during testing on animals because we cannot accurately predict their pharmacokinetics.<sup>105,106</sup> Current methods used to predict passive drug transport have limitations including biological dissimilarity, high time and labour input, and lack of control over assay composition.<sup>107–111</sup> We have developed a “slow microfluidic” platform that uses droplets covered in bespoke phospholipid mixtures to form artificial cell membranes that mimic the pathway that drugs follow from the intestine into blood via an enterocyte.

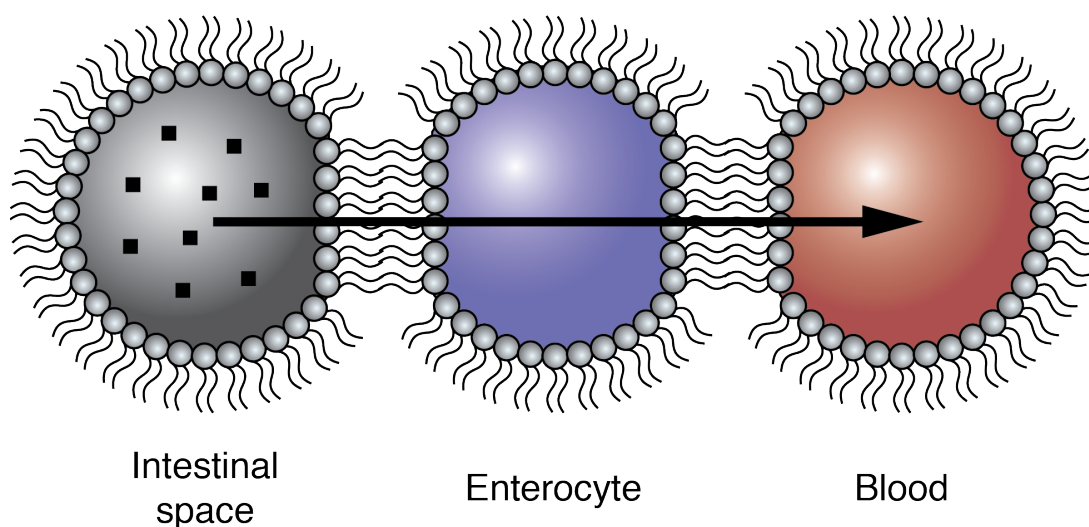


**Figure 4.1: A new type of pharmacokinetic compartment model.** Our *in vitro* droplet-based pharmacokinetic compartment model is designed to mimic the path that an orally administered drug follows from the intestine to the blood. Each compartment is made from a ~0.5 nL microfluidic droplet, where the interior of the droplet represents the compartment itself, and the phospholipid bilayer between the droplets represents an artificial cell membrane. The first droplet (droplet A, grey) mimics the intestinal space, the second droplet (droplet B, purple) mimics an enterocyte and the third droplet (droplet C, red) mimics the blood. Diffusion of a fluorophore (represented in the intestinal space droplet as black squares) occurs in the direction of the arrow.

At present, oral drug absorption is predicted using a variety of *in vitro* methods that range in complexity from cell-based assays to artificial membrane models.<sup>102,103</sup> Drug absorption can occur through both carrier-mediated uptake and passive lipoidal diffusion.<sup>112</sup> With cell-based techniques, the estimation of drug transport through both passive diffusion and carrier-mediated transport can be simultaneous, using supported monolayers of standard cell lines such as Caco-2 or Madin-Darby canine kidney (MDCK) to model transport out of the small intestine.<sup>113,114</sup> Data gathered from these assays are used to calculate apparent permeability coefficients ( $P_{app}$ ) which correlate to *in vivo* fractional drug absorption (F). These cell lines are also able to mimic the physiological properties of enterocytes such as microvilli.<sup>12</sup> Conversely, artificial membrane models, such as liposome-based assays and parallel artificial membrane permeability assays (PAMPA), have other advantages: relatively low labour requirements, the ability to isolate the role of lipoidal diffusion, and tunability, which allows the mimicking of different types of membranes.

Liposomes can be comprised of one<sup>115</sup> or more<sup>116</sup> phospholipids, or even sourced directly from living cell membranes.<sup>117</sup> Results from these assays correlate well with human intestinal absorption in some cases.<sup>115</sup> However, liposome-based predictions of drug absorption rely on the use of bulk solutions, eliminating the potential for the creation of tunable, biomimetic pharmacokinetic compartments. Therefore we focus on the comparison of our model to PAMPA. There is no research to show that the membranes formed in PAMPA resemble true phospholipid bilayers as found in cells. In PAMPA, *in situ* drug absorption occurs through phospholipid-doped plastic filters placed in 96-well plates.<sup>10</sup> The lipid composition can be customised, and the pH in

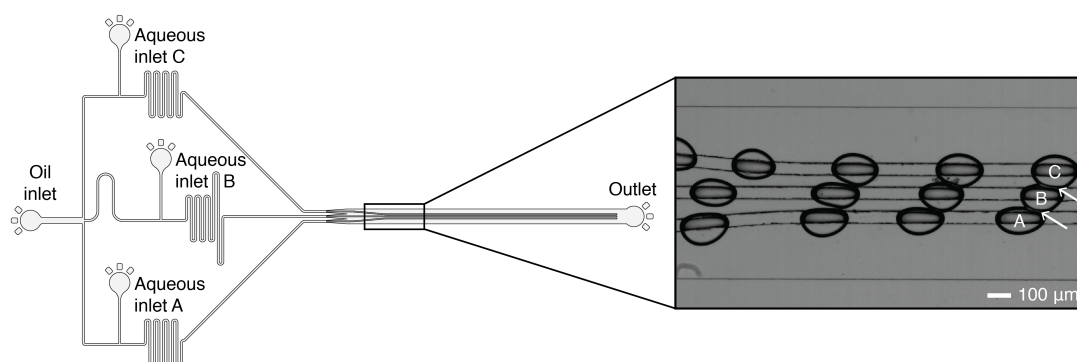


Figure 4.2: **Microfluidic platform.** Design of the “slow microfluidic” platform for the formation of ABC droplet triplets. The device schematic shows the three separately controlled aqueous inlets (A, B and C) used for the formation of three different aqueous droplets at three T-junctions. Each droplet represents a compartment in the pharmacokinetic model. To equilibrate the pressure in the system, a single oil inlet is used and the length of each channel is the same before and after each T-junction. Stabilisation of the lipid monolayer covered aqueous droplets occurs as they travel through the meanders, and bilayer formation occurs when the rails guide the droplets into contact with each other. Each DIB represents an artificial cell membrane between each compartment. The inset is a photograph showing the formation of ABC DIB triplets in parallel using the rails. The continuous phase is squalene and aqueous droplets contain 10 mM HEPES, 140 mM KCl and  $10 \text{ mg mL}^{-1}$  DPhPC at pH 6.5. Arrows highlight the artificial cell membranes formed between the droplets. A video of the microfluidic platform in use is provided in the Electronic Supplementary Information.

the donor and acceptor compartments on either side of the filter can be tuned to mimic physiological conditions in specific tissues, which is a vital parameter in assessing the transport of ionisable compounds.<sup>118</sup> Concerns have been raised regarding the disproportionate thickness of the plastic filter used ( $\sim 125 \mu\text{m}$ )<sup>119</sup> in comparison to the thickness of a cell membrane ( $\sim 5 \text{ nm}$ )<sup>120</sup> as well as the presence of organic solvent in the interior of the phospholipid “membrane”.<sup>119</sup>

Our artificial cell membranes are based on droplet interface bilayers (DIBs), which

are lipid bilayers created by bringing two aqueous droplets covered by lipid monolayers into contact (Figure 4.1). Since they were first created,<sup>37,38</sup> DIBs have almost exclusively been made with the archaeal phospholipid 1,2-diphytanoyl-*sn*-glycero-3-phosphocholine (DPhPC), with a handful of exceptions, including soy<sup>45</sup> and *E. coli*<sup>121</sup> total lipid extracts. Here we show the first example of DIBs with human-mimicking phospholipid compositions.

Many different methods for the formation of DIBs using microfluidic technologies<sup>61,122</sup> have been developed since we published the first high-throughput method in 2010.<sup>40</sup> Lipid bilayers can also be formed in chambers in microfluidic platforms.<sup>123–125</sup> However, these methods cannot form multiple compartments of cell-scale droplets using human-mimetic phospholipid compositions in high-throughput. Therefore we have designed a new channel-based droplet microfluidic technology where a high level of control over fluid flow rates and droplet position are prioritised. To enable the prediction of pharmacologically relevant drug absorption in this *in vitro* platform, there are three design constraints. Firstly, the platform must be capable of forming droplet triplets of three different compositions, ABC, where A, B and C denote the different compartments in the pharmacokinetic model. Secondly, each droplet should be cell-scale and formed in high-throughput with high reproducibility. And finally, the platform design and surrounding equipment should be simple, to enable replication in other laboratories.

In our platform (Figure 4.2), three different types of ~0.5 nL droplets are created and brought into contact with each other to form DIBs using rails in parallel at a rate of

0.5 Hz. Rails were first used for guiding droplet movement in series in microfluidic devices by Abbyad *et al.*<sup>126</sup> and for DIB formation by Carreras *et al.*, who use the rails to direct droplets for the formation of AB chains of DIBs in series.<sup>65</sup> In comparison, the novel use of three parallel rails allows us to control the flow of droplets into triplet DIB networks and has the potential to allow parallel assays to be performed in the same on-chip structure. Once a triplet is formed, we use a pressure pump to instantly stop the flow for assay quantification without the need for any other on-chip features such as pillars<sup>41</sup> or electromagnetic valves.<sup>63</sup> For comparison, Czekalska *et al.*<sup>63</sup> were able to form one DIB ABCD network at a time and hold it in place for measurements using droplets that were approximately 500 nL in size at a rate of approximately one per minute. Also noteworthy is the microfluidic platform developed by Schmidt *et al.*<sup>41</sup> using approximately 5 nL AB droplets in series and the synthetic lipid 1,2-dioleoyl-*sn*-glycero-3-phosphocholine (DOPC) to measure the permeability of caffeine. Schmidt *et al.* do not report a formation rate and their platform relies on pillars and manually activated oil-withdrawing channels to form DIBs, which limits the potential for automation and increased throughput. The DIBs themselves are formed using a formulation composed of a single (synthetic) phospholipid, whereas cell membranes are usually formed of a formulation of many different types of phospholipids.<sup>127</sup> Other microfluidic platforms for the formation of DIBs are also flow-based, but only able to form networks of ABAB configuration.<sup>40,64</sup> Our platform allows us to form multiple pharmacokinetic assays simultaneously using only a pressure pump with a fast response time and one pressure channel per droplet type.

We have used our microfluidic platform to create a droplet triplet that mimics the

path that an orally administered drug follows from the intestine to the blood (Figure 4.1), with droplet A mimicking the intestinal space, droplet B mimicking an enterocyte and droplet C mimicking the blood. Pharmacokinetic compartment models describe tissues as mathematical compartments, simplifying the prediction of the distribution of drugs in the body. A single-compartment model treats the body as a single space, assuming that the administered drug is uniformly distributed, while a multicompartmental model integrates tissue-specific rates of absorption and distribution into these calculations.<sup>128</sup> Here we present a new type of pharmacokinetic compartment model, using droplets to model human tissues which are relevant to the absorption of orally administered drugs while maintaining important properties such as pH, ionic strength and phospholipid composition. The interior of each droplet is a buffer (Table 4.1) that mimics the pH and salt composition of each these compartments<sup>129–131</sup> and the artificial cell membrane between each droplet is an equal mixture of the phospholipids L- $\alpha$ -phosphatidylcholine (PC) and L- $\alpha$ -phosphatidylethanolamine (PE), a pared down version of the lipid formulation used in PAMPA assays to mimic the small intestine,<sup>132</sup> since these are the major components of intestinal cell membranes.<sup>133–139</sup> The droplet size mimics the volume of human cells<sup>140</sup> and is within two orders of magnitude of the size of human enterocytes<sup>141–143</sup>. Most importantly, the size of droplets formed is ten times smaller than the smallest droplets used in the literature for DIB diffusion quantification.<sup>41</sup> This microfluidic platform allows the quantification of the passive diffusion of fluorescein, which is commonly used as a drug proxy in release studies,<sup>144–147</sup> from the intestinal compartment to the blood compartment. Our new *in vitro* technique for the quantification of drug absorption of orally administered drugs

provides an alternative to PAMPA for the determination of fluorescent drug absorption rates. Our method preserves the compartment model seen in PAMPA, but replaces the thick, lipid-filled membrane with a biomimetic lipid mixture that mimics that found in human cells. We also preserve the differing rates of diffusion seen with different ionisation states of a drug in the gastrointestinal tract.

## 4.3 Materials and methods

### 4.3.1 Materials

1,2-diphytanoyl-*sn*-glycero-3-phosphocholine (DPhPC,  $\geq 99\%$  pure) was purchased from Avanti Polar Lipids. Sodium phosphate dibasic and sodium phosphate monobasic were purchased from Fisher Scientific. Sodium chloride and sodium carbonate were purchased from Bio Basic. L- $\alpha$ -phosphatidylcholine (PC,  $\geq 99\%$  pure, bovine liver), L- $\alpha$ -phosphatidylethanolamine (PE,  $\geq 97\%$  pure, bovine liver), squalene ( $\geq 98\%$  pure), 4-(2-hydroxyethyl)-1-piperazineethanesulfonic acid (HEPES,  $\geq 99.5\%$  pure), trimethylchlorosilane ( $\geq 99\%$  pure), sodium fluorescein (BioReagent, suitable for fluorescence), potassium hydroxide, hydrochloric acid ( $\geq 36.5\text{--}38\%$ ) and potassium chloride ( $\geq 99\%$  pure) were purchased from Millipore Sigma. Polydimethylsiloxane (PDMS, Dow Sylgard 184) was purchased from Ellsworth Adhesives. Acetate masks were printed at  $10\mu\text{m}$  resolution by CAD/Art Services Inc. Silicon wafers (100 mm diameter) were purchased from Silicon Materials. SU-8 3050 and developer were



purchased from MicroChem. Polytetrafluoroethylene (PTFE, 1/16" outer diameter, 250  $\mu\text{m}$  inner diameter) tubing was purchased from Chromatographic Specialties Inc.

### 4.3.2 Design and fabrication of the microfluidic platform

Microfluidic devices (Figure 4.2) have two layers. The first layer contains the channels and geometries used for the formation of the three different types of droplets used to model each pharmacokinetic compartment. The second layer contains the rails, which are 50  $\mu\text{m}$  apart. The three rails encourage the three aqueous droplets covered with a phospholipid monolayer to come into contact to form an artificial cell membrane at the points of interaction. The 5° angle of the rails means that the droplets can be brought into contact at a slow speed of approximately 40  $\mu\text{m s}^{-1}$ . The layers were designed using AutoCAD (Autodesk, 2018, see Electronic Supplementary Information) and printed onto acetate to create positive photomasks. A  $50 \pm 2 \mu\text{m}$  layer of the negative photoresist SU-8 3050 was spin-coated onto a silicon wafer, and the edgebead was removed with a stream of acetone. The wafer was subjected to a soft bake (5 min at 35 °C, 2 min at 65 °C and 30 min at 95 °C), and subsequently exposed to UV light (11.2 s, 19.96 mW/cm<sup>2</sup>, OAI Model 800 mask aligner) through the first photomask. A second layer was spincoated, softbaked, aligned and exposed to UV using the same parameters and the second layer photomask. Development removed the unexposed, non-crosslinked SU-8, and adhesion of the SU-8 features was accelerated by a final hard bake (30 min at 200 °C) and a third UV exposure (90 s, 19.96 mW/cm<sup>2</sup>).

Trimethylchlorosilane (50  $\mu$ L) and the wafer mould were placed under vacuum for 1 h to ensure the deposition of a thin film of silane on the surface of the wafer. PDMS base and curing agent were mixed together in a 10:1 ratio, poured over the aforementioned mould, degassed for 1 h under vacuum to remove any air bubbles introduced during mixing, and cured overnight at 65°C. The cured PDMS was then peeled from the mould. Inlets and outlets for each device were punched using a 1 mm biopsy punch. To create the base of the device, a 10:1 mixture of PDMS base and curing agent was mixed, degassed and spincoated at 1200 rpm for 25 s onto the surface of glass microscope slides to create a thin layer. Both the PDMS devices and the coated glass slides were washed with soapy reverse osmosis (RO) water, rinsed with RO water, isopropyl alcohol, ethanol and Milli-Q water, blown dry with filtered air, baked at 90 °C for 30 min, treated with air plasma (Diener Electronic, Zepto ONE, 37 s, 29 W, 1.75 mbar) to activate the surfaces and placed into contact with each other to bond the surfaces together. The microfluidic devices were then stored at 65 °C for a minimum of 48 h prior to use.

### 4.3.3 Preparation of lipid solutions

Chloroform was removed from the lipid stock solutions by placing 10 mg (400  $\mu$ L of a 25 mg mL<sup>-1</sup> solution dispensed using a P1000 Gilson pipette) of lipids in a 10 mL glass roundbottom flask, and rotating the flask under a stream of nitrogen gas to create a thin film. The flask was then placed in a desiccator under vacuum for 1 h to remove residual solvent. For DPhPC solutions, 1 mL aqueous buffer (buffer compo-

sition is the same as that of the intestinal space in Table 4.1) was then added and the flask was vortexed to resuspend the lipids. After freezing and thawing 5 times using liquid nitrogen and warm water, the lipids were extruded 21 times through a 0.1  $\mu\text{m}$  polycarbonate membrane (Avanti Polar Lipids) at room temperature. For 1:1 PC:PE solutions, 1 mL of squalene was added to the flask, which was then vortexed for 30 s and stirred at 50  $^{\circ}\text{C}$  until the phospholipids dissolved. The final concentration was 5  $\text{mg mL}^{-1}$  PC and 5  $\text{mg mL}^{-1}$  PE in squalene. For absorption experiments, 100  $\mu\text{M}$  fluorescein sodium was added to the buffer.

Table 4.1: **Composition of the buffers used for each pharmacokinetic compartment.**

Droplet designation	Buffer	Salt
Intestinal space <sup>129,148</sup>	10 mM $\text{Na}_2\text{HPO}_4$ , pH 6.5	140 mM KCl
Enterocyte	10 mM HEPES, pH 7.4	140 mM KCl
Blood <sup>149</sup>	10 mM $\text{Na}_2\text{CO}_3$ , pH 7.4	140 mM NaCl

#### 4.3.4 Operating parameters of the microfluidic platform

For all experiments, devices were mounted in a custom-made heating platform set to 37  $^{\circ}\text{C}$  (see the ESI for further details) on the stage of either a Nikon Eclipse Ti2-E or a Nikon Eclipse Ti2-U inverted microscope for visualisation. Brightfield images for statistical analysis were collected using a Motion Blitz EoSens Cube7 or a Phantom VEO 710L high speed camera. Fluorescence and brightfield images for fluorescence experiments were captured using a Hamamatsu ORCA-Flash4.0 V3, with a Solis 1C cold white LED (Thorlabs) and a GFP SemrockBrightline large field of view filter cube (Nikon).

Reagents were introduced into the microfluidic devices using an Elveflow OB1 MK3 pressure pump, four 1.5 mL Eppendorf tubes as reservoirs and four matched lengths of PTFE tubing. Squalene and aqueous buffers were introduced to the microfluidic device by applying a pressure of 100 mbar to 140 mbar to the squalene reservoir, and a pressure of 60 mbar to 100 mbar to each of the aqueous reservoirs. Following equilibration, the main chamber was monitored in Motion Blitz Director for quantification of device performance, and NIS Elements Advanced Research (Nikon, version 5.11.01) for fluorescence data collection. Following formation of a triplet for a fluorescence experiment, flow was stopped from all reservoirs from within the Elveflow control software. Typical droplet speeds were approximately  $450 \mu\text{m s}^{-1}$ , allowing this full stop to be done without the use of triggers.

The speed at which droplets are brought into contact with each other is crucial for the formation of stable artificial cell membranes, and this is especially true when using phospholipids below their phase transition temperatures, as we do here. The response time of the pressure pump means that the flow can be stopped within 130 ms of when an ABC droplet triplet forms and the assay starts. We are therefore able to accurately determine the initial time point of the assay and to discard substandard triplets.

#### **4.3.5 Fluorescence data collection**

Once ABC droplet triplets formed and the flow was stopped, brightfield and fluorescence images were taken every 10 s with a 300 ms exposure time until experiment ter-

mination. Quantification of fluorescence intensity was performed via time-based measurement of mean intensity in regions of interest (ROIs) within each droplet in each frame using NIS Elements. Fluorescence intensity data was normalised for phospholipid bilayer surface area and droplet volume. To do this, bilayer diameters and droplet semi-axes were measured using, respectively, the “Distance Measurement” and the “Measurements and Annotations” modules in NIS Elements. Subsequent calculations were performed by approximating artificial cell membrane surface area as ellipses and droplet volumes as ellipsoids. Each graph in this paper represents the replicate of 5 experiments conducted on 5 different microfluidic devices. Figure B.1, Figure B.2 and Figure B.3 in the ESI provide detailed information about the ROI selection, the quantification of fluorescence intensity, volume calculations and data normalisation for the artificial cell membrane surface area and droplet volume.

#### **4.3.6 Quantification of microfluidic device performance**

To quantify the performance of the microfluidic devices, squalene was pumped into the oil inlet and DPhPC in buffer was pumped into each of the three aqueous inlets with the pressure pump in constant pressure mode. Assessment of the efficacy of ABC DIB triplet formation on the platform was performed using DPhPC to allow for comparison with other DIB forming methodologies in the literature. After letting the flow equilibrate, the high-speed camera was centered on the main chamber, and 60 s of footage were captured for each replicate. The number of ABC DIB triplets formed in each sequence was counted, as summarised in Table 4.2. The total number of droplets

forming triplets was then determined as a percentage of the total number of droplets passing through the field of view. To show the robustness of our method, two sets of two replicates each were carried out, with a different researcher carrying out each set on separate days. For each replicate, a different microfluidic device was used. Statistical analysis indicated that triplets could be formed at a rate of  $0.5 \pm 0.1$  Hz and that  $45 \pm 8\%$  of droplets entering the rail section of the platform were able to form triplets. No precedent for reproducibility exists in the literature, so these may serve as a benchmark by which throughput and reproducibility of DIB forming methodologies (both microfluidic and not) may be assessed.

Table 4.2: **Statistical data used to quantify device performance.** All replicates were collected from 60 s of video captured at 30 frames per second. Triplets were counted from the beginning of the captured video and the number of triplets ( $n$ ) for each experimental repeat are shown in the first column.

$n$	Formation rate	Oil pressure	Aqueous pressure
34	0.57 Hz	120 mbar	113 mbar to 115 mbar
32	0.53 Hz	120 mbar	113 mbar to 115 mbar
26	0.43 Hz	100 mbar	90 mbar to 95 mbar
18	0.30 Hz	100 mbar	90 mbar to 95 mbar

## 4.4 Results and discussion

### 4.4.1 A new *in vitro* model for intestinal absorption

The time-resolved diffusion of fluorophore between pharmacokinetic compartments A, B and C may be seen in Figure 4.3. Timepoints are chosen to show when the flu-

orophore is concentrated in the intestinal compartment A ( $t = 0$  s), a mid-assay time-point ( $t = 420$  s) where the fluorophore is concentrated in the enterocyte compartment B, and the endpoint of the assay ( $t = 1800$  s). All data were gathered at physiological temperatures ( $37^{\circ}\text{C}$ ).

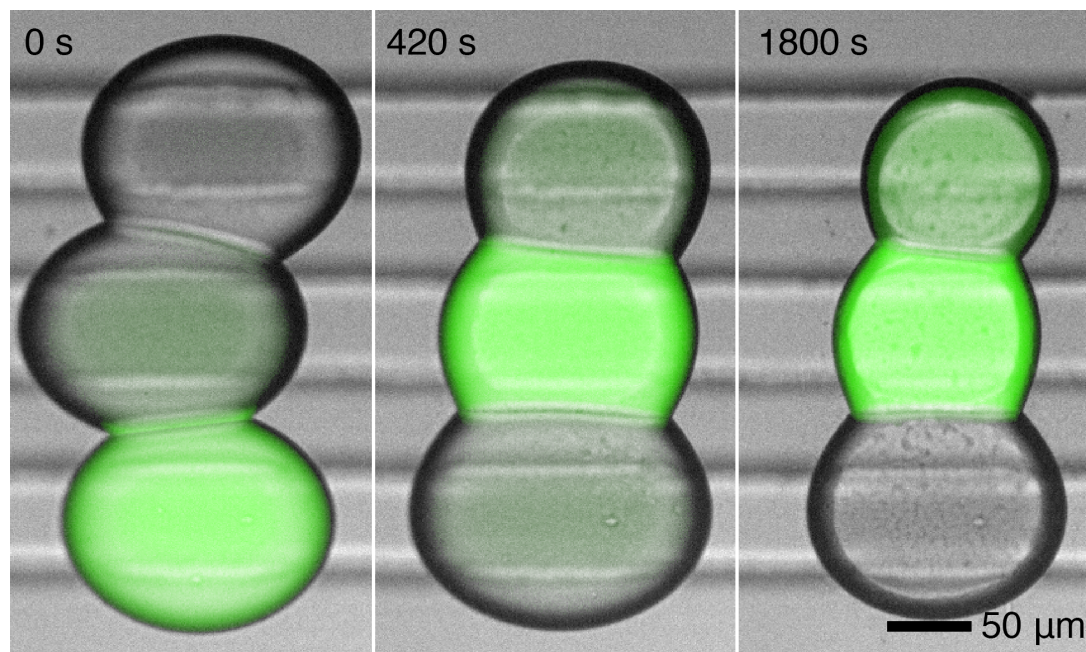


**Figure 4.3: Images of fluorophore diffusion.** Composite brightfield and fluorescence images showing the diffusion of fluorophore from the droplet that represents the intestinal space in the pharmacokinetic compartment model ( $t = 0$  s, bottom, droplet A), to the droplet that represents an enterocyte ( $t = 420$  s, middle, droplet B), after which it continues diffusing into the droplet that represents blood ( $t = 1800$  s, top, droplet C). The fluorophore in the fluorescence images has been tinted green to aid visualisation. Brightfield and colour intensity-corrected fluorescent images were exported from NIS Elements and overlaid with a screen blending mode. Brightness was raised to visible levels by applying a lookup table.

Figure 4.4 shows the change in fluorophore concentration over time for each compartment in the system. Given the well-known nature of PDMS and its effects on

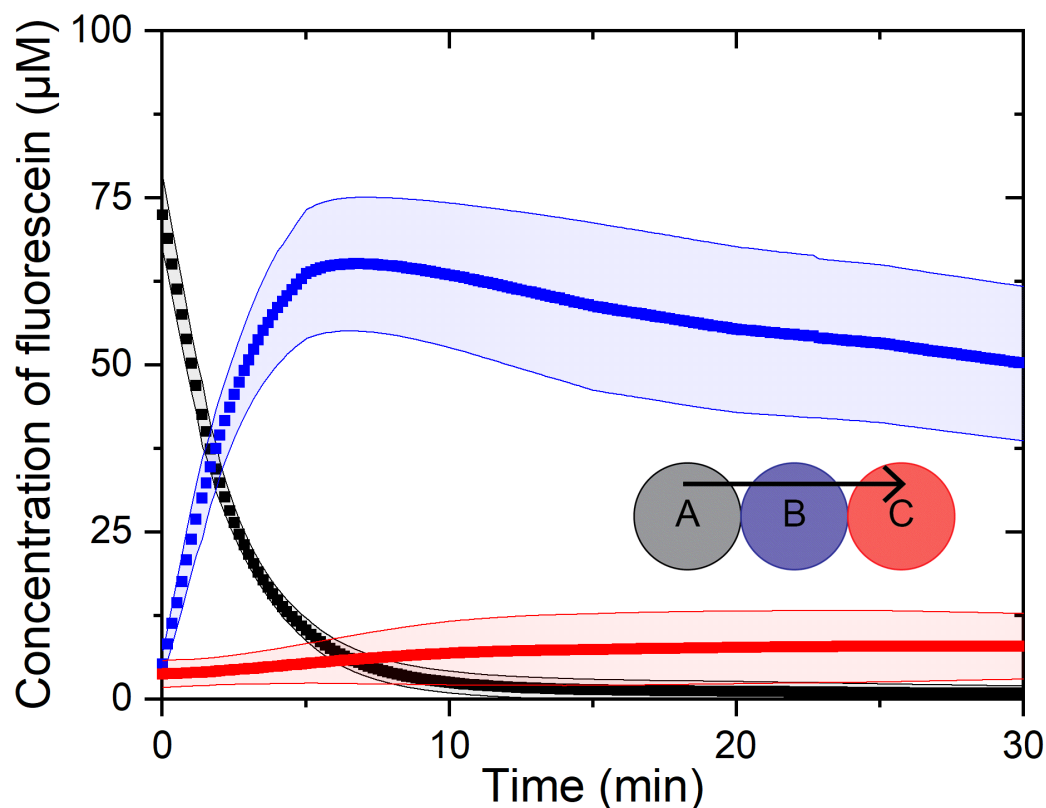


Figure 4.4: **Fluorophore diffusion over time.** Normalised concentration curves for each pharmacokinetic compartment in the droplet triplet model over 30 minutes. The fluorophore is initially concentrated in the droplet representing the intestinal space, A, but rapidly diffuses through the artificial cell membrane into the droplet representing an enterocyte, B, and slowly diffuses through the artificial cell membrane into the droplet representing the blood, C. 95 % confidence bands were calculated from the standard deviation for each timepoint, where  $n = 5$  using 5 different microfluidic devices.

droplet behaviour,<sup>150</sup> intensity measurements were first scaled based on changes in droplet volume over the course of the experiment, due to either evaporation or osmosis, using Equation 4.1, where  $I_s$  is the scaled intensity,  $I_t$  is the intensity at time  $t$ , and  $V_t$ , and  $V_0$  are the droplet volumes at times  $t$  and 0 respectively. To determine con-



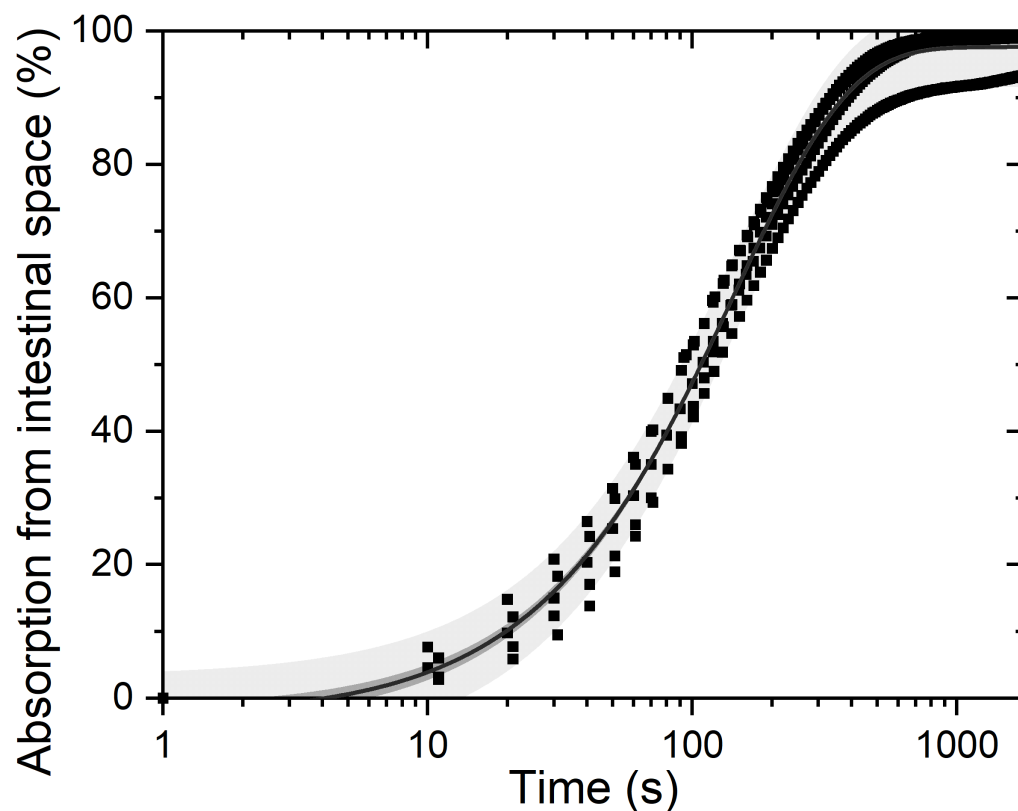


Figure 4.5: **Fluorophore absorption over time.** Absorption of fluorophore from the intestinal space compartment A, into the enterocyte compartment, B, shown as the percentage of fluorescence decrease from initial intensity. The fitted curve and narrow confidence band allow the prediction of the half-life of the fluorophore in the intestinal space compartment with a 2 % relative standard deviation.

centration and account for pH-dependent changes in fluorophore intensity, calibration curves were generated for fluorescein in each buffer and a linear fit was calculated using OriginPro 2019b. Concentration was then calculated from the fitted curve using the scaled intensity measurements. Calibration curves (Figure B.4, Figure B.5 and Figure B.6) and additional experimental information are provided in the ESI.

$$I_s = I_t \frac{V_t}{V_0} \quad (4.1)$$

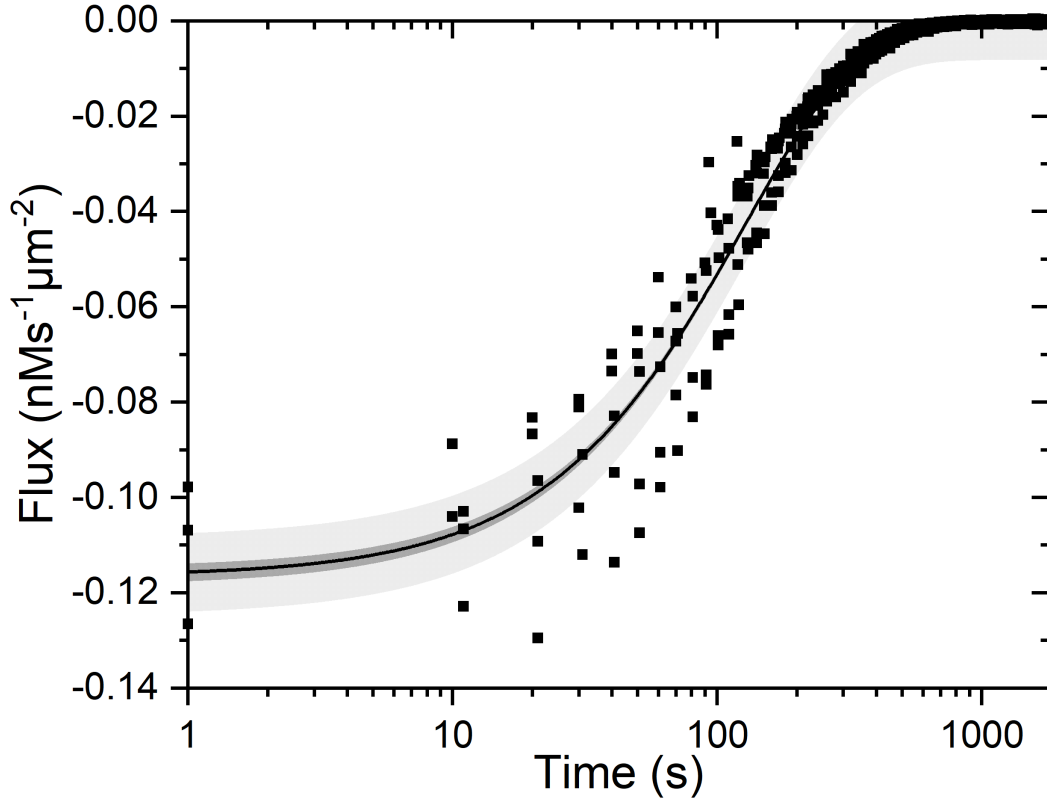


Figure 4.6: **Fluorophore flux over time.** Flux of fluorophore from the intestinal space compartment, A, into the enterocyte, B, calculated using Equation 4.2. Maximum flux may be determined using the fitted curve, providing a measurement of the permeability of the artificial cell membrane to the fluorophore.

Figure 4.5 shows the absorption of the fluorophore from the intestinal space compartment A into the enterocyte and blood compartments, B and C. The rapid absorption of the fluorophore from the intestinal space into both the enterocyte and the blood can be clearly seen. To find the half-life ( $t_{1/2}$ ) of the fluorophore in the intestinal space,

an exponential curve of the form  $y = a - bc^x$  was fitted to these data in OriginPro. This curve fitting found the parameters  $a = 0.976 \pm 0.001$ ,  $b = 1.004 \pm 0.007$ , and  $c = 0.99311 \pm 0.00005$ . The slope of the intensity curve gives the diffusion rate. From this curve a  $t_{1/2}$  of  $108 \pm 2$  s was determined.

The accuracy of this technique was improved by accounting for the area dependence of diffusion rates through the artificial cell membrane. This flux was calculated using Equation 4.2, where  $j_t$  is the flux at time  $t$ ,  $\Delta C/\Delta t$  is the momentary slope ( $C$  is concentration), and  $A_{DIB,t}$  is the measured artificial cell membrane area at time  $t$ .

$$j_t = \frac{\Delta C}{\Delta t} \frac{1}{A_{DIB,t}} \quad (4.2)$$

The flux of all five runs is plotted in Figure 4.6. Following curve fitting the  $y$ -intercept,  $j_{max}$ , was calculated to be  $-0.117 \pm 0.002 \text{ nMs}^{-1}\mu\text{m}^{-2}$ .

#### 4.4.2 Correlation to cell-based assays

Our method is three times better at predicting  $P_{app}$  of actual intestinal tissue than PAMPA. For direct comparison with literature permeability values for fluorescein, we adapted the equation for the  $P_{app}$  used by Berginc *et al.*<sup>151</sup> We treated the system as a two-compartment model, allowing us to treat diffusion out of the intestinal space (droplet A) as having the same magnitude as diffusion into the enterocyte (droplet B). This gives Equation 4.3, where  $\Delta C/\Delta t$  ( $\mu\text{M}/\text{s}$ ) is the maximum rate of diffusion

out of droplet A,  $V$  ( $\text{cm}^3$ ) is the initial volume of droplet B,  $C_0$  ( $\mu\text{M}$ ) is the initial concentration of droplet A, and  $A$  ( $\text{cm}^2$ ) is the maximum artificial cell membrane surface area.

$$P_{app} = \frac{-\Delta C_{max}}{\Delta t} \frac{V}{C_0 A} \quad (4.3)$$

We found  $P_{app}$  to be  $5.6 \pm 0.7 \times 10^{-5} \text{ cm s}^{-1}$ . PAMPA assays carried out previously by Berginc *et al.*<sup>151</sup> found  $P_{app}$  for fluorescein to be  $16 \pm 3 \times 10^{-5} \text{ cm s}^{-1}$  with pH 6.5 and 7.5 in the donor and acceptor compartments respectively, which is a whole order of magnitude higher than our value. However when they performed this absorption assay using rat jejunum under the same pH conditions we used they found  $P_{app}$  to be  $0.8 \pm 0.1 \times 10^{-5} \text{ cm s}^{-1}$ .

### 4.4.3 Control experiments

Direct comparison of the fluorophore intensity between the compartments is complicated by matrix differences since the composition of the droplets was customised to mimic specific biological compartments using different buffering agents and salts. Interestingly, there was a very narrow spread of data for the fluorophore leaving the intestinal space compartment (droplet A), but a wider spread of behaviours upon entering the enterocyte and blood droplets (droplets B and C). This can be seen as a wider spread in Figure 4.4 for these compartments. Control experiments were performed to assess the matrix effect, which was easily done with this microfluidic platform. In

these control experiments, the fluorophore was always dosed in droplet A (the intestinal space), but the composition of the triplet was varied to allow a different diffusion pathway in each case, namely: AAA, BAC, ABB, ACC and ACB, where B represents an enterocyte and C represents the blood (see Figure B.7 in the ESI for data).

As expected, complete fluorophore equilibration was observed when all three compartments were tuned to mimic the pH and ionic composition of the intestinal space (AAA). Likewise, when triplets of the composition BAC were formed, rapid equivalent diffusion out of droplet A into droplets B and C was observed, and in the case of ABB triplets, rapid diffusion into the first B droplet, B<sub>1</sub>, was followed by equilibration between both B droplets. The behavior of ACB triplets closely followed that of ABC triplets. However, when ACC triplets were formed, rapid diffusion into C<sub>1</sub> occurred, and the fluorophore did not continue into the second C droplet, C<sub>2</sub>. In all cases where pH 7.4 droplets were tested with pH 6.5 droplets, fluorescein demonstrated a clear preference for pH 7.4 compartments.

The primary driving force for the selective diffusion path seen in our pharmacokinetic compartment model is the different pH environments encapsulated in droplets A and B, and hence the fluorophore rapidly leaves the intestinal space and enters the enterocyte. Fluorescein has a pK<sub>a</sub> at 6.43,<sup>152</sup> so a larger fraction of molecules exist in the less lipid-soluble dianionic form at pH 7.4 and a larger fraction exist in the more lipid-soluble monoanionic form at pH 6.5. This effectively allows fluorescein to easily diffuse into the artificial cell membrane from the intestinal space, but to diffuse back into the intestinal space from the enterocyte at a far reduced rate. This ties rate of dif-

fusion to lipophilicity in the same way as PAMPA.<sup>10</sup> The fluorescein monoanion and dianion exhibit slight differences in absorption and emission spectra, including in fluorescence intensity and quantum yield,<sup>153,154</sup> which is accounted for using calibration curves as described above and in Figure B.4, Figure B.5, and Figure B.6 in the ESI. The movement of the fluorophore between droplets B and C, which are at the same pH, is explained by the second driving force for the observed transport phenomenon, which is the difference in osmolality between these droplets.

$$Osmolality = 2[Na^+ + K^+] + [urea] + [glucose]^{155} \quad (4.4)$$

Respectively, the calculated osmolalities of droplets A, B, and C are 320 mM, 280 mM, and 320 mM. Diffusion will be driven towards higher osmolality compartments, but because the majority of fluorescein exists as a dianion in droplet B and thus cannot diffuse back into droplet A, the equilibrium lies further towards droplet C.

## 4.5 Conclusions

Here we show a new type of pharmacokinetic compartment model with higher correlation to cell-based assays than PAMPA, the current state-of-the-art technology. This suggests that a higher degree of *in vitro-in vivo* correlation may also be found using our bespoke pharmacokinetic compartment model. We intend our method to be complementary to cell-based assays by providing a way of creating bespoke artificial

cell membranes and pharmacokinetic compartments to quantify the effect that each component has on drug transport.

We have used a new type of microfluidic platform for the formation of DIBs in parallel to build a pharmacokinetic compartment model of the path that an orally administered drug takes from the intestinal space, into enterocytes, and finally into the blood. We demonstrate how this compartment model can predict pharmacokinetic properties of a drug including half-life, flux and  $P_{app}$ . Our pharmacokinetic compartment model demonstrates a greater degree of similarity of  $P_{app}$  to a true biological system (rat jejenum) than is possible with PAMPA.

Our microfluidic platform is simple to use (it only requires a fast response pressure pump) and allows bespoke artificial cells to be formed of sizes ( $\sim 0.5$  nL) that more closely mimic human cells than preceding work using the major phospholipid components (PE and PC) of intestinal cells. We demonstrate and quantify the reproducibility of this platform and show the collection of data with far better time resolution than previously possible. Ongoing and future developments include modeling drug transport in other human tissues and investigating new drug tagging and detection methods.

The limited correlation between *in vitro* and *in vivo* methods for the prediction of drug behaviour in humans is a severe constraint in the timely and cost-effective development of new drugs. Our new *in vitro* model could allow the early prediction of pharmacokinetic parameters of drug candidates by enabling researchers in academia and the pharmaceutical industry to build bespoke pharmacokinetic compartment models.

## **4.6 Conflicts of interest**

There are no conflicts to declare.

## **4.7 Acknowledgements**

This research was funded through the Natural Sciences and Engineering Research Council of Canada (NSERC) Discovery Grant program. Dr. Elvira's position is funded through the Canada Research Chair program and her laboratory was equipped using funding from the Canada Foundation for Innovation John R. Evans Leaders Fund (CFI-JELF), the British Columbia Knowledge Development Fund (BCKDF) and the NSERC Research Tools and Instruments program. We also acknowledge Alberto Escobar Mingo for building the heating platform used in this work, and for writing the Electronic Supplementary Information section detailing its performance.



## Chapter 5

# Biomimetic artificial cells to model the effect of membrane asymmetry on chemoresistance

The work presented in this chapter builds upon the concept of using DIBs for pharmacokinetics assays initially presented in Chapter 4, and applies it to examining membrane asymmetry and its effects on membrane permeability. Presented herein is the published form of this work in which I was the first author, which was published in Chemical Communications under the title: *Biomimetic artificial cells to model the effect of membrane asymmetry on chemoresistance*.<sup>13</sup> This work included electronic supplementary information, which is shown in Appendix C. In this work, I developed a new version of the microfluidic platform shown in Chapter 2 to construct asymmet-

ric DIBs lipid-out using a naturally derived lipid mixture. The lipid-out method is difficult, if not impossible to do without microfluidic methods, and it had never before been done for any type of phospholipid, biomimetic or not. As the lipid-out method enabled straightforward collection and interpretation of permeability data, I used my platform to study the effect of membrane asymmetry on absorption of the chemotherapy drug doxorubicin (DOX). Ultimately, I determined that membrane asymmetry effected the permeability of a DIB to DOX, which served show a possible mechanism of chemoresistance in cancers. With this, I demonstrate that DIBs on a microfluidic device not only can carry out assays currently in existence with higher *in vitro-in vivo* correlation as seen in Chapter 4, but that DIBs enable entirely new methods to examine drug absorption *in vitro*, potentially providing previously hard to obtain insight into pharmacokinetics.

## 5.1 Abstract

We present a microfluidic platform that enables the formation of bespoke asymmetric droplet interface bilayers (DIBs) as artificial cell models from naturally-derived lipids. We use them to perform pharmacokinetic assays to quantify how lipid asymmetry affects the permeability of the chemotherapy drug doxorubicin. Previous attempts to model bilayer asymmetry with DIBs have relied on the use of synthetic lipids to achieve asymmetry. Use of natural lipids serves to increase the biomimetic nature of these artificial cells, showcasing the next step towards forming a true artificial

cell membrane *in vitro*. Here we use our microfluidic platform to form biomimetic, asymmetric and symmetric DIBs, with their asymmetry quantified through their life-mimicking degree of curvature. We subsequently examine permeability of these membranes to doxorubicin, and reveal measurable differences in its pharmacokinetics induced by membrane asymmetry, highlighting another factor that potentially contributes to chemoresistance in some forms of cancer.

## 5.2 Introduction

The lipid membrane of living cells contains several anatomical features which model membranes should replicate in order to be described as biomimetic. One of these is that the distribution of phospholipids is different between the inner and outer leaflets of eukaryotic cell bilayers. This asymmetry is maintained by proteins referred to as flippases and floppases.<sup>16</sup> Morphological changes to lipid membranes due to their asymmetry affect the pharmacokinetics of drug compounds, but current model membranes are not well-suited to modelling membrane asymmetry. Furthermore, loss of bilayer asymmetry is a feature of some types of cancerous cells, with important implications for detection of cancers and their course of treatment.<sup>156,157</sup> The anthracycline class of chemotherapy drugs, including doxorubicin (DOX), are particularly sensitive to these changes in lipid composition.<sup>158</sup> However, it is not possible to model membrane asymmetry using parallel artificial membrane permeation assays (PAMPA)<sup>10</sup> and incorporation of asymmetry in liposomes is more difficult than their symmet-

ric counterparts. Notable techniques for formation of asymmetric liposomes include treating symmetric liposomes with transfer proteins or cyclodextrins,<sup>159,160</sup> manipulation of water-in-oil emulsions,<sup>161</sup> and microfluidic methods,<sup>162</sup> each with their own challenges and caveats.<sup>36</sup> Additionally, computational models have shown that the effect of membrane asymmetry on permeability is highly dependent on curvature.<sup>33</sup> Since liposomes are generally significantly smaller than cells,<sup>163</sup> their correspondingly higher degree of curvature for very small liposomes may provide misleading results. We and others have recently shown that Droplet Interface Bilayers (DIBs) are biomimetic, cell-sized artificial cell models,<sup>43,55</sup> but these models can be developed further to more closely replicate cellular features.

Here we demonstrate for the first time the formation of asymmetric DIB-based artificial cells using bespoke, biomimetic, mammalian lipid formulations, and show how loss of asymmetry affects permeability of DOX. Lipids extracted from natural sources consist of numerous different fatty acid chain lengths and degrees of unsaturation, altering their physical properties and membrane packing characteristics. To date, all asymmetric DIBs have relied on synthetic phospholipids for one or both leaflets and none mimic the asymmetry found in mammalian cells.<sup>39,40,43,45,164,165</sup> The lipid formulations we use consist of naturally-derived 1- $\alpha$ -phosphatidylcholine (PC), 1- $\alpha$ -phosphatidylethanolamine (PE), sphingomyelin (SM) and cholesterol (CHOL). See Figure C.1 in the ESI for chemical structures. We chose to focus on these components of the cell membrane based on prior lipidomics data that quantifies membrane asymmetry.<sup>166</sup> PC and PE are the largest constituents of cell membranes, and are known to display an asymmetric distribution between leaflets, and SM and CHOL are known

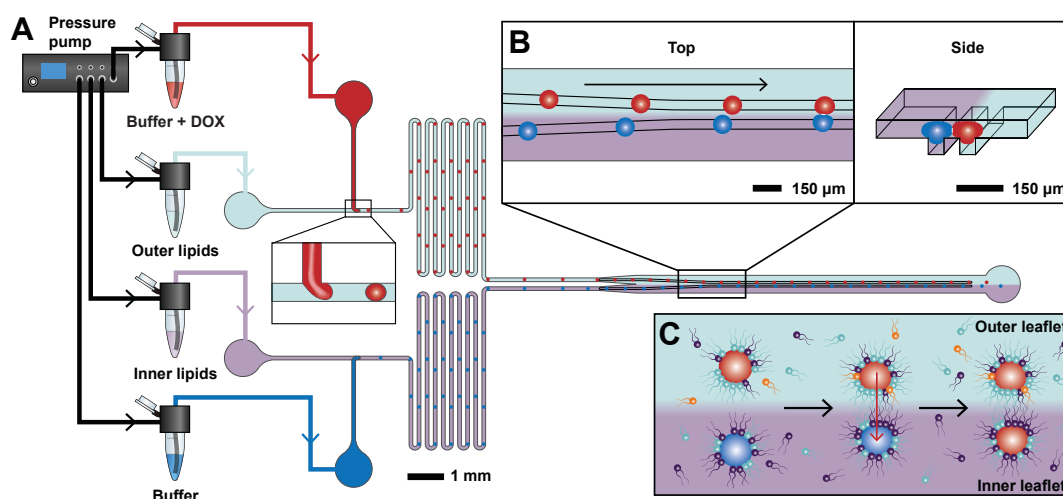


Figure 5.1: **A)** Design of the microfluidic platform showing how the device is connected to the pump and which solution is pumped into each inlet. Aqueous (buffer with DOX, red, or buffer, blue) solutions for the droplets and the surrounding oil phases (different lipid formulations in squalene, light blue and purple) meet at two T-junctions, allowing the formation of two different types of droplets surrounded by different lipid monolayers (inset shows red DOX-containing droplet formation). The meanders allow monolayer formation and equilibration before the droplets enter the main chamber. Arrows show direction of fluid flow. The design of the microfluidic device is shown to scale. **B)** Parallel rails are etched into the main chamber of the microfluidic device, bringing the droplets into contact with each other to form DIBs. **C)** Diagram showing the DIB formation process, the localisation of the lipids (not to scale), and subsequent DOX diffusion assays. A DOX-containing aqueous buffer droplet (red) is formed in an oil phase (light blue) containing the lipid formulation that represents the outer leaflet. The interior of this droplet represents the extracellular environment. An aqueous buffer droplet (blue) is formed in an oil phase (purple) containing the lipid formulation that represents the inner leaflet. The interior of this droplet represents the interior of the cell. The lipids in the oil phases form a monolayer at the surface of the droplets. The microfluidic device enables the droplets to be brought into contact with each other to form a DIB. DOX then diffuses from the donor droplet to the acceptor droplet (indicated by a red arrow), and the rate of this diffusion is quantified for permeability assays.

to coalesce strongly in major structural regions of the cell membrane known as lipid rafts.<sup>167</sup> SM is also nearly exclusively found on the outer leaflet.<sup>166</sup>

## 5.3 Experimental

We have developed a microfluidic platform that enables the formation of cell-sized asymmetric DIBs using natural lipids dosed in the oil phase (Figure 5.1). When forming DIBs, droplets of water are generated in a surrounding oil phase, with phospholipids suspended in either phase. The phospholipids self-assemble at the interface between these two phases in a monolayer, and when the droplets are brought into contact with each other, the monolayers will zip together to form a bilayer (DIB). Our microfluidic device is designed to form two different types of monolayer-covered droplets with a different bespoke lipid formulation dosed in each of the oil phases (Figure 5.1A). Full monolayer formation is enabled by adding meanders, before gently bringing the droplets together in the main chamber using rails to form DIBs between the droplets (Figure 5.1B). Following DIB formation, permeability assays are carried out by observing the diffusion of DOX from the DOX-containing donor droplet to the empty acceptor droplet (Figure 5.1C). We demonstrate the formation of stable asymmetric biomimetic DIBs through quantification of bilayer curvature. For asymmetric DIBs, the outer and inner leaflet compositions are shown in Table C.1 in the ESI. To quantify the effect that asymmetry has on DOX permeability, symmetric DIBs were also formed, where a 50:50 mix of the asymmetric lipid formulations were used for

both droplets. Partially symmetric DIBs (called “blend”) were also formed using a 75:25 mix of the asymmetric lipid formulations for the outer leaflet and a 25:75 mix of the asymmetric lipid formulations for the inner leaflet. Symmetric and blend formulations were prepared immediately before use by combining the required amount of asymmetric inner and outer leaflet solutions. Exact formulations for symmetric and blend DIBs are also shown in Table C.1 in the ESI.

Polydimethylsiloxane (PDMS) microfluidic devices, the aqueous buffer for droplet formation and lipid solutions in squalene (the oil phase for droplet formation) were prepared as described previously,<sup>55</sup> see ESI section C.1 for additional details. Lipid solutions in squalene and aqueous solutions (buffer or buffer with 1 mM DOX) were pumped into the microfluidic device using an Elveflow OB1 mk3 pressure pump at an operating pressure range of 115-145 mbar. Solutions were loaded into Eppendorf tubes and connected to the microfluidic device using matched lengths of 250  $\mu$ m inner diameter polytetrafluoroethylene (PTFE) tubing (Figure 5.1A), and the whole assembly was placed on a custom heating platform<sup>55</sup> on a Nikon Eclipse Ti2-E inverted microscope for visualisation. Experiments were carried out at 50 °C, the lowest temperature that allows DIB formation with these naturally derived lipid formulations. Device flow was stopped when a DIB formed, and collection of brightfield and fluorescence images was carried out immediately using a Hamamatsu ORCA-Flash4.0 V3 camera and a Solis-1C white LED light source (Thor Labs). Fluorescence images were collected using an mCherry-C filter cube set (Semrock) with excitation and emission bands of 538-588 nm and 600-685 nm respectively. Images were collected every 5 s for 1 min and then every 20 s for 10 min. These images were collected and

then analyzed with NIS Elements Advanced Research (Nikon, 5.11.01). All curvature measurements were carried out at time of 4 min to allow for complete bilayer formation. To normalise droplet curvature measurements with respect to droplet size, the radius of a circle fitted to the inner leaflet droplet on the face opposite the bilayer was measured. Relative curvature was then calculated by dividing droplet radius by the radius of a circle fitted to the bilayer itself. Additional details on these measurements, as well as measurement of fluorescence intensity, droplet size and bilayer size may be found in Figure C.2, Figure C.3, and Figure C.4 in the ESI.

## 5.4 Results and discussion

Our microfluidic platform allows the formation of asymmetric DIBs using naturally derived lipids dosed in the oil phase (“lipid-out”). Lipid asymmetry is maintained over at least 10 min (see Figure C.5, Figure C.6, and Figure C.7 in the ESI), allowing quantification of the effect that asymmetry has on DOX permeability. Using DIBs formed lipid-in (lipids dosed in the aqueous phase) for pharmacokinetic modelling is difficult, as liposomes present in solution may retain drug and complicate interpretation of drug diffusion. In contrast to most prior work,<sup>39,40,45,164</sup> our device uses the lipid-out approach to enable collection of diffusion data. There are two main reasons why our device enables the stable formation of asymmetric model membranes. Firstly, squalene is around 13 times more viscous than water,<sup>168,169</sup> which means that mixing of the two different lipid formulations present in each of the two oil phases is very slow.



Secondly, monolayer formation when forming DIBs lipid-out is generally slower than when forming them lipid-in, in large part due to the higher energy barrier to inverse micelle contact with the fluid interface of a partially formed monolayer.<sup>54</sup> This suggests that there is also a large energetic barrier to lipid exchange in the oil solutions, leading to a preservation of asymmetry following DIB formation.

Here we show that DIBs can model the curvature of real cells and that this depends on the lipids used. We found that the asymmetric distribution of lipids between leaflets was quantifiable using membrane curvature, and that increased bilayer asymmetry leads to an enhanced degree of curvature (Figure 5.2). Previous work has shown that asymmetric DIBs made from synthetic phospholipids display curvature based on differing interfacial tension (IFT) of the leaflets.<sup>165</sup> Our natural lipid formulations show an enhanced degree of curvature, more closely replicating the morphology of cellular membranes. The scale of our droplets is similar to that of human cells,<sup>140</sup> and the DIB curvature relative to droplet size approaches 1:1 for the asymmetric bilayers. Hence, the curvature observed in our asymmetric DIBs mimics the expected curvature for an actual cell, driven by a 20-fold difference in IFT between the leaflets (see Table C.2 in the ESI). This driving force likely differs from those observed in biological membranes, which have considerably lower IFT.<sup>170</sup> Early preliminary experiments showed that the curvature exhibited by membranes consisting of identical concentrations of DOPC, PE and CHOL did not display this dramatic curvature (see Figure C.8 in the ESI). This suggests that SM contributes the greatest amount to the differing interfacial tension between leaflets. Indeed, this 20-fold drop in IFT was observed with addition of only 120  $\mu\text{M}$  of SM (see Figure C.9 in the ESI). The differing

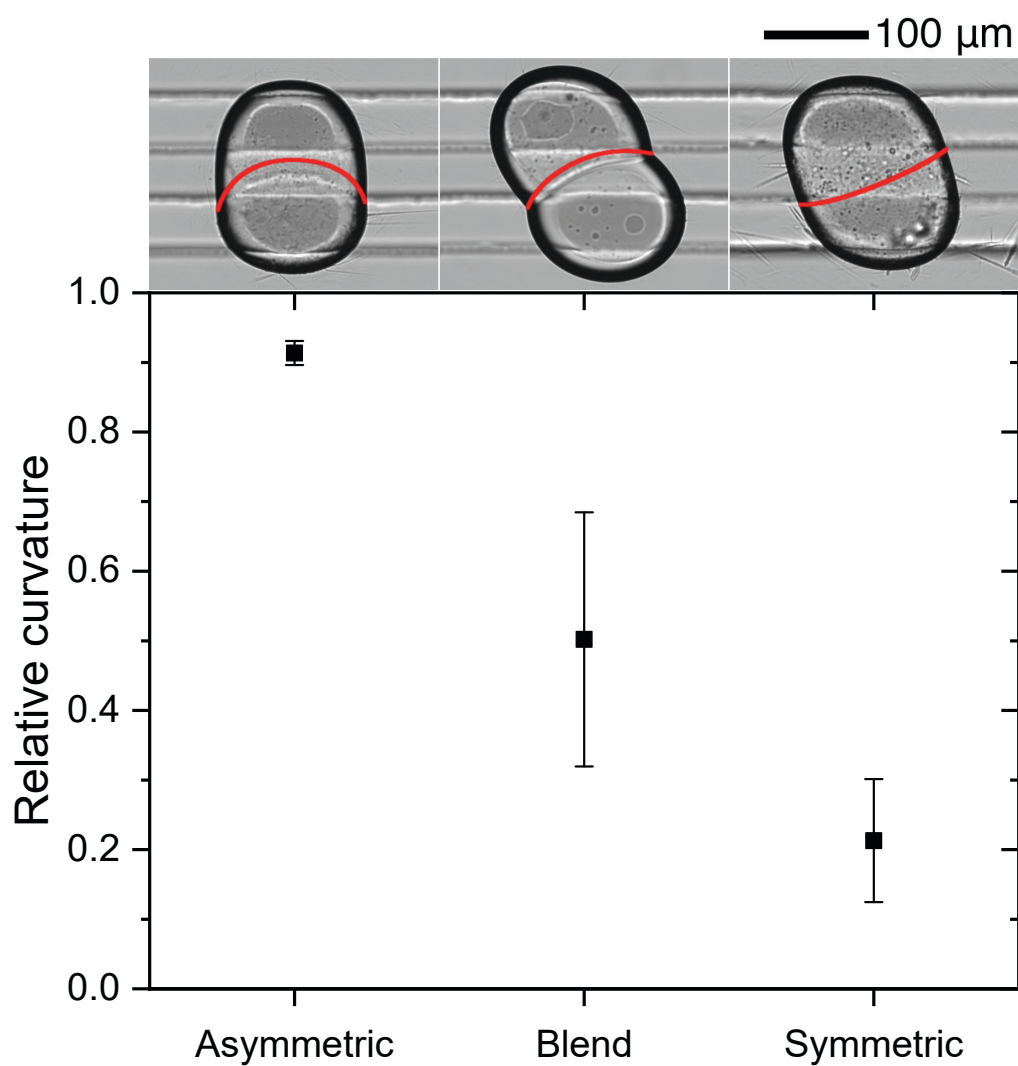
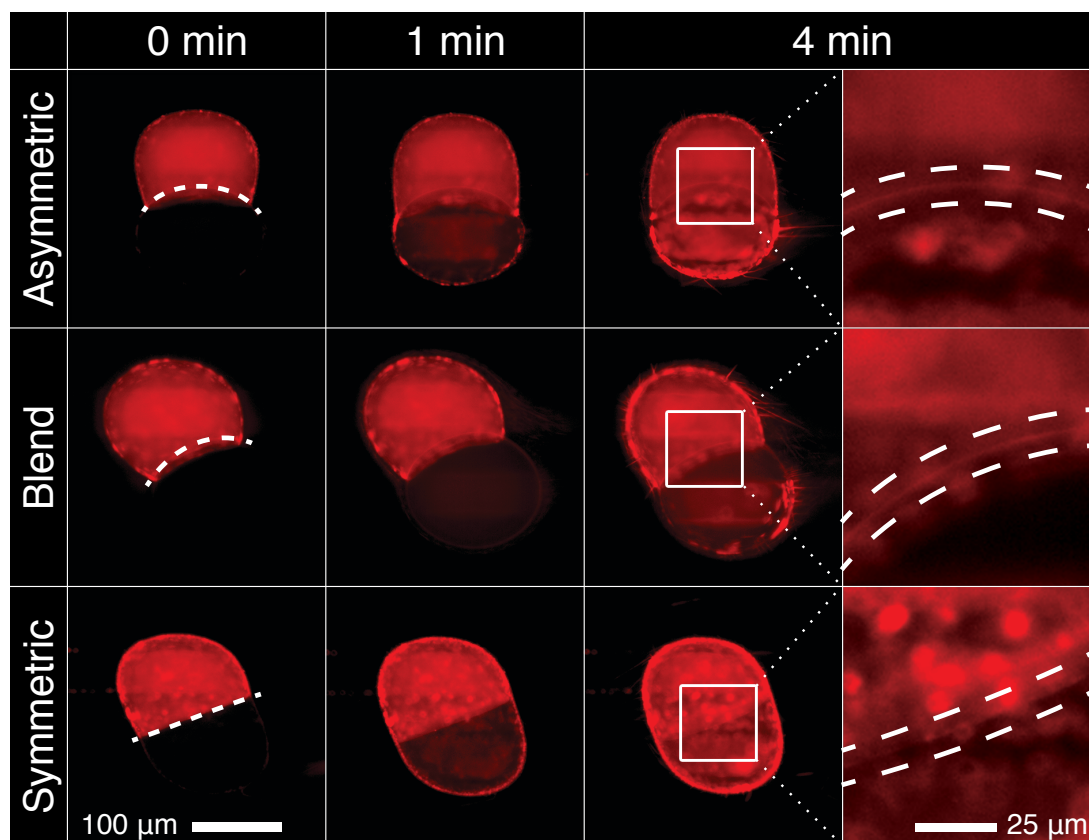


Figure 5.2: **Relative curvature of asymmetric, blend, and symmetric DIBs.** Data are normalised for droplet size. Error bars represent the standard deviation ( $n = 3$ ). Representative images for each formulation are shown above their respective data points, with the measured portion of the bilayer indicated by a red line. The scale applies to all images. The non-spheroidal shape seen in both symmetric bilayer droplets is likely due to the exceptionally low IFT in these bilayers, which also makes them less stable over time.

curvature conferred by the cylindrical and conical shape of PC and PE respectively appears to be a secondary effect, in agreement with membrane curvature preferences found in the literature.<sup>171</sup>



**Figure 5.3: Diffusion of DOX across asymmetric, blend and symmetric bilayers is shown over time.** The initial bilayer location is indicated by a dashed white line for each lipid formulation. The evolution of the bilayer as it forms can be seen, with equilibrium bilayer size and curvature visible at time = 4 min. The scale applies to all images in the first three columns. DOX localisation in membrane domains is shown for the last set of images, as indicated by the white squares at time = 4 min. The interaction between DOX and the bilayer is visible in the final column of images as a thin bright line (highlighted with dashed lines). This column has been contrast enhanced to aid visualisation. The scale applies to all expanded images. For original images, see Figure C.10, Figure C.11, Figure C.12, and Figure C.13 in the ESI.

Our microfluidic platform enables us to create DIBs from bespoke lipid formulations which we can use to distinguish the effect that lipid asymmetry has on DOX permeation. We quantified DIB permeability to DOX with asymmetric, symmetric, and blend lipid formulations. We found differences in the permeability of our biomimetic model membranes to DOX depending upon their asymmetry, and quantified this using fluorescence intensity (Figure 5.3). The fluorescence intensity of DOX upon association with phospholipid bilayers is known to be enhanced.<sup>172</sup> This increased intensity of DOX fluorescence is visible in the DIBs as a thin brighter line between the droplets (Figure 5.3). This further shows the biomimetic nature of our DIBs since they correctly model the local microenvironment of a cellular membrane, with the visible enhancement of DOX fluorescence serving as evidence of the expected interaction between DOX and the bilayer. We quantified DOX permeation using flux (Figure 5.4), which revealed an inverse relationship between membrane symmetry and permeability. The cause of this relationship is unclear, but we believe differing IFT and lipid packing are more likely to drive this relationship than the differing curvatures, given that the curved bilayers are effectively planar on the molecular scale. The permeability ( $P_{app}$ ) for the asymmetric, blend and the symmetric bilayers is  $5.3 \pm 0.2 \times 10^{-6} \text{ cm s}^{-1}$ ,  $5 \pm 1 \times 10^{-6} \text{ cm s}^{-1}$  and  $4.1 \pm 0.3 \times 10^{-6} \text{ cm s}^{-1}$  respectively.  $P_{app}$  for DOX in cells can range from  $0.3 \times 10^{-6} \text{ cm s}^{-1}$  to  $14 \times 10^{-6} \text{ cm s}^{-1}$  depending on cell line and DOX concentration.<sup>173</sup> Our  $P_{app}$  therefore is in agreement with data obtained by other *in vitro* methods, although being collected above physiological temperature likely increases measured  $P_{app}$ .

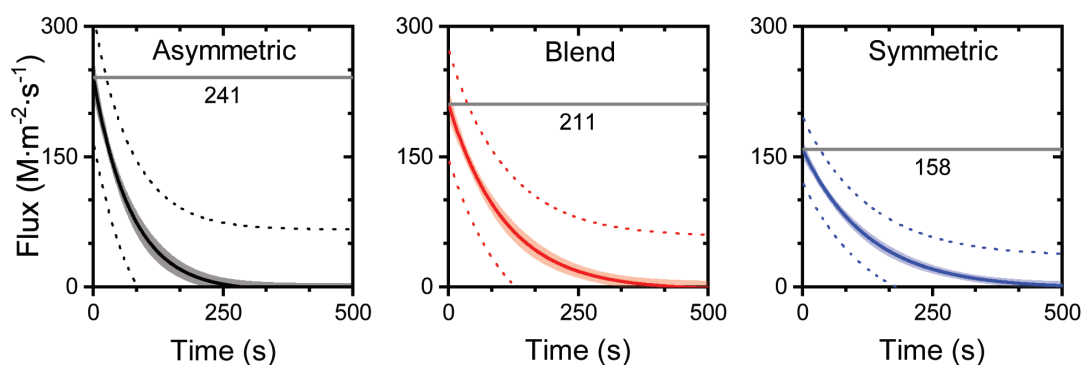


Figure 5.4: **Flux of DOX over time for asymmetric, blend and symmetric DIBs.** Graphs show the trendlines for flux calculated from fluorescence intensity measurements (see ESI section C.5 for formulae) with 95% confidence bands (shaded) and 95% prediction bands (dotted lines) ( $n = 3$ ). Peak flux is indicated by a horizontal line, with this value used for  $P_{app}$  calculations.

## 5.5 Conclusions

In conclusion, our microfluidic platform enables us to build asymmetric bilayers using naturally derived lipids that mimic mammalian cells and use them to quantify the effect that lipid asymmetry has on permeability of DOX. Our membrane curvature characterisation revealed that an asymmetric lipid formulation based on the leaflet composition of real cells produces a degree of curvature comparable to that of a biological system. We have hence shown that we are significantly closer to making artificial membranes that are worthy of the title of artificial cell, since they truly emulate cell membranes found in nature. By studying the permeability of both symmetric and asymmetric bilayers to DOX, we have found that bilayer asymmetry has a measurable effect on permeability of a membrane to a chemotherapy drug. This not only shines light on one potential mechanism by which tumors may exhibit chemoresistance, but

also serves to highlight the importance of fully replicating the structural features of biological systems when studying their pharmacokinetics *in vitro*. The newly demonstrated ability of our biomimetic, asymmetric, DIB-based artificial cells to measure permeability of chemotherapy drugs *in vitro* opens the door to an entirely new kind of pharmacokinetic study for drugs both during and following their development. For acknowledgements and funding sources, see ESI section C.6.

## **5.6 Conflicts of interest**

There are no conflicts to declare.

## Chapter 6

### Conclusions and future work

Through my research, I sought to establish the potential for DIBs on microfluidic devices to serve as a platform for studying pharmacokinetics *in vitro*, as well as answer fundamental questions pertinent to how phospholipids behave on these devices.

By developing a new microfluidic platform for forming DIBs as seen in Chapter 2, I addressed the shortcomings found in many microfluidic methods of forming DIBs: low throughput, low reproducibility when building networks from more than one type of droplet, complexity in manufacturing and operation, and fast droplet contact leading to coalescence of droplets with more complex lipid mixtures. The platform that I developed is robust, reproducible, easy to manufacture and use, brings droplets into contact gently, and can form DIBs faster than most microfluidic methods. The platform was robust enough to serve as the platform for the work presented in Chapters 4<sup>55</sup> and 5,<sup>13</sup> as well as being adaptable for use by other members of our research

group.

My currently ongoing study of the behaviour of DPhPC on PDMS based microfluidic devices seen in Chapter 3 has provided valuable insight into this previously unstudied area. I have been able to conclude that DPhPC does not assemble in a monolayer fast enough to effect interfacial tension during droplet formation, providing guidance on how to design microfluidic devices for DIB formation by designing for a system for no lipids. Furthermore, I have found that DPhPC leads to enhanced wetting of water to the walls of a PDMS based microfluidic device, suggesting that more widespread adoption of microfluidic methods for DIB formation will require use of different materials than the ubiquitous PDMS, or the development of new surface treatment protocols.

By using the platform that I developed for a pharmacokinetic compartment model as shown in Chapter 4, my collaborator Jaime Korner and I demonstrated that DIBs made from naturally derived lipids can be used to determine pharmacokinetic parameters *in vitro* such as apparent permeability ( $P_{app}$ ), which we did using the fluorescent tracer fluorescein. Not only were we able to show that DIBs could be used for carrying out pharmacokinetic assays, but that they were able to measure  $P_{app}$  with greater accuracy than currently used macroscopic methods such as PAMPA.

Finally, in Chapter 5, I demonstrated that DIBs could be used to reproduce structural features found in biological cells such as membrane asymmetry, and could be used to study their effect on drug absorption. I constructed biomimetic asymmetric DIBs using entirely naturally derived mixtures of lipids for the first time using a



modified form of my microfluidic platform. To further demonstrate that microfluidic methods were a critical facet of my work, I formed these DIBs lipid-out, which would be impossible using traditional macroscopic DIB formation techniques. By examining the absorption of the chemotherapy drug doxorubicin across asymmetric DIBs, I determined that membrane asymmetry had a measurable effect on its permeation, and may contribute to the reduced absorption of doxorubicin seen in some forms of cancer. Acquiring this information through other pharmacokinetic assays like PAMPA, PVPA, and a Caco-2 permeability assay is not possible, and shows that DIBs on microfluidic devices can be used to provide new insights into pharmacokinetics during the process of drug development.

In addition to the future work required to conclude Chapter 3, there are multiple future avenues to meaningfully build upon this research. In order to ameliorate the lipid induced surface property deterioration uncovered in Chapter 3, and allow more widespread adoption of these microfluidic methods, exploration of new surface treatments for PDMS devices is needed. Numerous ways to change the surface properties of PDMS exist in the literature,<sup>75</sup> but their longevity can be short, and their ability to change the behaviour of lipid containing solutions on microfluidic devices is almost entirely unknown. A logical, albeit ambitious progression to the work in Chapters 4 and 5 is to incorporate a human transporter protein for study of active transport of drugs. Until now, only a prokaryotic transporter has ever been successfully studied in a DIB.<sup>42</sup> Successfully incorporating a human transporter would demonstrate that the methods presented here can be generalised towards studying more than just passive diffusion, further advancing DIBs towards supplanting cell based pharmacokinetics

assays. Finally, one great hurdle towards more widespread adoption of DIB based microfluidic methods is their overreliance on fluorescence, microscopy and electrical measurements for quantification. Modifying the device that I developed in Chapter 2 to allow unloading of droplets after each experiment could potentially enable use of highly sensitive, broadly applicable methods like mass spectrometry. This would enable use of my microfluidic methods to study pharmacokinetics of a far greater number of compounds than currently possible.

In conclusion, I have found through the course of my research that DIBs formed on microfluidic devices show great potential as a platform for pharmacokinetics assays. DIB based on-chip pharmacokinetic assays may enable new studies previously inaccessible in a drug development setting, such as an assay assessing membrane asymmetry and its effect on drug permeation. Through the application of these bespoke artificial cells, I believe that microfluidic methods and DIBs may someday reduce the astronomical costs associated with drug development, accelerate the drug development process, and serve as valuable tools in the pursuit of new scientific knowledge.

# References

- [1] DiMasi, J. A., Grabowski, H. G. & Hansen, R. W. Innovation in the pharmaceutical industry: New estimates of R&D costs. *Journal of Health Economics* **47**, 20–33 (2016). URL <http://www.sciencedirect.com/science/article/pii/S0167629616000291>.
- [2] DiMasi, J. A., Hansen, R. W. & Grabowski, H. G. The price of innovation: new estimates of drug development costs. *Journal of Health Economics* **22**, 151–185 (2003). URL <https://www.sciencedirect.com/science/article/pii/S0167629602001261>.
- [3] Commissioner, O. o. t. The Drug Development Process (2020). URL <https://www.fda.gov/patients/learn-about-drug-and-device-approvals/drug-development-process>. Publisher: FDA.
- [4] Ritter, J., Flower, R., Henderson, G., Loke, Y. K. & MacEwan, D. *Rang and Dale's Pharmacology* (Elsevier, 2018), 9th edn.

- [5] Alavijeh, M. S. & Palmer, A. M. The pivotal role of drug metabolism and pharmacokinetics in the discovery and development of new medicines. *IDrugs: The Investigational Drugs Journal* **7**, 755–763 (2004).
- [6] Giacomini, K. M. *et al.* Membrane transporters in drug development. *Nature Reviews Drug Discovery* **9**, 215–236 (2010). URL <https://doi.org/10.1038/nrd3028>.
- [7] Lu, C. & Di, L. In vitro and in vivo methods to assess pharmacokinetic drug–drug interactions in drug discovery and development. *Biopharmaceutics & Drug Disposition* **41**, 3–31 (2020). URL <https://onlinelibrary.wiley.com/doi/abs/10.1002/bdd.2212>.
- [8] Brouwer, K. L. R. *et al.* In Vitro Methods to Support Transporter Evaluation in Drug Discovery and Development. *Clinical Pharmacology & Therapeutics* **94**, 95–112 (2013). URL <http://onlinelibrary.wiley.com.ezproxy.library.uvic.ca/doi/10.1038/clpt.2013.81/abstract>.
- [9] Berben, P. *et al.* Drug permeability profiling using cell-free permeation tools: Overview and applications. *European Journal of Pharmaceutical Sciences* **119**, 219–233 (2018). URL <https://www.sciencedirect.com/science/article/pii/S0928098718301751>.
- [10] Kansy, M., Senner, F. & Gubernator, K. Physicochemical high throughput screening: Parallel artificial membrane permeation assay in the description of

- passive absorption processes. *Journal of Medicinal Chemistry* **41**, 1007–1010 (1998). URL <https://pubs.acs.org/doi/10.1021/jm970530e>.
- [11] Flaten, G. E., Dhanikula, A. B., Luthman, K. & Brandl, M. Drug permeability across a phospholipid vesicle based barrier: a novel approach for studying passive diffusion. *European Journal of Pharmaceutical Sciences: Official Journal of the European Federation for Pharmaceutical Sciences* **27**, 80–90 (2006).
- [12] Hidalgo, I. J., Raub, T. J. & Borchardt, R. T. Characterization of the human colon carcinoma cell line (Caco-2) as a model system for intestinal epithelial permeability. *Gastroenterology* **96**, 736–749 (1989). URL <http://www.sciencedirect.com/science/article/pii/0016508589908974>.
- [13] Stephenson, E. B. & Elvira, K. S. Biomimetic artificial cells to model the effect of membrane asymmetry on chemoresistance. *Chemical Communications* **57**, 6534–6537 (2021). URL <https://pubs.rsc.org/en/content/articlelanding/2021/cc/dlcc02043a>.
- [14] Balimane, P. V., Chong, S. & Morrison, R. A. Current methodologies used for evaluation of intestinal permeability and absorption. *Journal of Pharmacological and Toxicological Methods* **44**, 301–312 (2000). URL <https://www.sciencedirect.com/science/article/pii/S1056871900001131>.
- [15] Singer, S. J. & Nicolson, G. L. The Fluid Mosaic Model of the Structure of

- Cell Membranes. *Science* **175**, 720–731 (1972). URL <https://science.sciencemag.org/content/175/4023/720>.
- [16] Hankins, H. M., Baldrige, R. D., Xu, P. & Graham, T. R. Role of flippases, scramblases, and transfer proteins in phosphatidylserine subcellular distribution. *Traffic* **16**, 35–47 (2015). URL <https://www.ncbi.nlm.nih.gov/pmc/articles/PMC4275391/>.
- [17] Mueller, P., Rudin, D. O., Tien, H. T. & Wescott, W. C. Reconstitution of Cell Membrane Structure in vitro and its Transformation into an Excitable System. *Nature* **194**, 979–980 (1962). URL <https://www.nature.com/articles/194979a0>.
- [18] Bangham, A. D. & Horne, R. W. Negative staining of phospholipids and their structural modification by surface-active agents as observed in the electron microscope. *Journal of Molecular Biology* **8**, 660–IN10 (1964). URL <https://www.sciencedirect.com/science/article/pii/S0022283664801157>.
- [19] Fettiplace, R. *et al.* Techniques in the Formation and Examination of “Black” Lipid Bilayer Membranes. In Korn, E. D. (ed.) *Biophysical Approaches*, 1–75 (Springer US, Boston, MA, 1975). URL [https://doi.org/10.1007/978-1-4684-2907-7\\_1](https://doi.org/10.1007/978-1-4684-2907-7_1).
- [20] Kongsuphol, P., Fang, K. B. & Ding, Z. Lipid bilayer technologies in ion channel recordings and their potential in drug screening assay. *Sensors and Actuators B: Chemical* **185**, 530–542 (2013). URL

- <https://www.sciencedirect.com/science/article/pii/S0925400513005601>.
- [21] Akbarzadeh, A. *et al.* Liposome: classification, preparation, and applications. *Nanoscale Research Letters* **8**, 102 (2013). URL <https://dx.doi.org/10.1186%2F1556-276X-8-102>.
- [22] Kondo, T., Dale, G. L. & Beutler, E. Glutathione transport by inside-out vesicles from human erythrocytes. *Proceedings of the National Academy of Sciences* **77**, 6359–6362 (1980). URL <https://www.pnas.org/content/77/11/6359>.
- [23] Let's talk about lipid nanoparticles. *Nature Reviews Materials* **6**, 99–99 (2021). URL <https://www.nature.com/articles/s41578-021-00281-4>.
- [24] Barenholz, Y. C. Doxil® — The first FDA-approved nano-drug: Lessons learned. *Journal of Controlled Release* **160**, 117–134 (2012). URL <https://www.sciencedirect.com/science/article/pii/S0168365912002301>.
- [25] Corbett, K. S. *et al.* SARS-CoV-2 mRNA vaccine design enabled by prototype pathogen preparedness. *Nature* **586**, 567–571 (2020). URL <https://www.nature.com/articles/s41586-020-2622-0>.
- [26] Walsh, E. E. *et al.* Safety and Immunogenicity of Two RNA-Based Covid-

- 19 Vaccine Candidates. *New England Journal of Medicine* **383**, 2439–2450 (2020). URL <https://doi.org/10.1056/NEJMoa2027906>.
- [27] Welty, J., Rorrer, G. & Foster, D. *Fundamentals of Momentum, Heat, and Mass Transfer* (Wiley, 2014), 6 edn. URL <https://books.google.ca/books?id=PVCfDwAAQBAJ>.
- [28] Palumbo, P. *et al.* A general approach to the apparent permeability index. *Journal of Pharmacokinetics and Pharmacodynamics* **35**, 235 (2008). URL <https://doi.org/10.1007/s10928-008-9086-4>.
- [29] White, S. H. The Physical Nature of Planar Bilayer Membranes. In Miller, C. (ed.) *Ion Channel Reconstitution*, 3–35 (Springer US, Boston, MA, 1986). URL [https://doi.org/10.1007/978-1-4757-1361-9\\_1](https://doi.org/10.1007/978-1-4757-1361-9_1).
- [30] Bayley, H. *et al.* Droplet interface bilayers. *Molecular BioSystems* **4**, 1191–1208 (2008). URL <https://doi.org/10.1039/b808893d>.
- [31] Lipinski, C. A., Lombardo, F., Dominy, B. W. & Feeney, P. J. Experimental and computational approaches to estimate solubility and permeability in drug discovery and development settings. *Advanced Drug Delivery Reviews* **23**, 3–25 (1997). URL <http://www.sciencedirect.com/science/article/pii/S0169409X96004231>.
- [32] Allen, T. M. & Cleland, L. G. Serum-induced leakage of liposome contents. *Biochimica et Biophysica Acta (BBA) - Biomembranes* **597**, 418–



- 426 (1980). URL <https://www.sciencedirect.com/science/article/pii/0005273680901182>.
- [33] Yesylevskyy, S., Rivel, T. & Ramseyer, C. Curvature increases permeability of the plasma membrane for ions, water and the anti-cancer drugs cisplatin and gemcitabine. *Scientific Reports* **9**, 17214 (2019). URL <https://www.nature.com/articles/s41598-019-53952-2>.
- [34] Membranes. URL <https://avantilipids.com/products/equipment/category/membranes>.
- [35] Montal, M. & Mueller, P. Formation of Bimolecular Membranes from Lipid Monolayers and a Study of Their Electrical Properties. *Proceedings of the National Academy of Sciences* **69**, 3561–3566 (1972). URL <https://www.pnas.org/content/69/12/3561>.
- [36] Nguyen, M. H. L., Rickeard, B. W., DiPasquale, M. & Marquardt, D. Asymmetric Model Membranes: Frontiers and Challenges. In Kök, F. N., Arslan Yildiz, A. & Inci, F. (eds.) *Biomimetic Lipid Membranes: Fundamentals, Applications, and Commercialization*, 47–71 (Springer International Publishing, Switzerland, 2019). URL [https://doi.org/10.1007/978-3-030-11596-8\\_3](https://doi.org/10.1007/978-3-030-11596-8_3).
- [37] Funakoshi, K., Suzuki, H. & Takeuchi, S. Lipid bilayer formation by contacting monolayers in a microfluidic device for membrane protein analysis. *Analytical Chemistry* **78**, 8169–8174 (2006). URL <http://dx.doi.org/10.1021/ac0613479>.

- [38] Holden, M. A., Needham, D. & Bayley, H. Functional bionetworks from nanoliter water droplets. *Journal of the American Chemical Society* **129**, 8650–8655 (2007). URL <https://doi.org/10.1021/ja072292a>.
- [39] Hwang, W. L., Chen, M., Cronin, B., Holden, M. A. & Bayley, H. Asymmetric Droplet Interface Bilayers. *Journal of the American Chemical Society* **130**, 5878–5879 (2008). URL <https://doi.org/10.1021/ja802089s>.
- [40] Stanley, C. E. *et al.* A microfluidic approach for high-throughput droplet interface bilayer (DIB) formation. *Chemical Communications* **46**, 1620–1622 (2010). URL <http://pubs.rsc.org/en/content/articlelanding/2010/cc/b924897h>.
- [41] Nisisako, T., Portonovo, S. A. & Schmidt, J. J. Microfluidic passive permeability assay using nanoliter droplet interface lipid bilayers. *Analyst* **138**, 6793–6800 (2013). URL <https://pubs.rsc.org/en/content/articlelanding/2013/an/c3an01314f>.
- [42] Findlay, H. E., Harris, N. J. & Booth, P. J. In vitro synthesis of a Major Facilitator Transporter for specific active transport across Droplet Interface Bilayers. *Scientific Reports* **6**, 1–9 (2016). URL <https://doi.org/10.1038/srep39349>.
- [43] Bachler, S., Ort, M., Krämer, S. D. & Dittrich, P. S. Permeation Studies across Symmetric and Asymmetric Membranes in Microdroplet Arrays. *Analytical Chemistry* **93**, 5137–5144 (2021). URL <https://doi.org/10.1021/acs.analchem.0c04939>.

- [44] Faugeras, V., Duclos, O., Bazile, D. & Thiam, A. R. Membrane determinants for the passive translocation of analytes through droplet interface bilayers. *Soft Matter* **16**, 5970–5980 (2020). URL <https://doi.org/10.1039/D0SM00667J>.
- [45] Barlow, N. E. *et al.* Engineering plant membranes using droplet interface bilayers. *Biomicrofluidics* **11**, 024107 (2017). URL <https://www.ncbi.nlm.nih.gov/pmc/articles/PMC5367087/>.
- [46] Elvira, K. S., i Solvas, X. C., Wootton, R. C. R. & deMello, A. J. The past, present and potential for microfluidic reactor technology in chemical synthesis. *Nature Chemistry* **5**, 905–915 (2013). URL <http://www.nature.com/nchem/journal/v5/n11/full/nchem.1753.html?foxtrotcallback=true>.
- [47] Song, Y., Cheng, D. & Zhao, L. (eds.) *Microfluidics: Fundamentals, Devices, and Applications* (Wiley, 2018).
- [48] Zhao, Z., Wang, W., Xiao, J., Chen, Y. & Cao, Y. Interfacial Engineering of Pickering Emulsion Co-Stabilized by Zein Nanoparticles and Tween 20: Effects of the Particle Size on the Interfacial Concentration of Gallic Acid and the Oxidative Stability. *Nanomaterials* **10**, 1068 (2020). URL <https://www.mdpi.com/2079-4991/10/6/1068>.
- [49] Kreutz, J. E. *et al.* Evolution of Catalysts Directed by Genetic Algorithms in a Plug-Based Microfluidic Device Tested with Oxidation of Methane by Oxy-

- gen. *Journal of the American Chemical Society* **132**, 3128–3132 (2010). URL <https://doi.org/10.1021/ja909853x>.
- [50] Zhu, Y. & Fang, Q. Analytical detection techniques for droplet microfluidics—A review. *Analytica Chimica Acta* **787**, 24–35 (2013). URL <https://doi.org/10.1016/j.aca.2013.04.064>.
- [51] Zhang, Y. & Jiang, H.-R. A review on continuous-flow microfluidic PCR in droplets: Advances, challenges and future. *Analytica Chimica Acta* **914**, 7–16 (2016). URL <https://doi.org/10.1016/j.aca.2016.02.006>.
- [52] Sánchez Barea, J., Lee, J. & Kang, D.-K. Recent Advances in Droplet-based Microfluidic Technologies for Biochemistry and Molecular Biology. *Micromachines* **10**, 412 (2019). URL <https://doi.org/10.3390/mi10060412>.
- [53] Sohrabi, S., Kassir, N. & Moraveji, M. K. Droplet microfluidics: fundamentals and its advanced applications. *RSC Advances* **10**, 27560–27574 (2020). URL <https://pubs.rsc.org/en/content/articlelanding/2020/ra/d0ra04566g>.
- [54] Venkatesan, G. A. *et al.* Adsorption Kinetics Dictate Monolayer Self-Assembly for Both Lipid-In and Lipid-Out Approaches to Droplet Interface Bilayer Formation. *Langmuir* **31**, 12883–12893 (2015). URL <https://doi.org/10.1021/acs.langmuir.5b02293>.
- [55] Korner, J. L., Stephenson, E. B. & Elvira, K. S. A bespoke microfluidic phar-

- macokinetic compartment model for drug absorption using artificial cell membranes. *Lab on a Chip* **20**, 1898–1906 (2020). URL <https://pubs.rsc.org/en/content/articlelanding/2020/lc/d0lc00263a>.
- [56] Courtney, M. *et al.* Droplet Microfluidic System with On-Demand Trapping and Releasing of Droplet for Drug Screening Applications. *Analytical Chemistry* **89**, 910–915 (2017). URL <https://doi.org/10.1021/acs.analchem.6b04039>.
- [57] Niu, X., Gulati, S., Edel, J. B. & deMello, A. J. Pillar-induced droplet merging in microfluidic circuits. *Lab on a Chip* **8**, 1837–1841 (2008). URL <http://pubs.rsc.org/en/content/articlelanding/2008/lc/b813325e>.
- [58] Zhou, H. & Yao, S. A facile on-demand droplet microfluidic system for lab-on-a-chip applications. *Microfluidics and Nanofluidics* **16**, 667–675 (2014). URL <https://doi.org/10.1007/s10404-013-1268-8>.
- [59] Bai, Y. *et al.* A double droplet trap system for studying mass transport across a droplet-droplet interface. *Lab on a Chip* **10**, 1281–1285 (2010). URL <https://doi.org/10.1039/b925133b>.
- [60] Carreras, P., Elani, Y., Law, R., Seddon, J. & Ces, O. A Droplet Trapping Microfluidic Device For The Study of Mass-Transport Across Droplet Interface Bilayers. *18th International Conference on Miniaturized Systems for Chemistry and Life Sciences, MicroTAS 2014* 1620–1622 (2014).

- [61] Nguyen, M.-A., Srijanto, B., Collier, C. P., Retterer, S. T. & Sarles, S. A. Hydrodynamic trapping for rapid assembly and in situ electrical characterization of droplet interface bilayer arrays. *Lab on a Chip* **16**, 3576–3588 (2016). URL <https://pubs.rsc.org/en/content/articlelanding/2016/1c/c61c00810k>.
- [62] Czekalska, M. A. *et al.* A droplet microfluidic system for sequential generation of lipid bilayers and transmembrane electrical recordings. *Lab on a Chip* **15**, 541–548 (2015). URL <https://doi.org/10.1039/C4LC00985A>.
- [63] Czekalska, M. A., Kaminski, T. S., Horka, M., Jakiela, S. & Garstecki, P. An automated microfluidic system for the generation of droplet interface bilayer networks. *Micromachines* **8**, 93 (2017). URL <http://www.mdpi.com/2072-666X/8/3/93>.
- [64] Schlicht, B. & Zagnoni, M. Droplet-interface-bilayer assays in microfluidic passive networks. *Scientific Reports* **5**, 9951 (2015).
- [65] Carreras, P. *et al.* A microfluidic platform for size-dependent generation of droplet interface bilayer networks on rails. *Biomicrofluidics* **9**, 064121 (2015). URL <https://doi.org/10.1063/1.4938731>.
- [66] Creative Commons. Creative Commons — Attribution 4.0 International. URL <https://creativecommons.org/licenses/by/4.0/>.
- [67] Zheng, B., Tice, J. D. & Ismagilov, R. F. Formation of Droplets of Alternating Composition in Microfluidic Channels and Applications to Indexing of Concen-

- trations in Droplet-Based Assays. *Analytical Chemistry* **76**, 4977–4982 (2004). URL <https://doi.org/10.1021/ac0495743>.
- [68] Zagnoni, M. & Cooper, J. M. A microdroplet-based shift register. *Lab on a Chip* **10**, 3069–3073 (2010). URL <http://pubs.rsc.org/en/content/articlelanding/2010/lc/c0lc00219d>.
- [69] Li, X.-B. *et al.* Study on the mechanism of droplet formation in T-junction microchannel. *Chemical Engineering Science* **69**, 340–351 (2012). URL <https://www.sciencedirect.com/science/article/pii/S0009250911007627>.
- [70] Tadros, T. Interface and Surface. In Tadros, T. (ed.) *Encyclopedia of Colloid and Interface Science*, 634–634 (Springer Berlin Heidelberg, Berlin, Heidelberg, 2013). URL [https://doi.org/10.1007/978-3-642-20665-8\\_100086](https://doi.org/10.1007/978-3-642-20665-8_100086).
- [71] Wehking, J. D., Gabany, M., Chew, L. & Kumar, R. Effects of viscosity, interfacial tension, and flow geometry on droplet formation in a microfluidic T-junction. *Microfluidics and Nanofluidics* **16**, 441–453 (2014). URL <https://doi.org/10.1007/s10404-013-1239-0>.
- [72] Li, X., He, L., He, Y., Gu, H. & Liu, M. Numerical study of droplet formation in the ordinary and modified T-junctions. *Physics of Fluids* **31**, 082101 (2019). URL <https://aip-scitation-org.ezproxy.library.uvic.ca/doi/10.1063/1.5107425>.

- [73] Tadros, T. Contact Angle. In Tadros, T. (ed.) *Encyclopedia of Colloid and Interface Science*, 147–147 (Springer Berlin Heidelberg, Berlin, Heidelberg, 2013). URL [https://doi.org/10.1007/978-3-642-20665-8\\_55](https://doi.org/10.1007/978-3-642-20665-8_55).
- [74] Baret, J.-C. Surfactants in droplet-based microfluidics. *Lab on a Chip* **12**, 422–433 (2012). URL <https://pubs.rsc.org/en/content/articlelanding/2012/lc/c1lc20582j>.
- [75] Zhou, J., Khodakov, D. A., Ellis, A. V. & Voelcker, N. H. Surface modification for PDMS-based microfluidic devices. *Electrophoresis* **33**, 89–104 (2012).
- [76] Santos, R. A Review of Advances in Multiphase Computational Fluid Dynamics for Microfluidics. *International journal of microscale and nanoscale thermal and fluid transport phenomena* **2**, 77–102 (2013).
- [77] Adamson, T., Adamson, A. & Gast, A. *Physical Chemistry of Surfaces*. A Wiley-Interscience publication (Wiley, 1997). URL <https://books.google.ca/books?id=rK4PAQAAMAAJ>.
- [78] Wang, X., Riaud, A., Wang, K. & Luo, G. Pressure drop-based determination of dynamic interfacial tension of droplet generation process in T-junction microchannel. *Microfluidics and Nanofluidics* **18**, 503–512 (2015). URL <https://doi.org/10.1007/s10404-014-1449-0>.
- [79] McDonald, J. C. & Whitesides, G. M. Poly(dimethylsiloxane) as a Material for Fabricating Microfluidic Devices. *Accounts of Chemical Research* **35**, 491–499 (2002). URL <https://doi.org/10.1021/ar010110q>.



- [80] Unger, M. A., Chou, H. P., Thorsen, T., Scherer, A. & Quake, S. R. Monolithic microfabricated valves and pumps by multilayer soft lithography. *Science (New York, N.Y.)* **288**, 113–116 (2000).
- [81] Lee, J. N., Park, C. & Whitesides, G. M. Solvent Compatibility of Poly(dimethylsiloxane)-Based Microfluidic Devices. *Analytical Chemistry* **75**, 6544–6554 (2003). URL <https://doi.org/10.1021/ac0346712>.
- [82] Debon, A. P., Wootton, R. C. R. & Elvira, K. S. Droplet confinement and leakage: Causes, underlying effects, and amelioration strategies. *Biomicrofluidics* **9**, 024119 (2015). URL <http://aip.scitation.org/doi/10.1063/1.4917343>.
- [83] Qiu, W., Sun, X., Wu, C., Hjort, K. & Wu, Z. A Contact Angle Study of the Interaction between Embedded Amphiphilic Molecules and the PDMS Matrix in an Aqueous Environment. *Micromachines* **5**, 515–527 (2014). URL <https://www.mdpi.com/2072-666X/5/3/515>.
- [84] Keefe, A. J., Brault, N. D. & Jiang, S. Suppressing Surface Reconstruction of Superhydrophobic PDMS Using a Superhydrophilic Zwitterionic Polymer. *Biomacromolecules* **13**, 1683–1687 (2012). URL <https://doi.org/10.1021/bm300399s>.
- [85] Ushikubo, F. Y., Birribilli, F. S., Oliveira, D. R. B. & Cunha, R. L. Y- and T-junction microfluidic devices: effect of fluids and interface properties and operating conditions. *Microfluidics and Nanofluidics* **17**, 711–720 (2014). URL <https://doi.org/10.1007/s10404-014-1348-4>.

- [86] Bathe, K.-J. Finite Element Method. In *Wiley Encyclopedia of Computer Science and Engineering*, 1–12 (American Cancer Society, 2008). URL <http://onlinelibrary.wiley.com/doi/abs/10.1002/9780470050118.ecse159>. \_eprint: <https://onlinelibrary.wiley.com/doi/pdf/10.1002/9780470050118.ecse159>.
- [87] Jangir, P. & Jana, A. K. CFD simulation of droplet splitting at microfluidic T-junctions in oil–water two-phase flow using conservative level set method. *Journal of the Brazilian Society of Mechanical Sciences and Engineering* **41**, 75 (2019). URL <https://doi.org/10.1007/s40430-019-1569-2>.
- [88] Lei, L., Zhang, H. B., Bergstrom, D. J., Zhang, B. & Zhang, W. J. Modeling of Droplet Generation by a Modified T-Junction Device Using COMSOL. *Applied Mechanics and Materials* **705**, 112–116 (2015). URL <https://www.scientific.net/AMM.705.112>.
- [89] Jamalabadi, M. Y. A., DaqiqShirazi, M., Kosar, A. & Shadloo, M. S. Effect of injection angle, density ratio, and viscosity on droplet formation in a microfluidic T-junction. *Theoretical and Applied Mechanics Letters* **7**, 243–251 (2017). URL <https://www.sciencedirect.com/science/article/pii/S209503491730079X>.
- [90] García Pérez, M. & Vakkilainen, E. A comparison of turbulence models and two and three dimensional meshes for unsteady CFD ash deposition tools. *Fuel* **237**, 806–811 (2019). URL <https://www.sciencedirect.com/science/article/pii/S0016236118317794>.

- [91] Dimitrov, A. S., Kralchevsky, P. A., Nikolov, A. D., Noshi, H. & Matsumoto, M. Contact angle measurements with sessile drops and bubbles. *Journal of Colloid and Interface Science* **145**, 279–282 (1991). URL <https://www.sciencedirect.com/science/article/pii/002197979190120W>.
- [92] Berry, J. D., Neeson, M. J., Dagastine, R. R., Chan, D. Y. C. & Tabor, R. F. Measurement of surface and interfacial tension using pendant drop tensiometry. *Journal of Colloid and Interface Science* **454**, 226–237 (2015). URL <https://research.monash.edu/en/publications/measurement-of-surface-and-interfacial-tension-using-pendant-drop>.
- [93] Huang, E. *et al.* OpenDrop: Open-source software for pendant drop tensiometry & contact angle measurements. *Journal of Open Source Software* **6**, 2604 (2021). URL <https://joss.theoj.org/papers/10.21105/joss.02604>.
- [94] Droplet Breakup in a T-Junction. URL <https://www.comsol.com/model/droplet-breakup-in-a-t-junction-1994>.
- [95] Dubey, G. P. & Sharma, M. Thermodynamic and Transport Properties of Binary Liquid Mixtures of 1-Hexanol with Hexadecane and Squalane at 298.15, 303.15 and 308.15 K. *Zeitschrift für Physikalische Chemie* **223**, 279–298 (2009). URL <https://www.degruyter.com/document/doi/10.1524/zpch.2009.5431/html>.

- [96] Nekouei, M. & Vanapalli, S. A. Volume-of-fluid simulations in microfluidic T-junction devices: Influence of viscosity ratio on droplet size. *Physics of Fluids* **29**, 032007 (2017). URL <https://aip.scitation.org/doi/10.1063/1.4978801>.
- [97] Domańska, U., Kozłowska, M. K. & Rogalski, M. Solubilities, Partition Coefficients, Density, and Surface Tension for Imidazoles + Octan-1-ol or + Water or + n-Decane. *Journal of Chemical & Engineering Data* **47**, 456–466 (2002). URL <https://doi.org/10.1021/je0103014>.
- [98] Goebel, A. & Lunkenheimer, K. Interfacial Tension of the Water/n-Alkane Interface. *Langmuir* **13**, 369–372 (1997). URL <https://doi.org/10.1021/la960800g>.
- [99] Liu, H. & Zhang, Y. Droplet formation in a T-shaped microfluidic junction. *Journal of Applied Physics* **106**, 034906 (2009). URL <https://aip.scitation.org/doi/10.1063/1.3187831>.
- [100] Baltussen, E., Cramers, C. & Sandra, P. Sorptive sample preparation – a review. *Analytical and Bioanalytical Chemistry* **373**, 3–22 (2002). URL <https://doi.org/10.1007/s00216-002-1266-2>.
- [101] Lin, G., Zhang, X., Kumar, S. R. & Mark, J. E. Modification of Polysiloxane Networks for Biocompatibility. *Molecular Crystals and Liquid Crystals* **521**, 56–71 (2010). URL <https://doi.org/10.1080/15421401003719738>.

- [102] Baillie, T. A. Metabolism and toxicity of drugs. Two decades of progress in industrial drug metabolism. *Chemical Research in Toxicology* **21**, 129–137 (2008). URL <https://doi.org/10.1021/tx7002273>.
- [103] Chung, T. D. Y., Terry, D. B. & Smith, L. H. *In vitro and in vivo assessment of ADME and PK properties during lead selection and lead optimization – Guidelines, benchmarks and rules of thumb* (Eli Lilly & Company and the National Center for Advancing Translational Sciences, 2015, Bethesda (MD), 2015). URL <http://www.ncbi.nlm.nih.gov/books/NBK326710/>.
- [104] Institute of Medicine (US) Committee on Conflict of Interest in Medical Research, Education, and Practice. *Conflict of interest in medical research, education, and practice* (National Academies Press (US), Washington (DC), 2009). URL <http://www.ncbi.nlm.nih.gov/books/NBK22942/>.
- [105] Avdeef, A. Physicochemical profiling (solubility, permeability and charge state). *Current Topics in Medicinal Chemistry* **1**, 277–351 (2001).
- [106] Ceccarelli, M., Wagner, B., Alvarez-Sánchez, R., Cruciani, G. & Goracci, L. Use of the distribution coefficient in brain polar lipids for the assessment of drug-induced phospholipidosis risk. *Chemical Research in Toxicology* **30**, 1145–1156 (2017).
- [107] Sun, H., Chow, E. C., Liu, S., Du, Y. & Pang, K. S. The Caco-2 cell monolayer: Usefulness and limitations. *Expert Opinion on Drug Metabolism & Toxicology* **4**, 395–411 (2008). URL <http://www.tandfonline.com/doi/full/10.1517/17425255.4.4.395>.

- [108] Balimane, P. V. & Chong, S. Cell culture-based models for intestinal permeability: A critique. *Drug Discovery Today* **10**, 335–343 (2005). URL <http://www.sciencedirect.com/science/article/pii/S1359644604033549>.
- [109] Avdeef, A. *et al.* PAMPA: Critical factors for better predictions of absorption. *Journal of Pharmaceutical Sciences* **96**, 2893–2909 (2007). URL <http://www.sciencedirect.com/science/article/pii/S0022354916324054>.
- [110] Alqahtani, S., Mohamed, L. A. & Kaddoumi, A. Experimental models for predicting drug absorption and metabolism. *Expert Opinion on Drug Metabolism & Toxicology* **9**, 1241–1254 (2013). URL <https://doi.org/10.1517/17425255.2013.802772>.
- [111] Nigsch, F., Klaffke, W. & Miret, S. *In vitro* models for processes involved in intestinal absorption. *Expert Opinion on Drug Metabolism & Toxicology* **3**, 545–556 (2007). URL <https://doi.org/10.1517/17425255.3.4.545>.
- [112] Smith, D. *et al.* Passive lipoidal diffusion and carrier-mediated cell uptake are both important mechanisms of membrane permeation in drug disposition. *Molecular Pharmaceutics* **11**, 1727–1738 (2014). URL <https://doi.org/10.1021/mp400713v>.
- [113] Volpe, D. A. Drug-permeability and transporter assays in Caco-2 and MDCK cell lines. *Future Medicinal Chemistry* **3**, 2063–2077 (2011).

- [114] Irvine, J. D. *et al.* MDCK (Madin-Darby canine kidney) cells: A tool for membrane permeability screening. *Journal of Pharmaceutical Sciences* **88**, 28–33 (1999).
- [115] Balon, K., Riebesehl, B. U. & Müller, B. W. Drug liposome partitioning as a tool for the prediction of human passive intestinal absorption. *Pharmaceutical Research* **16**, 882–888 (1999). URL <https://doi.org/10.1023/A:1018882221008>.
- [116] Purushothaman, S., Cama, J. & F. Keyser, U. Dependence of norfloxacin diffusion across bilayers on lipid composition. *Soft Matter* **12**, 2135–2144 (2016). URL <https://pubs.rsc.org/en/content/articlelanding/2016/sm/c5sm02371h>.
- [117] Osiecka, I., Porter, P. A., Borchardt, R. T., Fix, J. A. & Gardner, C. R. *In vitro* drug absorption models. I. Brush border membrane vesicles, isolated mucosal cells and everted intestinal rings: Characterization and salicylate accumulation. *Pharmaceutical Research* **2**, 284–293 (1985). URL <https://doi.org/10.1023/A:1016341601273>.
- [118] Kataoka, M. *et al.* A new *in vitro* system for evaluation of passive intestinal drug absorption: Establishment of a double artificial membrane permeation assay. *European Journal of Pharmaceutics and Biopharmaceutics* **88**, 840–846 (2014).
- [119] Yu, H. *et al.* A new PAMPA model proposed on the basis of a synthetic phospholipid membrane. *PLoS One* **10**, e0116502 (2015).

- [120] Warren, R. C. *Physics and the architecture of cell membranes* (Hilger, 1987).
- [121] Taylor, G. J. & Sarles, S. A. Heating-enabled formation of droplet interface bilayers using Escherichia coli total lipid extract. *Langmuir* **31**, 325–337 (2015). URL <http://dx.doi.org/10.1021/la503471m>.
- [122] Czekalska, M. A., Kaminski, T. S., Makuch, K. & Garstecki, P. Passive and parallel microfluidic formation of droplet interface bilayers (DIBs) for measurement of leakage of small molecules through artificial phospholipid membranes. *Sensors and Actuators B: Chemical* **286**, 258–265 (2019). URL <https://doi.org/10.1016/j.snb.2019.01.143>.
- [123] Tonooka, T., Sato, K., Osaki, T., Kawano, R. & Takeuchi, S. Lipid Bilayers on a Picoliter Microdroplet Array for Rapid Fluorescence Detection of Membrane Transport. *Small* **10**, 3275–3282 (2014). URL <https://onlinelibrary.wiley.com/doi/abs/10.1002/sml1.201303332>.
- [124] Soga, N., Watanabe, R. & Noji, H. Attolitre-sized lipid bilayer chamber array for rapid detection of single transporters. *Scientific Reports* **5**, 1–8 (2015). URL <https://www.nature.com/articles/srep11025>.
- [125] Urban, M. *et al.* Highly Parallel Transport Recordings on a Membrane-on-Nanopore Chip at Single Molecule Resolution. *Nano Letters* **14**, 1674–1680 (2014). URL <https://doi.org/10.1021/nl5002873>.
- [126] Abbyad, P., Dangla, R., Alexandrou, A. & Baroud, C. N. Rails and anchors: guiding and trapping droplet microreactors in two dimensions. *Lab on a Chip*



- 11**, 813–821 (2011). URL <https://pubs.rsc.org/en/content/articlelanding/2011/lc/c01c00104j>.
- [127] van Meer, G., Voelker, D. R. & Feigenson, G. W. Membrane lipids: where they are and how they behave. *Nature Reviews Molecular Cell Biology* **9**, 112–124 (2008). URL <https://www.ncbi.nlm.nih.gov/pmc/articles/PMC2642958/>.
- [128] Jones, H. M. & Rowland Yeo, K. Basic Concepts in Physiologically Based Pharmacokinetic Modeling in Drug Discovery and Development. *CPT: Pharmacometrics & Systems Pharmacology* **2**, 63 (2013). URL <https://ascpt.onlinelibrary.wiley.com/doi/abs/10.1038/psp.2013.41>.
- [129] Stippler, E., Kopp, S. & Dressman, J. B. Comparison of US pharmacopeia simulated intestinal fluid TS (without pancreatin) and phosphate standard buffer pH 6.8, TS of the international pharmacopoeia with respect to their use in *in vitro* dissolution testing. *Dissolution Technologies* **11**, 6–10 (2004). URL [http://www.dissolutiontech.com/DTresour/200405Articles/DT200405\\_A01.pdf](http://www.dissolutiontech.com/DTresour/200405Articles/DT200405_A01.pdf).
- [130] Lang, F. Mechanisms and significance of cell volume regulation. *Journal of the American College of Nutrition* **26**, 613S–623S (2006).
- [131] Gilbert, D. L. Buffering of blood plasma. *The Yale Journal of Biology and Medicine* **32**, 378–389 (1960). URL <https://www.ncbi.nlm.nih.gov/pmc/articles/PMC2604138/>.

- [132] Sugano, K. *et al.* Optimized conditions of bio-mimetic artificial membrane permeation assay. *International Journal of Pharmaceutics* **228**, 181–188 (2001).
- [133] Proulx, P. Structure-function relationships in intestinal brush border membranes. *Biochimica et Biophysica Acta* **1071**, 255–271 (1991).
- [134] Forstner, G. G., Tanaka, K. & Isselbacher, K. J. Lipid composition of the isolated rat intestinal microvillus membrane. *Biochemical Journal* **109**, 51–59 (1968). URL <http://www.biochemj.org/content/109/1/51>.
- [135] Schwarz, S. M., Hostetler, B., Ling, S., Mone, M. & Watkins, J. B. Intestinal membrane lipid composition and fluidity during development in the rat. *American Journal of Physiology-Gastrointestinal and Liver Physiology* **248**, G200–G207 (1985). URL <http://www.physiology.org/doi/abs/10.1152/ajpgi.1985.248.2.g200>.
- [136] Brasitus, T. A., Yeh, K.-Y., Holt, P. R. & Schachter, D. Lipid fluidity and composition of intestinal microvillus membranes isolated from rats of different ages. *Biochimica et Biophysica Acta - Biomembranes* **778**, 341–348 (1984). URL <http://www.sciencedirect.com/science/article/pii/000527368490378X>.
- [137] Christiansen, K. & Carlsen, J. Microvillus membrane vesicles from pig small intestine Purity and lipid composition. *Biochimica et Biophysica Acta - Biomembranes* **647**, 188–195 (1981). URL <http://www.sciencedirect.com/science/article/pii/0005273681902455>.

- [138] Hauser, H., Howell, K., Dawson, R. M. C. & Bowyer, D. E. Rabbit small intestinal brush border membrane. Preparation and lipid composition. *Biochimica et Biophysica Acta - Biomembranes* **602**, 567–577 (1980). URL <http://www.sciencedirect.com/science/article/pii/0005273680903351>.
- [139] Brasitus, T. A., Davidson, N. O. & Schachter, D. Variations in dietary triacylglycerol saturation alter the lipid composition and fluidity of rat intestinal plasma membranes. *Biochimica et Biophysica Acta - Biomembranes* **812**, 460–472 (1985). URL <http://www.sciencedirect.com/science/article/pii/0005273685903219>.
- [140] Ginzberg, M. B., Kafri, R. & Kirschner, M. On being the right (cell) size. *Science* **348**, 1245075 (2015). URL <https://science.sciencemag.org/content/348/6236/1245075>.
- [141] MacLeod, R. J. *et al.* Corticostatic peptides cause nifedipine-sensitive volume reduction in jejunal villus enterocytes. *Proceedings of the National Academy of Sciences of the United States of America* **88**, 552–556 (1991).
- [142] Buschmann, R. J. & Manke, D. J. Morphometric analysis of the membranes and organelles of small intestinal enterocytes. I. Fasted hamster. *Journal of Ultrastructure Research* **76**, 1–14 (1981).
- [143] Crowe, P. T. & Marsh, M. N. Morphometric analysis of small intestinal mucosa. IV. Determining cell volumes. *Virchows Archiv. A, Pathological Anatomy and Histopathology* **422**, 459–466 (1993).

- [144] Stein, S., Bogdahn, M., Rosenbaum, C., Weitschies, W. & Seidlitz, A. Distribution of fluorescein sodium and triamcinolone acetonide in the simulated liquefied and vitrectomized Vitreous Model with simulated eye movements. *European Journal of Pharmaceutical Sciences* **109**, 233–243 (2017).
- [145] Khosroshahi, M. E. & Mahmoodi, M. Fabrication, visualization and analysis of fluorescein sodium encapsulated PLGA@CS nanoparticles as model for photothermomechanical drug delivery using pulsed 532 nm laser. *Advances in Nanoparticles* **7**, 720–726 (2018). URL <https://m.scirp.org/papers/abstract/87066>.
- [146] Liu, Y., Miyoshi, H. & Nakamura, M. Novel drug delivery system of hollow mesoporous silica nanocapsules with thin shells: Preparation and fluorescein isothiocyanate (FITC) release kinetics. *Colloids and Surfaces B: Biointerfaces* **58**, 180–187 (2007). URL <http://www.sciencedirect.com/science/article/pii/S0927776507001191>.
- [147] Fisher, K. A., Huddersman, K. D. & Taylor, M. J. Comparison of micro- and mesoporous inorganic materials in the uptake and release of the drug model fluorescein and its analogues. *Chemistry - A European Journal* **9**, 5873–5878 (2003). URL <https://onlinelibrary.wiley.com/doi/abs/10.1002/chem.200304764>.
- [148] Maurer, J. M. *et al.* Gastrointestinal pH and transit time profiling in healthy volunteers using the IntelliCap system confirms ileo-colonic release of ColoPulse

- tablets. *PLoS One* **10**, 1–17 (2015). URL <https://www.ncbi.nlm.nih.gov/pmc/articles/PMC4503763/>.
- [149] Kokubo, T. & Takadama, H. How useful is SBF in predicting *in vivo* bone bioactivity? *Biomaterials* **27**, 2907–2915 (2006). URL <http://www.sciencedirect.com/science/article/pii/S0142961206000457>.
- [150] Debon, A. P., Wootton, R. C. R. & Elvira, K. S. Droplet confinement and leakage: Causes, underlying effects, and amelioration strategies. *Biomicrofluidics* **9**, 024119 (2015). URL <https://aip.scitation.org/doi/10.1063/1.4917343>.
- [151] Berginc, K., Žakelj, S., Levstik, L., Uršič, D. & Kristl, A. Fluorescein transport properties across artificial lipid membranes, Caco-2 cell monolayers and rat jejunum. *European Journal of Pharmaceutics and Biopharmaceutics* **66**, 281–285 (2007). URL <http://www.sciencedirect.com/science/article/pii/S0939641106002931>.
- [152] Sjöback, R., Nygren, J. & Kubista, M. Characterization of fluorescein-oligonucleotide conjugates and measurement of local electrostatic potential. *Biopolymers* **46**, 445–453 (1998). URL <https://onlinelibrary.wiley.com/doi/abs/10.1002/%28SICI%291097-0282%28199812%2946%3A7%3C445%3A%3AAID-BIP2%3E3.0.CO%3B2-5>.

- [153] Martin, M. M. & Lindqvist, L. The pH dependence of fluorescein fluorescence. *Journal of Luminescence* **10**, 381–390 (1975). URL <http://www.sciencedirect.com/science/article/pii/0022231375900034>.
- [154] Doughty, M. J. pH dependent spectral properties of sodium fluorescein ophthalmic solutions revisited. *Ophthalmic & Physiological Optics: The Journal of the British College of Ophthalmic Opticians (Optometrists)* **30**, 167–174 (2010).
- [155] Worthley, L. I. G., Guerin, M. & Pain, R. W. For Calculating Osmolality, the Simplest Formula is the Best. *Anaesthesia and Intensive Care* **15**, 199–202 (1987). URL <https://doi.org/10.1177/0310057X8701500214>.
- [156] Alves, A. C., Ribeiro, D., Nunes, C. & Reis, S. Biophysics in cancer: The relevance of drug-membrane interaction studies. *BBA - Biomembranes* **1858**, 2231–2244 (2016). URL <http://www.sciencedirect.com/science/article/pii/S0005273616302334>.
- [157] Ran, S. & Thorpe, P. E. Phosphatidylserine is a marker of tumor vasculature and a potential target for cancer imaging and therapy. *International Journal of Radiation Oncology, Biology, Physics* **54**, 1479–1484 (2002). URL <https://www.sciencedirect.com/science/article/pii/S0360301602039287>.
- [158] Gallois, L., Fiallo, M. & Garnier-Suillerot, A. Comparison of the interaction of doxorubicin, daunorubicin, idarubicin and idarubicinol with large

- unilamellar vesicles: Circular dichroism study. *BBA - Biomembranes* **1370**, 31–40 (1998). URL <https://www.sciencedirect.com/science/article/pii/S0005273697002411>.
- [159] Johnson, L. W., Hughes, M. E. & Zilversmit, D. B. Use of phospholipid exchange protein to measure inside-outside transposition in phosphatidylcholine liposomes. *BBA - Biomembranes* **375**, 176–185 (1975). URL <https://www.sciencedirect.com/science/article/pii/000527367590187X>.
- [160] Cheng, H.-T., Megha & London, E. Preparation and Properties of Asymmetric Vesicles That Mimic Cell Membranes. *Journal of Biological Chemistry* **284**, 6079–6092 (2009). URL [https://www.jbc.org/article/S0021-9258\(20\)32635-1/abstract](https://www.jbc.org/article/S0021-9258(20)32635-1/abstract).
- [161] Pautot, S., Frisken, B. J. & Weitz, D. A. Engineering asymmetric vesicles. *Proceedings of the National Academy of Sciences* **100**, 10718–10721 (2003). URL <https://www.pnas.org/content/100/19/10718>.
- [162] Hu, P. C., Li, S. & Malmstadt, N. Microfluidic Fabrication of Asymmetric Giant Lipid Vesicles. *ACS Applied Materials & Interfaces* **3**, 1434–1440 (2011). URL <https://doi.org/10.1021/am101191d>.
- [163] Rivel, T., Ramseyer, C. & Yesylevskyy, S. The asymmetry of plasma membranes and their cholesterol content influence the uptake of cisplatin. *Scientific Reports* **9**, 5627 (2019). URL <https://www.nature.com/articles/s41598-019-41903-w>.

- [164] Taylor, G. *et al.* Electrophysiological interrogation of asymmetric droplet interface bilayers reveals surface-bound alamethicin induces lipid flip-flop. *BBA - Biomembranes* **1861**, 335–343 (2019). URL <https://doi.org/10.1016/j.bbamem.2018.07.001>.
- [165] Barlow, N. E. *et al.* Measuring bilayer surface energy and curvature in asymmetric droplet interface bilayers. *Journal of The Royal Society Interface* **15**, 20180610 (2018). URL <https://royalsocietypublishing.org/doi/full/10.1098/rsif.2018.0610>.
- [166] Zachowski, A. Phospholipids in animal eukaryotic membranes: transverse asymmetry and movement. *Biochemical Journal* **294**, 1–14 (1993). URL <https://www.ncbi.nlm.nih.gov/pmc/articles/PMC1134557/>.
- [167] Lingwood, D. & Simons, K. Lipid Rafts As a Membrane-Organizing Principle. *Science* **327**, 46–50 (2010). URL <https://science.sciencemag.org/content/327/5961/46>.
- [168] Morgan, J. J., Stumm, W. & Hem, J. D. Water. In *Kirk-Othmer Encyclopedia of Chemical Technology* (American Cancer Society, 2006). URL <http://onlinelibrary.wiley.com/doi/abs/10.1002/0471238961.1618151613151807.a01.pub2>. \_eprint: <https://onlinelibrary.wiley.com/doi/pdf/10.1002/0471238961.1618151613151807.a01.pub2>.
- [169] O’Neil, M. The Merck Index - An Encyclopedia of Chemicals, Drugs, and



- Biologicals. In *The Merck Index - An Encyclopedia of Chemicals, Drugs, and Biologicals*, 1624 (Royal Society of Chemistry, Cambridge, UK, 2013).
- [170] David, R. *et al.* Tissue cohesion and the mechanics of cell rearrangement. *Development* **141**, 3672–3682 (2014). URL <https://doi.org/10.1242/dev.104315>.
- [171] Kamal, M. M., Mills, D., Grzybek, M. & Howard, J. Measurement of the membrane curvature preference of phospholipids reveals only weak coupling between lipid shape and leaflet curvature. *Proceedings of the National Academy of Sciences* **106**, 22245–22250 (2009). URL <https://www.pnas.org/content/106/52/22245>.
- [172] Goldman, R., Facchinetti, T., Bach, D., Raz, A. & Shinitzky, M. A differential interaction of daunomycin, adriamycin and their derivatives with human erythrocytes and phospholipid bilayers. *BBA - Biomembranes* **512**, 254–269 (1978).
- [173] Bogorad, M. I. & Searson, P. C. Real-time Imaging and Quantitative Analysis of Doxorubicin Transport in a Perfusable Microvessel Platform. *Integrative Biology* **8**, 976–984 (2016). URL <https://www.ncbi.nlm.nih.gov/pmc/articles/PMC5035133/>.
- [174] Hwang, W. L., Holden, M. A., White, S. & Bayley, H. Electrical Behavior of Droplet Interface Bilayer Networks: Experimental Analysis and Modeling. *Journal of the American Chemical Society* **129**, 11854–11864 (2007). URL <https://doi.org/10.1021/ja074071a>.

- [175] Livingston, J. N. *et al.* Binding and molecular weight properties of the insulin receptor from omental and subcutaneous adipocytes in human obesity. *Diabetologia* **27**, 447–453 (1984). URL <https://doi.org/10.1007/BF00273909>.
- [176] Malmstadt, N., Nash, M. A., Purnell, R. F. & Schmidt, J. J. Automated Formation of Lipid-Bilayer Membranes in a Microfluidic Device. *Nano Letters* **6**, 1961–1965 (2006). URL <https://doi.org/10.1021/nl0611034>.
- [177] Sarles, S. A. & Leo, D. J. Tailored Current—Voltage Relationships of Droplet-Interface Bilayers Using Biomolecules and External Feedback Control. *Journal of Intelligent Material Systems and Structures* **20**, 1233–1247 (2009). URL <https://doi.org/10.1177/1045389X09104390>.
- [178] Aghdaei, S., Sandison, M. E., Zagnoni, M., Green, N. G. & Morgan, H. Formation of artificial lipid bilayers using droplet dielectrophoresis. *Lab on a Chip* **8**, 1617 (2008). URL <http://xlink.rsc.org/?DOI=b807374k>.
- [179] Renner, S., Geltinger, S. & Simmel, F. C. Nanopore translocation and force spectroscopy experiments in microemulsion droplets. *Small (Weinheim an Der Bergstrasse, Germany)* **6**, 190–194 (2010).
- [180] Poulos, J. L., Nelson, W. C., Jeon, T.-J., Kim, C.-J. & Schmidt, J. J. Electrowetting on dielectric-based microfluidics for integrated lipid bilayer formation and measurement. *Applied Physics Letters* **95**, 013706 (2009). URL <https://aip.scitation.org/doi/10.1063/1.3167283>.

- [181] Creasy, M. A. & Leo, D. J. Non-invasive measurement techniques for measuring properties of droplet interface bilayers. *Smart Materials and Structures* **19**, 094016 (2010). URL <https://doi.org/10.1088/0964-1726/19/9/094016>.
- [182] Sarles, S. A. & Leo, D. J. Physical encapsulation of droplet interface bilayers for durable, portable biomolecular networks. *Lab on a Chip* **10**, 710–717 (2010).
- [183] Sarles, S. A. & Leo, D. J. Regulated Attachment Method for Reconstituting Lipid Bilayers of Prescribed Size within Flexible Substrates. *Analytical Chemistry* **82**, 959–966 (2010). URL <https://doi.org/10.1021/ac902555z>.
- [184] Punnamaraju, S. & Steckl, A. J. Voltage Control of Droplet Interface Bilayer Lipid Membrane Dimensions. *Langmuir* **27**, 618–626 (2011). URL <https://doi.org/10.1021/la1036508>.
- [185] Syeda, R., Holden, M. A., Hwang, W. L. & Bayley, H. Screening Blockers Against a Potassium Channel with a Droplet Interface Bilayer Array. *Journal of the American Chemical Society* **130**, 15543–15548 (2008). URL <http://dx.doi.org/10.1021/ja804968g>.
- [186] Huang, J., Lein, M., Gunderson, C. & Holden, M. A. Direct Quantitation of Peptide-Mediated Protein Transport across a Droplet–Interface Bilayer. *Journal of the American Chemical Society* **133**, 15818–15821 (2011). URL <https://doi.org/10.1021/ja2046342>.

- [187] Barriga, H. M. G. *et al.* Droplet interface bilayer reconstitution and activity measurement of the mechanosensitive channel of large conductance from *Escherichia coli*. *Journal of the Royal Society Interface* **11** (2014). URL <https://www.ncbi.nlm.nih.gov/pmc/articles/PMC4233688/>.
- [188] Najem, J. S. *et al.* Multifunctional, Micropipette-based Method for Incorporation And Stimulation of Bacterial Mechanosensitive Ion Channels in Droplet Interface Bilayers. *Journal of Visualized Experiments: JoVE* (2015).
- [189] El-Beyrouthy, J., Makhoul-Mansour, M. M., Taylor, G., Sarles, S. A. & Freeman, E. C. A new approach for investigating the response of lipid membranes to electrocompression by coupling droplet mechanics and membrane biophysics. *Journal of The Royal Society Interface* **16**, 20190652 (2019). URL <https://royalsocietypublishing.org/doi/10.1098/rsif.2019.0652>.
- [190] Zhang, Y., Bracken, H., Woolhead, C. & Zagnoni, M. Functionalisation of human chloride intracellular ion channels in microfluidic droplet-interface-bilayers. *Biosensors and Bioelectronics* **150**, 111920 (2020). URL <https://doi.org/10.1016/j.bios.2019.111920>.
- [191] Carreras, P., Law, R. V., Brooks, N., Seddon, J. M. & Ces, O. Microfluidic generation of droplet interface bilayer networks incorporating real-time size sorting in linear and non-linear configurations. *Biomicrofluidics* **8** (2014). URL <https://doi.org/10.1063/1.4897495>.

- [192] Elani, Y., Solvas, X. C. I., Edel, J. B., Law, R. V. & Ces, O. Microfluidic generation of encapsulated droplet interface bilayer networks (multisomes) and their use as cell-like reactors. *Chemical Communications* **52**, 5961–5964 (2016). URL <https://doi.org/10.1039/c6cc01434h>.
- [193] Winterhalter, M. Black lipid membranes. *Current Opinion in Colloid & Interface Science* **5**, 250–255 (2000). URL [https://doi.org/10.1016/S1359-0294\(00\)00063-7](https://doi.org/10.1016/S1359-0294(00)00063-7).
- [194] Oiki, S. Planar Lipid Bilayer Method for Studying Channel Molecules. In Okada, Y. (ed.) *Patch Clamp Techniques: From Beginning to Advanced Protocols*, Springer Protocols Handbooks, 229–275 (Springer Japan, Tokyo, 2012). URL [https://doi.org/10.1007/978-4-431-53993-3\\_16](https://doi.org/10.1007/978-4-431-53993-3_16).
- [195] Peetla, C., Stine, A. & Labhasetwar, V. Biophysical interactions with model lipid membranes: applications in drug discovery and drug delivery. *Molecular pharmaceutics* **6**, 1264–1276 (2009). URL <https://www.ncbi.nlm.nih.gov/pmc/articles/PMC2757518/>.
- [196] Elani, Y., deMello, A. J., Niu, X. & Ces, O. Novel technologies for the formation of 2-D and 3-D droplet interface bilayer networks. *Lab on a Chip* **12**, 3514–3520 (2012). URL <https://doi.org/10.1039/C2LC40287D>.
- [197] Tamaddoni, N., Taylor, G., Hepburn, T., Kilbey, S. M. & Sarles, S. A. Reversible, voltage-activated formation of biomimetic membranes between tri-block copolymer-coated aqueous droplets in good solvents. *Soft Matter* **12**, 5096–5109 (2016). URL <https://doi.org/10.1039/C6SM00400H>.

- [198] Taylor, G. J. *et al.* Capacitive Detection of Low-Enthalpy, Higher-Order Phase Transitions in Synthetic and Natural Composition Lipid Membranes. *Langmuir* **33**, 10016–10026 (2017). URL <https://doi.org/10.1021/acs.langmuir.7b02022>.
- [199] Najem, J. S. *et al.* Memristive Ion Channel-Doped Biomembranes as Synaptic Mimics. *ACS Nano* **12**, 4702–4711 (2018). URL <https://doi.org/10.1021/acsnano.8b01282>.
- [200] Michalak, Z., Muzzio, M., Milianta, P. J., Giacomini, R. & Lee, S. Effect of Monoglyceride Structure and Cholesterol Content on Water Permeability of the Droplet Bilayer. *Langmuir* **29**, 15919–15925 (2013). URL <https://doi.org/10.1021/la4040535>.
- [201] Lopez, M., Evangelista, S. E., Morales, M. & Lee, S. Enthalpic Effects of Chain Length and Unsaturation on Water Permeability across Droplet Bilayers of Homologous Monoglycerides. *Langmuir* **33**, 900–912 (2017). URL <https://doi.org/10.1021/acs.langmuir.6b03932>.
- [202] Lopez, M. *et al.* Effects of Acyl Chain Unsaturation on Activation Energy of Water Permeability across Droplet Bilayers of Homologous Monoglycerides: Role of Cholesterol. *Langmuir* **34**, 2147–2157 (2018). URL <https://doi.org/10.1021/acs.langmuir.7b03590>.
- [203] Taylor, G. J., Venkatesan, G. A., Collier, C. P. & Sarles, S. A. Direct in situ measurement of specific capacitance, monolayer tension,

- and bilayer tension in a droplet interface bilayer. *Soft Matter* **11**, 7592–7605 (2015). URL <https://pubs.rsc.org/en/content/articlelanding/2015/sm/c5sm01005e>.
- [204] de Wit, G., Danial, J. S. H., Kukura, P. & Wallace, M. I. Dynamic label-free imaging of lipid nanodomains. *Proceedings of the National Academy of Sciences* **112**, 12299–12303 (2015).
- [205] McMahon, H. T. & Boucrot, E. Membrane curvature at a glance. *Journal of Cell Science* **128**, 1065–1070 (2015). URL <https://doi.org/10.1242/jcs.114454>.
- [206] Yanagisawa, M., Yoshida, T.-a., Furuta, M., Nakata, S. & Tokita, M. Adhesive force between paired microdroplets coated with lipid monolayers. *Soft Matter* **9**, 5891–5897 (2013). URL <https://pubs.rsc.org/en/content/articlelanding/2013/sm/c3sm50938a>.
- [207] Gross, L. C. M., Heron, A. J., Baca, S. C. & Wallace, M. I. Determining Membrane Capacitance by Dynamic Control of Droplet Interface Bilayer Area. *Langmuir* **27**, 14335–14342 (2011). URL <https://doi.org/10.1021/la203081v>.
- [208] Liu, P., Zabala-Ferrera, O. & Beltramo, P. J. Fabrication and electromechanical characterization of freestanding asymmetric membranes. *Biophysical Journal* **120**, 1755–1764 (2021). URL <https://www.sciencedirect.com/science/article/pii/S0006349521001946>.

- [209] Beltramo, P. J., Scheidegger, L. & Vermant, J. Toward Realistic Large-Area Cell Membrane Mimics: Excluding Oil, Controlling Composition, and Including Ion Channels. *Langmuir* (2018). URL <https://doi.org/10.1021/acs.langmuir.8b00837>.
- [210] Milianta, P. J., Muzzio, M., Denver, J., Cawley, G. & Lee, S. Water Permeability across Symmetric and Asymmetric Droplet Interface Bilayers: Interaction of Cholesterol Sulfate with DPhPC. *Langmuir* **31**, 12187–12196 (2015). URL <https://doi.org/10.1021/acs.langmuir.5b02748>.
- [211] Braziel, S., Sullivan, K. & Lee, S. Quantitative Raman microspectroscopy for water permeability parameters at a droplet interface bilayer. *Analyst* **143**, 747–755 (2018). URL <https://doi.org/10.1039/C7AN01349C>.
- [212] Valet, M., Pontani, L.-L., Voituriez, R., Wandersman, E. & Prevost, A. Diffusion through Nanopores in Connected Lipid Bilayer Networks. *Physical Review Letters* **123**, 088101 (2019). URL <https://doi.org/10.1103/PhysRevLett.123.088101>.
- [213] Barlow, N. E. *et al.* Rheological Droplet Interface Bilayers (rheo-DIBs): Probing the Unstirred Water Layer Effect on Membrane Permeability via Spinning Disk Induced Shear Stress. *Scientific Reports* **7**, 1–12 (2017). URL <https://doi.org/10.1038/s41598-017-17883-0>.
- [214] A lipid-based parallel processor for chemical signals | bioRxiv. URL <https://www.biorxiv.org/content/10.1101/2021.05.05.442835v1>.



- [215] Li, X., Huang, J., Holden, M. A. & Chen, M. Peptide-Mediated Membrane Transport of Macromolecular Cargo Driven by Membrane Asymmetry. *Analytical Chemistry* **89**, 12369–12374 (2017). URL <https://doi.org/10.1021/acs.analchem.7b03421>.
- [216] Wood, M. *et al.* Ibuprofen and the Phosphatidylcholine Bilayer: Membrane Water Permeability in the Presence and Absence of Cholesterol. *Langmuir* **37**, 4468–4480 (2021). URL <https://doi.org/10.1021/acs.langmuir.0c03638>.
- [217] Allen-Benton, M., Findlay, H. E. & Booth, P. J. Probing membrane protein properties using droplet interface bilayers. *Experimental Biology and Medicine* **244**, 709–720 (2019). URL <https://doi.org/10.1177/1535370219847939>.
- [218] Booth, M. J., Cazimoglu, I. & Bayley, H. Controlled deprotection and release of a small molecule from a compartmented synthetic tissue module. *Communications Chemistry* **2**, 1–8 (2019). URL <https://doi.org/10.1038/s42004-019-0244-y>.
- [219] Leptihn, S., Thompson, J. R., Ellory, J. C., Tucker, S. J. & Wallace, M. I. In Vitro Reconstitution of Eukaryotic Ion Channels Using Droplet Interface Bilayers. *Journal of the American Chemical Society* **133**, 9370–9375 (2011). URL <https://doi.org/10.1021/ja200128n>.
- [220] Smith, S. M. Strategies for the Purification of Membrane Proteins. In *Protein Chromatography*, Methods in Molecular Biology, 485–496 (Humana Press,

- 2011). URL [https://doi.org/10.1007/978-1-60761-913-0\\_29](https://doi.org/10.1007/978-1-60761-913-0_29).
- [221] Najem, J. S. *et al.* Activation of bacterial channel MscL in mechanically stimulated droplet interface bilayers. *Scientific Reports* **5**, 13726 (2015). URL <https://doi.org/10.1038/srep13726>.
- [222] Strutt, R. *et al.* Activating mechanosensitive channels embedded in droplet interface bilayers using membrane asymmetry. *Chem. Sci.* **12**, 2138–2145 (2021). URL <http://dx.doi.org/10.1039/D0SC03889J>.
- [223] Restrepo Schild, V. *et al.* Light-Patterned Current Generation in a Droplet Bilayer Array. *Scientific Reports* **7**, 46585 (2017). URL <https://www.nature.com/articles/srep46585>.
- [224] Alcinesio, A. *et al.* Controlled packing and single-droplet resolution of 3D-printed functional synthetic tissues. *Nature Communications* **11**, 2105 (2020). URL <https://www.nature.com/articles/s41467-020-15953-y>.
- [225] Graham, A. D. *et al.* High-Resolution Patterned Cellular Constructs by Droplet-Based 3D Printing. *Scientific Reports* **7**, 7004 (2017). URL <https://www.nature.com/articles/s41598-017-06358-x>.
- [226] Challita, E. J., Makhoul-Mansour, M. M. & Freeman, E. C. Reconfiguring droplet interface bilayer networks through sacrificial membranes. *Biomicroflu-*

- idics* **12**, 034112 (2018). URL <https://aip.scitation.org/doi/abs/10.1063/1.5023386>.
- [227] Villar, G., Heron, A. J. & Bayley, H. Formation of droplet networks that function in aqueous environments. *Nature Nanotechnology* **6**, 803–808 (2011). URL <https://www.nature.com/articles/nnano.2011.183>.
- [228] Maglia, G. *et al.* Droplet networks with incorporated protein diodes show collective properties. *Nature Nanotechnology* **4**, 437–440 (2009). URL <https://doi.org/10.1038/nnano.2009.121>.
- [229] Bayoumi, M., Bayley, H., Maglia, G. & Sapra, K. T. Multi-compartment encapsulation of communicating droplets and droplet networks in hydrogel as a model for artificial cells. *Scientific Reports* **7**, 45167 (2017). URL <https://www.nature.com/articles/srep45167>.
- [230] Challita, E. J., Najem, J. S., Monroe, R., Leo, D. J. & Freeman, E. C. Encapsulating Networks of Droplet Interface Bilayers in a Thermoreversible Organogel. *Scientific Reports* **8**, 6494 (2018). URL <https://www.nature.com/articles/s41598-018-24720-5>.
- [231] Shen, H.-H., Lithgow, T. & Martin, L. L. Reconstitution of Membrane Proteins into Model Membranes: Seeking Better Ways to Retain Protein Activities. *International Journal of Molecular Sciences* **14**, 1589–1607 (2013). URL <https://www.ncbi.nlm.nih.gov/pmc/articles/PMC3565336/>.

- [232] Rofeh, J. & Theogarajan, L. Instantaneous tension measurements in droplet interface bilayers using an inexpensive, integrated pendant drop camera. *Soft Matter* **16**, 4484–4493 (2020). URL <https://pubs.rsc.org/en/content/articlelanding/2020/sm/d0sm00418a>.
- [233] Creasy, M. A. & Leo, D. J. Non-invasive measurement techniques for measuring properties of droplet interface bilayers. *Smart Materials and Structures* **19**, 094016 (2010). URL <https://doi.org/10.1088/0964-1726/19/9/094016>.
- [234] Okuno, D. *et al.* A Simple Method for Ion Channel Recordings Using Fine Gold Electrode. *Analytical Sciences* **32**, 1353–1357 (2016).
- [235] Shoji, K., Kawano, R. & White, R. J. Recessed Ag/AgCl Microelectrode-Supported Lipid Bilayer for Nanopore Sensing. *Analytical Chemistry* **92**, 10856–10862 (2020). URL <https://doi.org/10.1021/acs.analchem.0c02720>.
- [236] Challita, E. J. & Freeman, E. C. Hydrogel Microelectrodes for the Rapid, Reliable, and Repeatable Characterization of Lipid Membranes. *Langmuir* **34**, 15166–15173 (2018). URL <https://doi.org/10.1021/acs.langmuir.8b02867>.
- [237] Makhoul-Mansour, M. M. & Freeman, E. C. Droplet-Based Membranous Soft Materials. *Langmuir* **37**, 3231–3247 (2021). URL <https://doi.org/10.1021/acs.langmuir.0c03289>.

- [238] Sarles, S. A., Madden, J. D. W. & Leo, D. J. Hair cell inspired mechanotransduction with a gel-supported, artificial lipid membrane. *Soft Matter* **7**, 4644 (2011). URL <https://doi.org/10.1039/C1SM05120B>.
- [239] Tamaddoni, N., Freeman, E. C. & Sarles, S. A. Sensitivity and directionality of lipid bilayer mechanotransduction studied using a revised, highly durable membrane-based hair cell sensor. *Smart Materials and Structures* **24**, 065014 (2015). URL <https://doi.org/10.1088/0964-1726/24/6/065014>.
- [240] Venkatesan, G. A. *et al.* Evaporation-induced monolayer compression improves droplet interface bilayer formation using unsaturated lipids. *Biomechanics* **12** (2018). URL <https://doi.org/10.1063/1.5016523>.
- [241] Dupin, A. & Simmel, F. C. Signalling and differentiation in emulsion-based multi-compartmentalized in vitro gene circuits. *Nature Chemistry* **11**, 32–39 (2019). URL <https://www.nature.com/articles/s41557-018-0174-9>.
- [242] Farley, S., Ramsay, K. & Elvira, K. S. A plug-and-play modular microcapillary platform for the generation of multicompartmental double emulsions using glass or fluorocarbon capillaries. *Lab on a Chip* (2021). URL <https://pubs.rsc.org/en/content/articlelanding/2021/lc/d1lc00126d>.
- [243] E. Barlow, N. *et al.* Multiplexed droplet Interface bilayer formation. *Lab on*

*a Chip* **16**, 4653–4657 (2016). URL <https://www.doi.org/10.1039/C6LC01011C>.

- [244] Scheuble, N. *et al.* Microfluidic Technique for the Simultaneous Quantification of Emulsion Instabilities and Lipid Digestion Kinetics. *Analytical Chemistry* **89**, 9116–9123 (2017). URL <https://doi.org/10.1021/acs.analchem.7b01853>.

# **Appendices**

## **Appendix A**

### **Droplet Interface Bilayers: How can they achieve their full potential?**

Included in this appendix is a perspective review on the DIBs field, written collaboratively with my colleague Jaime Korner, and my supervisor Katherine Elvira. Jaime and I contributed equally to the writing of this work. The work herein has been submitted to Nature Chemistry, and has been peer-reviewed (changes submitted July 7, 2021). The text herein is subject to change prior to publication, and is a snapshot of the manuscript at the time of writing.



## A.1 Abstract

Model membranes can be used to elucidate the intricacies of the chemical processes that occur in cell membranes. But the perfectly biomimetic, yet bespoke, model membrane has yet to be built. Droplet interface bilayers (DIBs) are a new type of model membrane that are able to mimic some features of real cell membranes better than traditional models such as liposomes and black lipid membranes. In this perspective we discuss recent work in the field that is starting to showcase the potential of these model membranes to enable the quantification of membrane processes, such as the behaviour of protein transporters and the prediction of *in vivo* drug movement. We will also highlight the challenges remaining to enable DIBs to achieve their full potential as artificial cells, and as a biological analytical platforms for quantifying molecular transport.

## A.2 Introduction

Unanswered questions about the chemistry of fundamental biological mechanisms often drive the development of new analytical techniques. One such example is the use of droplet interface bilayers (DIBs) as tools for the analysis and quantification of membrane processes. DIBs are a type of artificial bilayer created by amphiphilic molecules at the interface between two aqueous droplets in a surrounding immiscible (usually oil) phase (Figure A.1A). Each droplet in a DIB is effectively a compartment

on either side of the artificial bilayer, which can hence be used to quantify molecular transport across it.

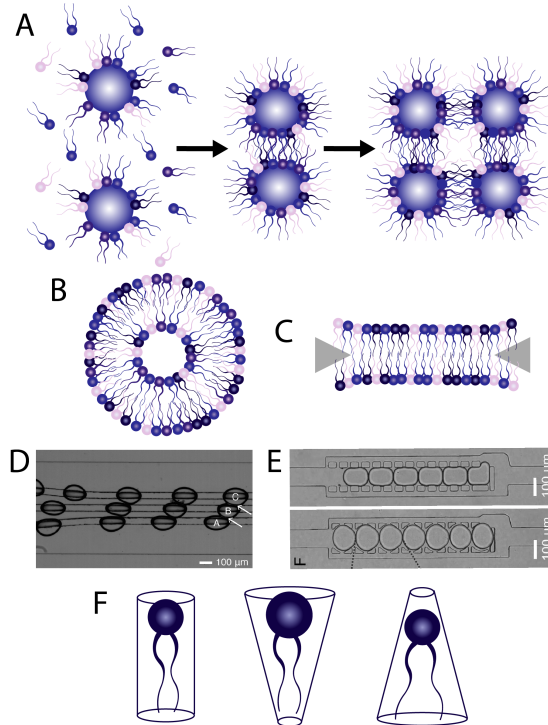
From a classical perspective, DIBs can be said to provide answers to many of the shortcomings of other model membrane systems, such as liposomes (Figure A.1B) and black lipid membranes (BLMs) (Figure A.1C). DIBs are easier to make, their formation can be automated using microfluidic technologies, they can be arranged to create complex networks that exhibit emergent properties similar to those found in cells and tissues<sup>174</sup> and can be made with volumes similar to those of human cells<sup>55,175</sup>. They also have the potential to mimic features of real cell membranes such as asymmetry<sup>13,39</sup> and curvature<sup>165</sup>. However, to the detriment of the field, DIBs have generally been made from one type of synthetic phospholipid (1,2-diphytanoyl-sn-glycero-3-phosphocholine, DPhPC)<sup>176</sup> and used mostly to study the transport of fluorescent dyes passively or through membrane pores such as  $\alpha$ -hemolysin<sup>176</sup>, alamethicin<sup>177</sup>, gramicidin<sup>178</sup> and bacteriorhodopsin<sup>38</sup>.

A quantitative analysis of all DIB publications shows that research into the formation and use of DIBs has been growing steadily over the last 15 years. Early work focused on the formation of DIBs using almost exclusively DPhPC<sup>179,180</sup> and the use of electronic measurements to study the pore forming proteins and peptides alamethicin<sup>181,182</sup> and  $\alpha$ -hemolysin<sup>183,184</sup>. This emphasis on electronic studies continued through the late 2000s and early 2010s with the insertion of the first ion channels<sup>185</sup> and pore forming antibiotics<sup>30</sup>. Another trend that arises from this analysis is that the type of analytical techniques available for use with DIBs guides the field. For example,

the use of fluorescence or spectroscopic detection methods has an inverse relationship with electronic studies during this period: a drop-off in the insertion of new pores and channels following 2011 seems to align with a relative explosion in publications using fluorescence for quantification, primarily to studying molecular diffusion across these model membranes<sup>41,186</sup>. Later in the 2010s, more exotic compounds such as membrane transport proteins<sup>42</sup> and mechanoselective ion channels<sup>187,188</sup> were inserted into DIBs, with both electrical and fluorescent methods used for quantification of molecular transport. Another trend seen since 2008 is the use of different lipids for DIB formation, such as cholesterol<sup>189,190</sup>. We believe interest in this area will continue to grow as a result of a greater focus on biomimeticity, which shows an increasing interest in these model membranes as artificial cells. It is notable that the proportion of publications using microfluidic techniques<sup>40,191,192</sup> for DIB formation has remained constant. We think that this is primarily due to difficulties associated with developing and using microfluidic technologies in laboratories that lack the facilities and equipment for doing so, an issue often referred to as the “chip-in-a-lab” problem.

In the first review of the field<sup>30</sup>, the authors predicted that DIBs would be used to facilitate precise membrane measurements to answer fundamental biophysical questions about membrane proteins, lipid diffusion and lipid flip-flop, and that asymmetric DIBs had not reached their full potential. In this perspective, we will discuss the progress that has taken place since then and highlight the major challenges facing the field, including the limitations associated with microfluidic methods for the formation of DIBs, how the lack of suitable detection techniques for quantifying molecular transport within DIBs is limiting their application in more diverse fields, and how to

Figure A.1: **A)** Schematic showing the formation of DIBs. Lipids self-assemble at the interface of aqueous droplets to form monolayers. Droplets are then brought into contact with each other manually or using microfluidic technologies to encourage bilayer formation between the droplets. DIBs can then be formed into networks in both two and three dimensions. **B)** Schematic showing the arrangement of lipids to form a liposome and **C)** a black lipid membrane. Triangles denote the solid support used to build the bilayer. Phospholipid size is exaggerated to show assembly. Microfluidic methods for the formation of DIBs usually rely on on-chip features such as **D)** rails<sup>55</sup> or **E)** pillars<sup>64</sup> to align the droplets and slowly bring them into contact with each other. In **D)**, three different droplets (labeled A, B and C with arrows showing the two DIBs formed between them) are brought together using this geometry. **F)** Cylindrical and conical shapes used to describe the packing characteristics of different types of lipids. Figure E reproduced under the terms of the Creative Commons license.<sup>66</sup>



increase the biomimetic nature of DIBs. We will also explore what the future holds for DIBs.

### **A.3 Designing and building DIBs as biomimetic model membranes**

The ultimate goal when developing model membranes is to build a fully biomimetic bilayer from the bottom up. Cell membranes are complex entities, and it is not always possible to determine how molecules interact with and pass through these membranes. Being able to design and build model membranes that mimic each facet of cell biology provides a versatile and modular tool to study *in vivo* processes. Hence, each component of the membrane, from the molecular composition to the membrane proteins, should mimic those found in nature, while also enabling bespoke model membranes to be created for a wide range of applications. Traditional model membrane systems can be broadly categorised into planar or curved. BLMs are the earliest example of planar model membranes<sup>17</sup>, but some of their inherent characteristics have limited widespread adoption of these systems. BLMs are short lived and unstable, which means that they are mostly used to study fast processes carried out by ion channels and pores<sup>193</sup>. Forming BLMs is also a particularly delicate process, requiring a high degree of skill that is not compatible with high throughput experimentation<sup>194</sup>. Because they are planar bilayers formed between aqueous wells, BLMs fail to capture features of cellular membranes such as membrane curvature, and the vastly different

ratio of cellular volume to bilayer surface area. Liposomes are the most commonly used curved model membranes and are relatively straightforward to make compared to BLMs, leading to their widespread adoption as model membranes for studying lipid interactions<sup>195</sup>. However, achieving consistency in terms of size and lipid distribution can be difficult, as can be modelling features of cellular membranes such as the asymmetric molecular composition of each of the monolayers that form the bilayer in cell membranes. DIBs represent a third category of model membranes, which have advantages associated with planar membranes, such as the ease of compartmentalisation of the fluid on each side of the membrane, and advantages associated with curved model membranes, such as the formation of asymmetric bilayers and consequential inducement of membrane curvature<sup>13</sup>.

Microfluidic technologies allow unprecedented control over how DIB systems are built and interrogated. Microfluidic technologies are designed to enable accurate control of fluids on the micron scale, for example to create aqueous droplets of volumes similar to the size of cells, which can then be used to build biomimetic DIBs. Over the last decade, around a third of publications have used microfluidic methods for DIB formation, highlighting a significant shift in the field since the first high-throughput method was published in 2010<sup>40</sup>. Microfluidic technologies have enabled the creation of artificial tissues-on-a-chip, where multiple DIBs are arranged into interconnected networks, by refining control over droplet and bilayer size and their precise arrangement in the network<sup>61,62,65,196</sup> and can hence be used for the measurement of passive molecular movement across the membranes<sup>41,64</sup>. These applications require the isolation of distinct chemical environments in separate droplets which is enabled by the

highly tunable nature of microfluidic platforms, and showcase properties of DIBs that are not possible with other types of model membranes.

There are several key designs of on-chip features that allow this level of control and are consistently used in the field. The introduction of meanders<sup>60</sup> allows time for lipids to self-assemble as monolayers on the droplet surface before DIB formation, bypassing the long equilibration times (minutes) required when using manual micromanipulators<sup>30</sup>. This means that whereas manual methods for DIB formation are usually limited to tens of DIBs, microfluidic methods can generate hundreds or even thousands of DIBs per minute<sup>40</sup>. Droplet trapping geometries such as pillars<sup>41</sup> and rails<sup>65</sup> are commonly used to guide droplets to exact locations and hence provide control over the exact composition of DIB networks (Figure A.1D and E). However, DIB formation techniques are far from homogeneous and more esoteric microfluidic DIB formation strategies include bilayers formed by solvent evaporation<sup>176</sup>, flow-guiding<sup>65</sup>, hydrodynamic traps<sup>61,164</sup>, “passive” droplet guidance that relies solely on on-chip architectural features<sup>55,64,191</sup>, and “active” droplet guidance which additionally requires the use of on-chip features such as valves to control droplets<sup>62</sup>.

From a molecular perspective, the design of the membrane fundamentally limits the type of assays that can be performed in the DIB, both from the perspective of the molecules used to form the bilayer and the oil phase used to support the amphiphilic molecules prior to DIB formation. So far, DIBs have largely been built using single synthetic phospholipids, mainly DPhPC and DOPC (1,2-dioleoyl-sn-glycero-3-phosphocholine) and are hence not very biomimetic. The few exceptions include

polymers<sup>59,197</sup>, and more biomimetic bespoke lipid formulations<sup>55,198</sup> and total lipid extracts<sup>45,121,198,199</sup>. Other components of cell membranes, including neutral lipids such as cholesterol and monoglycerides, have also been used along with phospholipids for DIB formation<sup>189,198,200–204</sup>. The chemical structure of phospholipids is a factor in membrane permeability, with both acyl chain and polar head group type influencing bilayer packing and permeability<sup>44</sup>. In biological systems, lipid packing depends partially on the relative space occupied by the head group and acyl chains<sup>127,205</sup> (Figure A.1F). Lipids with similarly sized head groups and acyl chains have an overall cylindrical shape and pack together as flat bilayers. Lipids with head groups that are much larger than the space occupied by the acyl chains form a cone shape that creates curvature when packing. Finally, lipids with small head groups are the opposite, where the cone is inverted because the head groups are much smaller than the splayed tails. These structural complexities create differences in molecular packing which are only recently beginning to be understood<sup>44</sup>. It is also important to note that bilayer formation in cells is not just dependent on self-assembly, but is also reliant on cellular machinery that is not currently present in these types of artificial cells.

From an energetic perspective, DIBs present a non-biomimetic system where the tail groups of the lipids are in a supportive oil phase, rather than in fully aqueous biological systems. This means that there needs to be an energetic advantage to forming a bilayer in a DIB<sup>54</sup> and this is dependent on the molecular composition used to form them. In fact, the length of the lipid tails has an effect on how likely the droplets are to adhere to each other and form a DIB<sup>206</sup>. Lipids available for use in building model membranes are either synthesised directly or extracted from natural sources, which



leads to differences in the molecular composition of the reagents. Synthetic lipids are formed from molecules with the same head groups and acyl chains, and usually have high degrees of purity. Naturally derived lipids have been extracted from a natural source (mostly egg or animal tissues) and purified to ensure that all molecules present in the sample have the same head group. However, the sample contains a range of acyl chains lengths and degrees and location of unsaturation. The most biomimetic lipid source are total lipid extracts, where all head groups (and hence acyl chains) from a natural source are extracted. Both of the naturally derived lipids may also include other molecules present in cell membranes, such as polyunsaturated fatty acids. The oil in which the aqueous droplets are formed also plays an important role in the energetic favourability of DIB formation, though this has been less studied. The oil must both support the self assembly of the monolayer covering the droplets by supporting the lipid tails and, as the DIB forms, be easily removed from the bilayer. Hexadecane in the most commonly used oil for DIB formation, though it is likely to stay in the membrane and hence cause unrealistically thick model membranes<sup>207,208</sup>. Squalene is likely to be excluded completely from the membrane<sup>209</sup> and is therefore a more attractive choice for biomimetic model membrane formation. Hence, the choice of the lipids (and of the supporting oil) used to form DIBs has a direct effect on the degree of biomimicry of the model membrane.

However, being able to make DIBs from either bespoke naturally derived lipid formulations or biomimetic total lipid extracts is a key step for DIBs to fulfil their potential as an elegant model for complex cell membranes. Controlled heating of the aqueous droplets has been shown to facilitate complete monolayer self-assembly and

encourage DIB formation<sup>55,121,198</sup>. We have also recently shown that the lipid-out method, where lipids are dosed in the oil phase, allows DIB formation at physiological temperatures with naturally derived lipids<sup>55</sup>, whereas when the same lipids are dosed in the aqueous phase (lipid-in) higher temperatures are required to enable DIB formation. Hence, temperature is another factor that can affect packing dynamics in DIBs by allowing the molecules to rearrange themselves to accommodate their neighbours<sup>44</sup>. Generally, the lipid-out method is slower to form a monolayer because of the high energy required for inverse micelles to form a monolayer due to tail-tail interactions. Repulsive interactions between micelles in the water phase favours monolayer formation when using the lipid-in method. However, this does not hold for naturally derived lipids, where heating is required to overcome this energetic barrier.

DIBs allow the interplay between the molecular components of membranes and their biological behaviour to be elucidated. Fundamental research into water permeability across DIBs provides insight into the role that key lipid types play in membrane permeability. DIBs built between two droplets containing a NaCl concentration gradient allowed the observation of osmotic transport of water across the membrane using microscopy<sup>200–202,210</sup> and Raman microspectroscopy<sup>211</sup>. By designing lipid formulations containing precise amounts of membrane components such as cholesterol<sup>200</sup>, cholesterol sulphate<sup>210</sup>, monoglycerides with varying acyl chain lengths and saturation levels<sup>200–202</sup> and asymmetric DIBs<sup>210</sup>, it is possible to isolate the effects these wide-ranging membrane properties have on water permeability. For example, increasing monoglyceride unsaturation is correlated with increasing water permeability across the DIB<sup>200–202</sup> and addition of cholesterol is correlated with decreasing

permeability<sup>200,202</sup>. This is because unsaturated lipids have a cis bond which allows for looser packing. Cholesterol itself actually sits inside the bilayer causing the lipid tails to agglomerate around it and hence packing becomes tighter making the membrane less permeable<sup>189</sup>. Increasing monoglyceride acyl chain length, which leads to creation of thicker bilayers, is also correlated with decreasing water permeability<sup>201</sup>. Addition of cholesterol sulphate to a DPhPC bilayer correlates with decreasing permeability, while addition of this molecule to only one leaflet of the DIB creates an intermediate condition<sup>210</sup>. In fact, DIBs have enabled the investigation of the effect that cholesterol has on the formation of lipid rafts, which are not readily visible in other systems<sup>204</sup>. It is exciting to see that the ease with which both symmetric and asymmetric DIBs can be formed from bespoke lipid formulations means that they are used to precisely quantify how molecular transport across membranes is affected by changes in lipid composition.

## **A.4 DIBs to quantify molecular kinetics**

DIBs represent a simple method to quantify molecular transport across an artificial bilayer because the droplets on either side of the bilayer serve as donor and acceptor compartments, with volumes small enough to enable detection at low concentrations and the potential to perform parallelised assays. This is one of the major advantages of DIBs when compared to other model membranes for chemical analysis. However, this has not been exploited to its full advantage and most research has been performed

using dyes such as fluorescein<sup>40,41,55,64</sup>, carboxyfluorescein<sup>212</sup>, calcein<sup>64,187</sup> and resorufin<sup>45,213</sup>. In fact, diffusion of fluorescein is regularly used in place of capacitance measurements<sup>37</sup> to verify that contacted droplets have formed a DIB, especially within microfluidic devices.

An interesting example shows the translocation of large molecules across a DIB with the horseradish peroxidase enzyme as a detector using the cell penetrating peptide Pep-1<sup>186</sup>. Translocation across the bilayer was verified by merging the acceptor droplet with a droplet of fluorogenic substrate, demonstrating the possible utility of this technique for droplet sized fluorescence assays. Furthermore, by treating multiple encapsulated DIBs as a reactor unit, it is possible to use these “multisomes” as self-contained chemical reactors for the synthesis of a fluorescent pyridinium reporter (Figure A.2)<sup>192</sup> or to mimic how cells process external chemical signals<sup>214</sup>. This type of *in-situ* modular processing opens the door to performing multi-step synthetic chemistry in biologically relevant environments, for example for the synthesis of drugs close to their membrane-bound targets and the study of membrane-bound signalling pathways. Since DIBs can be used to easily form asymmetric bilayers, it possible to use these model membranes to study the effect that membrane asymmetry has on molecular transport and hence the design of intracellular drug delivery methods<sup>215</sup>.

From a pharmacological perspective, early work showing the diffusion of caffeine in DIBs showed their potential to become an alternative to parallel artificial membrane permeability assays (PAMPA)<sup>41</sup>, which are a commercial *in vitro* platform used in drug discovery to predict the ability of drugs to cross cell membranes *in vivo*. There

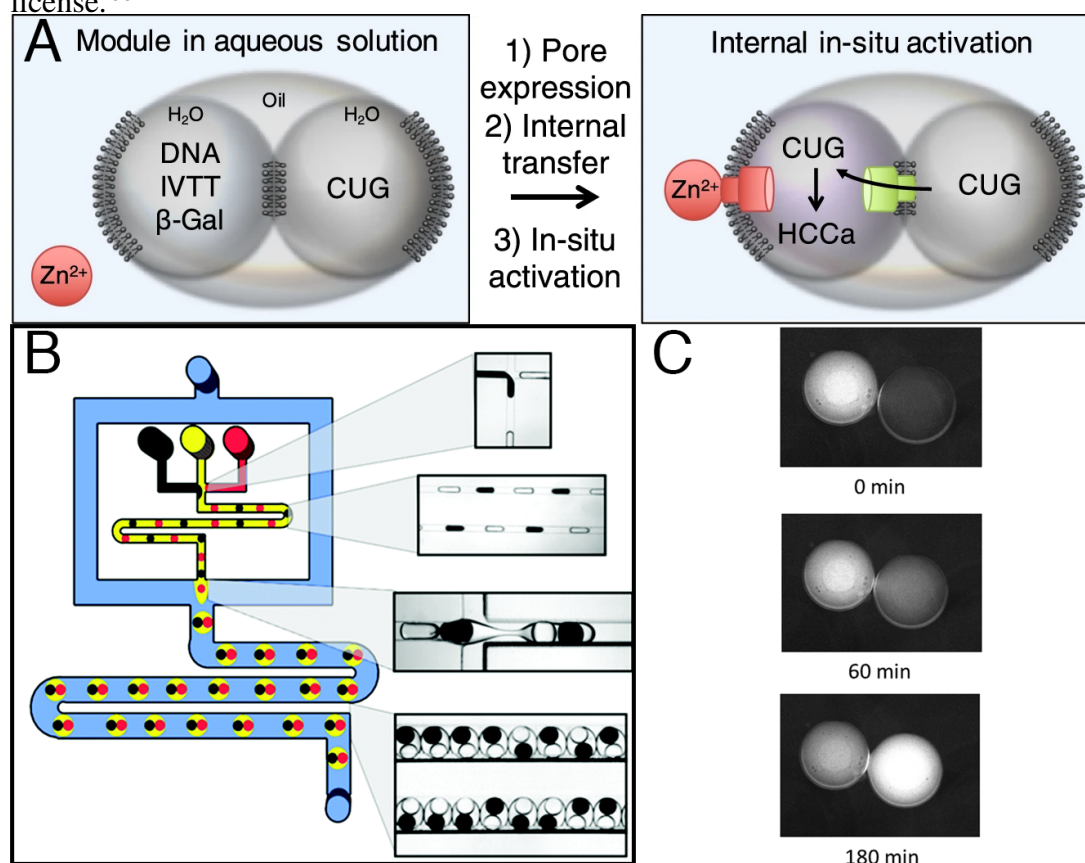
is no true model membrane in PAMPA, instead, a plastic filter placed in a well and infused with lipids is used to quantify molecular transport. This work is also interesting because it addresses another current limitation of DIB research, namely the overreliance on fluorescence microscopy for detection, and instead uses UV microspectroscopy to monitor molecular movement. We have recently demonstrated that DIBs more accurately predict apparent permeability than PAMPA for fluorescein absorption in rat intestinal cells<sup>55</sup>. Our DIBs were made using naturally derived lipids that mimicked the lipid composition of intestinal cells. This means that DIBs are potentially a more reliable indicator of passive drug permeability than the current state of the art commercial technique. We have also recently shown that DIBs can be used to model the breakdown in membrane asymmetry that occurs during cancer, and how this affects the transport of the chemotherapy agent doxorubicin, giving new insight into the mechanism of chemoresistance<sup>13</sup>. In a similar manner, DIBs have also been used to investigate the effect that the nonsteroidal anti-inflammatory drug (NSAID) ibuprofen has on the integrity of the membrane itself, showing that membrane permeability is increased when ibuprofen interacts with certain lipids in the membrane, but not when cholesterol is present<sup>216</sup>. These recent works illustrate the potential of DIBs to be used to study drug-membrane interactions to help understand the mechanisms behind drug *in vivo* behaviour.

## A.5 DIBs to study integral membrane proteins

Being structurally analogous to a cell membrane, DIBs provide a useful scaffold to study membrane proteins<sup>217</sup>. Since DIBs are more stable than other artificial membrane systems they provide an attractive platform for this kind of analysis. The first protein to be inserted into a DIB was  $\alpha$ -haemolysin<sup>37,38</sup>, a pore forming toxin from *Staphylococcus aureus*. Due to its relative ease of use, and ability to self insert in a membrane,  $\alpha$ -hemolysin has dominated the field perhaps to the detriment of more exciting biological entities. In the past decade many more proteins and peptides have been successfully reconstituted and inserted into DIBs using three main methods: self-insertion, reconstitution in liposomes before DIB formation, and *in vitro* transcription/translation (IVTT). Proteins can sometimes be self-inserted into membranes without any external influence through self-assembly under favourable conditions. Usually, however, proteins need to be reconstituted using detergents to solubilise them, which are then exchanged for lipids using dialysis. In IVTT, cellular machinery (ribosomes, DNA, amino acids etc.) is inserted into a droplet of the DIB to express the protein *in situ* directly into the bilayer.

Notable examples of protein insertion into DIBs include the incorporation of the eukaryotic hERG potassium channel and NMDA receptor in DIBs after expression in mammalian cells<sup>219</sup>. Electrical measurements of these, as well as endogenously expressed mammalian potassium channels, and prokaryotic KcsA were carried out with no purification. Since purification of membrane proteins is notoriously difficult<sup>220</sup>, bypassing this step greatly increases the accessibility of methods to study them. The

Figure A.2: **A)** Use of IVTT to insert a variant of  $\alpha$ -hemolysin into a multisome, allowing the precursor compound 3-carboxyumbelliferyl- $\beta$ -D-galactopyranoside (CUG) to diffuse through to the droplet containing  $\beta$ -galactosidase. This enzymatic reactor creates a fluorescent reporter<sup>218</sup>. **B)** Multisomes have been made in large quantities using microfluidic methods, creating several self-contained reaction vessels, also used in this work to create a fluorescent reporter<sup>192</sup>. **C)** IVTT has also been used for the expression of an ATP powered transporter protein from the major facilitator superfamily, shown here pumping the fluorescent sugar 4-methylumbelliferyl- $\beta$ -galactopyranoside<sup>42</sup>. Figures reproduced under the terms of the Creative Commons license.<sup>66</sup>



incorporation of ion channels into DIBs suggests that DIBs may also be used as an alternative to patch clamp experiments. The patch clamp technique is used to compartmentalise sections of live cells such that transport across ion channels can be measured while in their natural environment. The compartmentalisation inherent in DIBs means that these experiments can happen in model membranes that mimic the natural environment much easier. The mechanoselective MscL channel, a stretch activated ion channel found in *E. coli*, has been incorporated into DIBs and activated using the compound 2-(trimethylammonium)ethyl methane thiosulphonate bromide<sup>187</sup>. Further work has confirmed that MscL proteins incorporated into DIBs retain their stretch responsive properties by taking electrical measurements while mechanically stimulating the DIB in which MscL was incorporated<sup>221</sup>. It is interesting to see again that being able to create asymmetric DIBs provides more information on the behaviour of a biological system. In this case, membrane asymmetry allows control over the activation state of MscL, showing that the lipoidal composition of the membrane can be leveraged to generate physical forces to pull open the channel<sup>222</sup>. More recently, the spontaneous insertion of the human chloride channel CLIC1 has been shown in a DIB, and quantification of chloride flux using the quenching of a chloride responsive fluorescent dye<sup>190</sup>. This work is particularly interesting due to their unique approach to forming DIB pairs using a microfluidic device that created a multiplexed array of several replicates.

While most proteins successfully inserted into DIBs are pores or ion channels, so far only two examples of active transport across a DIB have been demonstrated through the insertion of the *E. coli* lactose permease transporter (LacY) (Figure A.2)<sup>42</sup>



and bacteriorhodopsin<sup>38,223</sup>. The uphill transport of a fluorescent sugar using LacY was shown and through manipulation of the lipid composition, the authors were able to vary the activity level of LacY. In this case, exchanging DOPC with DOPE (1,2-dioleoyl-sn-glycero-3-phosphoethanolamine) increased the lateral pressure in the tail group region of the membrane, which led to a change in the rate of molecular transport by causing a change in the energy of the conformational change in the protein. LacY was successfully incorporated in a DIB using both reconstitution in liposomes after expression in *E. coli*, and with IVTT. Bacteriorhodopsin is a light-driven proton pump that has been inserted into DIBs to use them as “bio-pixels” to detect images as the proton pumps are activated by light and produce a current. The aim of this work was to show the potential of these DIBs to be used to stimulate real cells such as neurons.

Since the droplet on either side of a DIB can be used to mimic a cell<sup>55</sup>, linking multiple DIBs together in a network can form an artificial tissue where it is possible to control the packing of each artificial cell in the tissue<sup>224–226</sup>. In these cases proteins are not only inserted into DIBs to enable their behaviour to be studied, but are used as well to demonstrate fundamental characteristics of the artificial tissues, such as intercellular communication<sup>227</sup> and collective properties<sup>228</sup>. Recent work has shown that DIBs created in this manner but encapsulated in a non-oil surrounding material (in this case a hydrogel) for stability can also be used to mimic communication between organelles in a cell through the bacterial pore cytolysin A<sup>229</sup>. This surrounding material can also be deformed, causing controllable changes in the membrane properties in these three dimensional networks<sup>230</sup>.

However no human proteins have so far been inserted into DIBs. This is likely because it is not straightforward to create DIBs (or any type of model membranes) that are biomimetic enough to support the correct insertion of complex human proteins and ensure their functionality<sup>231</sup>. A good first step in this direction will be the creation of DIBs that mimic the native environment of the proteins, both in terms of the molecular composition of the membrane and in terms of creating favourable experimental conditions for the insertion of proteins. With screening of drugs against transporter libraries forming an important and costly part of early drug discovery<sup>6</sup>, successfully inserting pharmacologically relevant transporters into DIBs will mark a turning point in the use of DIBs as biomimetic model membranes and we predict that interest in their use as a tool to enable cheaper and faster early drug discovery by supplementing or replacing cell cultures will be high.

## **A.6 DIBs as scaffolds for electrophysiological measurements**

Electrochemical gradients provide the driving force for cellular processes such as nerve conduction and respiration. Studying the electrophysiological characteristics of lipid membranes is essential to fully understand this aspect of cellular physiology. The electrical properties of DIBs have been measured extensively, with capacitance measurements and measurement of current through  $\alpha$ -hemolysin forming the bulk of these measurements. Fundamental research into the voltage-current relationship of DPhPC

membranes and the effect of  $\alpha$ -hemolysin and of alamethicin on this relationship has shown that  $\alpha$ -hemolysin decreases membrane resistance through formation of pores, and alamethicin causes a voltage dependant increase in conductance<sup>177</sup>. The dependence of bilayer capacitance on bilayer area has been exploited to accurately measure the specific capacitance of DPhPC based DIBs in hexadecane<sup>207,232</sup>, mixtures of hexadecane, silicone oil and decane<sup>203</sup> and tetradecane<sup>189</sup>. Capacitance measurements of planar bilayers can be used to accurately quantify membrane parameters to ensure biological similarity. For example, to show the formation of the bilayer through exclusion of the oil phase<sup>209</sup> and to quantify membrane asymmetry<sup>208</sup>. While electrodes used for these types of measurements in DIBs are frequently Ag/AgCl electrodes inserted into the droplets themselves, it has also been shown that electrodes that sit at the surface of the droplets can be used to induce or measure flow of ions between DIBs<sup>233</sup>. These electrodes are covered with a monolayer of lipids and form another bilayer with the monolayer covered droplet. This type of measurements has been developed for other model membrane systems in ways that could also be integrated with DIBs. Interesting work to create a membrane containing a single peptide pore and measure current across it has potential for high-throughput screening using gold<sup>234</sup>, Ag/AgCl<sup>235</sup> or hydrogel electrodes<sup>236</sup>. The advantage of external electrodes is that they can be easily integrated into microfluidic devices for analysis of molecular transport across DIBs, potentially expanding the types of analyses that can be performed in DIBs, which is one of the current main limitations in the field.

Engineered networks of DIBs had already been shown to exhibit interesting emergent properties prior to the first review of the field, such as functioning as batteries or

light sensors<sup>38</sup>. Since then, networks of DIBs have been shown to be capable of functioning as diodes when treated with modified, heptameric  $\alpha$ -hemolysin<sup>228</sup>. Droplets containing these modified  $\alpha$ -hemolysin heptamers were arranged to create a half wave rectifier, a current limiter, and even a full wave bridge rectifier. Because DIBs can easily be built into networks, more complex signal processing may be carried out with systems like this, for example to perform computing, or to serve as an interface between electronics and tissue. A recent review of the field further expands these ideas by elegantly describing the potential of DIBs from an engineering and materials science perspective<sup>237</sup>.

From a more biomimetic perspective, bilayer capacitance and air flow-induced current measurements have been used to model the mechanotransduction properties of animal sensory hairs via DIBs made from DPhPC as model hair cells<sup>197,238,239</sup>. In this work, an artificial hair was inserted into one of the droplets forming the DIB, allowing the effect of hair movement on the membrane to be investigated. This integration of macro and micro biological entities serves as a new kind of electromechanical sensor for small air movements and sound. DIBs made from DPhPC and DOPC have also been used as models for biophysical kinetic measurements by monitoring changes in transmembrane potential of asymmetric DIBs before and after insertion of alamethicin. It is not easy to form asymmetric bilayers using other types of model membranes, and few systems even exist that enable these types of studies. Being able to easily model this asymmetry using DIBs revealed new insights into how this pore interacts with the membrane by inducing lipid “flip-flop”. Hence, DIBs allowed the elucidation of the behaviour of the antibiotic in the membrane<sup>164</sup>. Prior work shows

the use of a combination of interfacial tension (IFT) measurements and computational analysis to investigate the effects of lipid adsorption kinetics on phospholipid monolayer self-assembly at an oil-water interface<sup>54</sup>. The quantification of the success rate of DIB formation as well as resistance and rupture potential of the DIBs successfully formed using each of the aforementioned techniques showed a significant difference between DPhPC and the unsaturated lipid DOPC. Even when the IFT value determined to be optimal for DIB formation was attained, DOPC monolayers required a longer incubation time than DPhPC to form DIBs. Studying the factors affecting the kinetics of monolayer formation not only provides explanations for success rates of DIB formation in future work, but also provides useful information for processes involving lipid emulsion formation. The authors apply these findings to use evaporation to cause monolayer compression to be able to form DIBs using unsaturated phospholipids<sup>240</sup>, with more recent work using smaller droplets to more easily form DIBs from unsaturated lipids<sup>216,236,241</sup>. The mechanics of membrane formation in DIBs requires further investigation. This is especially true since DIBs made from more biomimetic lipids and more complex lipid mixtures are needed to enable them to become the go-to model membrane system.

## **A.7 The future and potential of DIBs**

The last decade has shown that DIBs are versatile and biomimetic model bilayers for applications ranging from the study of protein transport to artificial cells. The ease

of formation of DIBs using manual or microfluidic methods means that they have the potential to become a widely used model membrane system. However, it is clear that they have yet to achieve their full potential. We believe that advances in the following research areas will be key drivers in terms of the development and application of these systems in coming years.

**Fundamental bilayer behaviour.** There is a lack of fundamental chemical insight into the kinetics and mechanics of monolayer and DIB formation. For example, we need a deeper understanding of the effect that the method of lipid delivery (lipid-in or lipid-out) has on the kinetics of DIB formation, what the kinetics are for lipid domain formation in DIBs and whether this enables the modeling of domain formation in real cells, how lipid flip-flop and lateral diffusion within the bilayer occur and how this affects molecular permeability, and how small molecule diffusion through bilayers is affected by differing lipid (and oil) composition. The incorporation of fluorescently tagged lipids into DIBs may be a key component of this research, as will the use of techniques, both experimental and computational, more widely used by the membrane biophysics community to study the structure and function of these systems. Understanding these fundamental biophysical processes will enable more complex DIBs to be formed, and will enable comparison of the model membrane with their biological comparators.

**Biomimetic artificial cells.** Cells are complex entities. DIBs can function as bespoke artificial cells that can be built from the bottom up to enable the quantification of the behaviour of each component of the cell membrane. To function as artificial cells

for the understanding of chemical interactions in the cell membrane, we must expand the library of lipids and biomimetic lipid mixtures that can be used for DIB formation. This should include all types of molecules found in cell membranes, such as glycolipids and peripheral proteins. Making DIBs more biomimetic also necessitates the development of strategies to reproducibly generate asymmetric DIBs and to insert a range of human membrane proteins into DIBs. Creating more complex DIB-linked droplet networks will enable the investigation of larger scale cell communication and molecular transport. Progress on these fronts will allow DIBs to be developed specifically as a screening tool for early-stage drug candidate permeability and activity.

**Technological advances.** Microfluidic technologies have enabled a host of new advances in the field. However, most microfluidic platforms are made using polydimethylsiloxane (PDMS), a choice of material that both limits assay length as the droplets evaporate over short time-frames and limits the commercialisation of microfluidic methods for DIB formation because other materials are used for the mass manufacture of microfluidic devices. Microfluidic devices made from materials such as polymers suitable for injection-moulding or hot embossing will ensure that they are not simply a gimmick used by experts in academic laboratories. More high-throughput methods for DIB formation would enable rapid screening of drugs in DIBs for potentially dangerous interactions with channels and pore proteins. To increase the biomimetic nature of DIBs, microfluidic technologies that enable even smaller DIBs to be formed would allow more cell types to be modelled. Most fundamentally, the field would benefit from a streamlined strategy for the design of microfluidic platforms for DIB formation both in specialist and non-specialist laboratories, and from

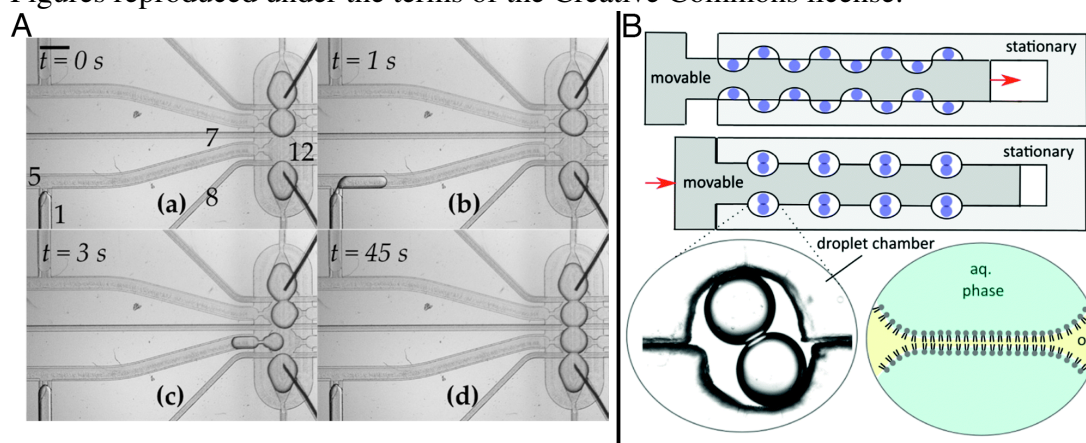
better integration of a variety of detection methods into these microfluidic platforms. For example, we have recently developed plug-and-play microfluidic platforms for the creation of droplets within droplets (multiple emulsions) that could be used for DIB formation<sup>242</sup>. Major impact in this area would be provided by a commercially available 3D printer capable of printing 3D networks of DIBs of different compositions onto surfaces with integrated electrodes or sensors for detection. Techniques such as these would enable these technologies to be used in laboratories with no microfluidic expertise.

**Detection methods.** One of the greatest barriers to the widespread adoption of DIBs as model membranes for the quantification of molecular behaviour is the reliance on fluorescence microscopy. This is particularly true for microfluidic methods of forming DIBs, since removing droplets from a microfluidic device for analysis is a nontrivial task. There is a need for new measurement techniques that allow the quantification of molecular transport on-chip (and off-chip) of a wider range of molecules. Types of molecules it would be interesting to detect in DIBs include those that enter or exit cells and organelles, such as drugs, cell signalling molecules, and cellular nutrients, or more complex entities that enter cells using other mechanisms, such as viruses. As we mentioned at the start of this article, the field has changed based on the types of analytical techniques available for detection in DIBs. Recent exciting work shows the integration of microfluidic platforms for the formation of DIBs with off-chip label-free analysis using liquid chromatography–mass spectrometry<sup>43</sup>. Older, and in our opinion underutilised, work with high potential for drug detection includes the use of UV-vis spectroscopy<sup>41</sup>. It would be exciting to see further work with these detec-



tion techniques, but also to see the integration of simple colorimetric assays, or more complex biochemical assays such as enzyme-linked immunosorbent assays (ELISA) into DIBs. New detection methods can also be based on the development of universal molecular recognition agents or through the development of on-chip sensors.

Figure A.3: **A)** An automated microfluidic platform that uses electronic control of valves to assemble and disassemble networks of DIBs on demand<sup>63</sup>. Complex experiments involving DIBs may potentially be done using such a system to increase throughput. **B)** A machined polycarbonate device for assembly of many DIB pairs on demand<sup>243</sup>. With multiplexed arrays of DIBs, single bilayer experiments may be carried out in replicate much like traditional macroscopic experiments in well plates. Figures reproduced under the terms of the Creative Commons license.<sup>66</sup>



Looking to the future, we believe that these advances will allow DIBs to be used for a host of new applications. By exploiting the electrical properties of engineered DIB networks, we might be able to assemble more complex structures such as logic gates that function as tuneable biosensors. Through advances in microfluidic technologies we could build interconnected, three dimensional networks of DIBs to create new biomaterials for application in the medicinal sciences. We can also imagine a future that includes automated synthesis and testing platforms for drug discovery (Figure A.3),

where combinatorial synthesis of drugs occurs in droplets which are then brought together to form DIBs to test molecular uptake through bespoke artificial cell membranes containing different types of lipids and transporter proteins. We look forward to looking back next decade to see whether DIBs have achieved their full potential.

## **A.8 Funding**

KSE is a Canada Research Chair and a Michael Smith Foundation for Health Research Scholar in partnership with the Pacific Alzheimer Research Foundation and receives funding from both. EBS and JLK are funded through KSE's Natural Sciences and Engineering Research Council of Canada (NSERC) Discovery grant.

## **Appendix B**

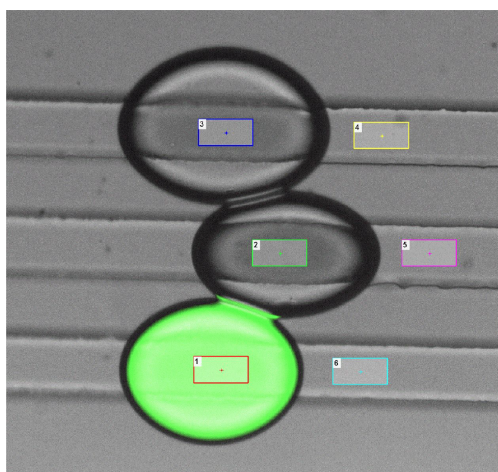
### **Electronic Supplementary**

### **Information: A bespoke microfluidic pharmacokinetic compartment model for drug absorption using artificial cell membranes**

Included in this appendix is the electronic supplementary information (ESI) for the work shown in Chapter 4, originally published in *Lab on a Chip* under the title: *A bespoke microfluidic pharmacokinetic compartment model for drug absorption using artificial cell membranes*.<sup>55</sup> My co-author Jaime Korner and I contributed equally to

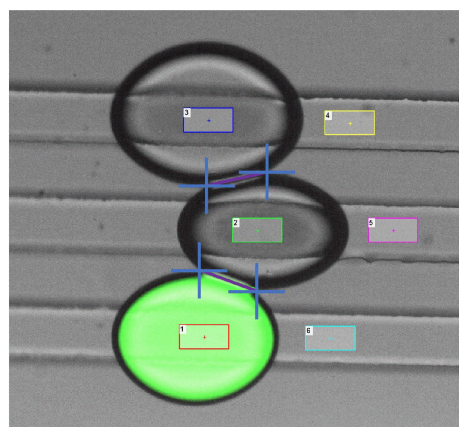
the writing of this ESI. There are video files associated with this ESI, which can be downloaded at: <https://www.rsc.org/suppdata/d0/lc/d0lc00263a/d0lc00263a1.zip>

## B.1 Fluorescence measurements and data normalisation



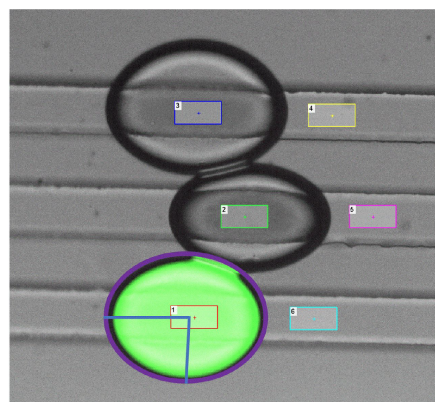
		Intensity (a.u.)						Background-Corrected Intensity (a.u.)			
Frame Number	Time (h:m:s)	Droplet A	Droplet B	Droplet C	A Background	B Background	C Background	Time (s)	Droplet A	Droplet B	Droplet C
1	00:00.4	49398.18	7157.96	6388.00	3346.52	3280.43	3244.00	0	46051.66	3877.53	3144.00
2	00:10.5	47625.79	8969.97	6422.77	3340.18	3275.58	3229.18	11	44285.61	5694.39	3193.59
3	00:20.5	45771.15	11060.22	6450.77	3345.15	3276.74	3227.89	21	42426.00	7783.48	3222.88
4	00:30.5	43717.29	13354.58	6473.10	3349.04	3278.36	3227.09	31	40368.25	10076.22	3246.01
5	00:40.5	41398.91	15870.70	6515.75	3358.16	3283.73	3234.70	41	38040.75	12586.97	3281.05

Figure B.1: **Fluorescence intensity measurements.** Regions of interest (ROIs) were drawn manually in the centre of each droplet (shown as coloured squares in the image above), allowing for the time-based measurement of fluorescence intensity using NIS Elements AR. Measurements based on ROIs were also taken in the channels near the droplets to determine the background intensity, which was subsequently subtracted from the sample intensities. Representative raw and treated data are shown in the tables.



Time (s)	Frame Number	Diameter ( $\mu\text{m}$ )	Area ( $\mu\text{m}^2$ )
0	1	53.85	2277.48
10	2	65.50	2829.29
20	3	70.75	3056.31
30	4	78.03	3370.45
40	5	87.42	3776.31

Figure B.2: **Artificial cell membrane surface area calculations.** Artificial cell membrane surface area was calculated by approximating droplet interface bilayers (DIBs) as ellipses, the diameters of which were measured using NIS Elements AR as shown above (lines between droplets defined between crosses; enlarged to show detail). This diameter and the depth of the channel (measured with a DekTak profilometer to be  $55 \pm 2 \mu\text{m}$ ) were used to calculate the artificial cell membrane surface area. Representative raw and treated data are shown in the table.



Time (s)	Axis A ( $\mu\text{m}$ )	Axis B ( $\mu\text{m}$ )	Volume ( $\mu\text{m}^3$ )
0	88.05	64.97	658966.79
300	85.25	73.12	718045.35
600	80.97	71.80	669683.94
900	79.81	69.16	635819.14
1200	78.94	67.67	615339.23

Figure B.3: **Droplet volume calculations.** Droplet volume was calculated by approximating droplets as ellipsoids, the semiaxes of which were measured using NIS Elements AR as shown above in the fluorescent droplet (lines from the centre of the droplet to the edges; enlarged to show detail). The semiaxes and the depth of the channel (measured with a DekTak profilometer to be  $55 \pm 2 \mu\text{m}$ ) were used to calculate the droplet volume. Representative raw and treated data are shown in the table.

## B.2 Calibration curves

Calibration curves were generated by first creating a dilution series of  $100 \mu\text{M}$ ,  $50 \mu\text{M}$ ,  $25 \mu\text{M}$ ,  $10 \mu\text{M}$ ,  $5 \mu\text{M}$  and  $1 \mu\text{M}$  fluorescein in all buffer solutions detailed in the paper. These buffers were pumped onto a chip, and the fluorescence intensity of droplets in

the main chamber was measured in the same way as for the intensity measurements described in the paper. Background was subtracted from all intensity measurements and linear fit generated in OriginPro 2019b. Each measurement was performed in triplicate and all values are shown in the graphs below.

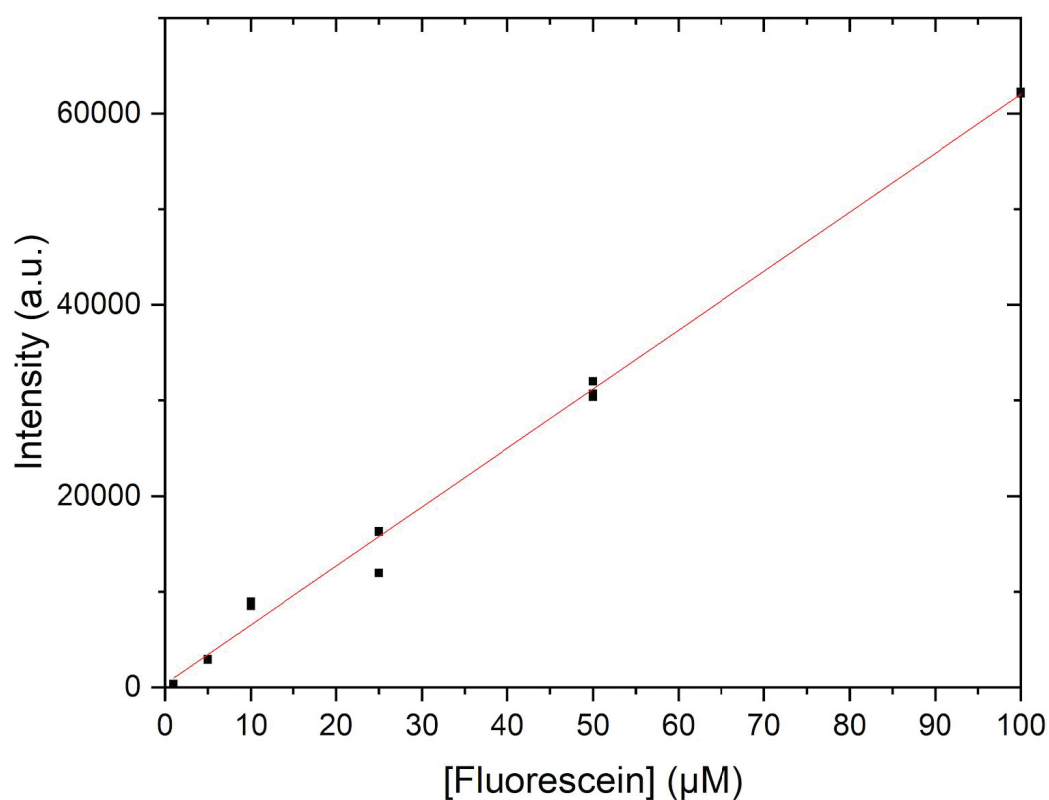


Figure B.4: **Calibration curve for fluorescein in the intestinal space compartment buffer.** Fit  $y = a + bx$ , where  $a = 393.23729 \pm 465.43736$  and  $b = 616.27152 \pm 9.90404$ .  $R^2 = 0.99588$ .



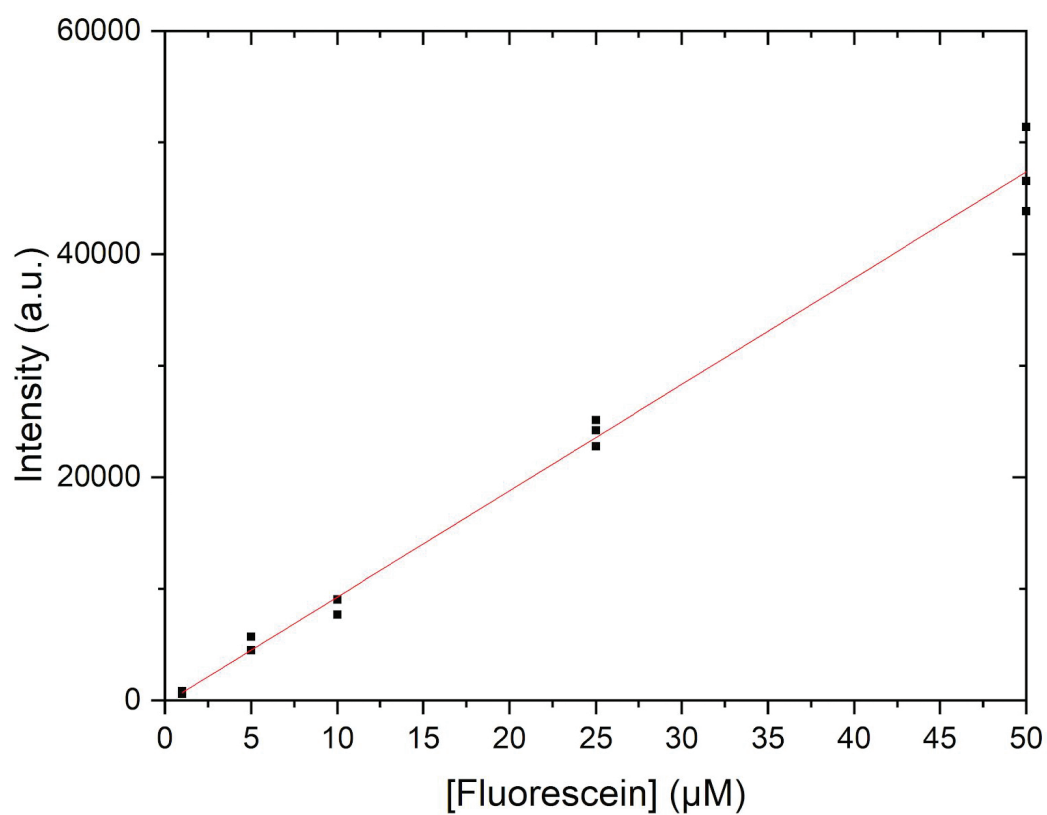


Figure B.5: **Calibration curve for fluorescein in the enterocyte compartment buffer.** Fit  $y = a + bx$ , where  $a = -229.04392 \pm 620.96026$  and  $b = 952.02902 \pm 24.35232$ .  $R^2 = 0.99157$ .  $100\text{ }\mu\text{M}$  data not included due to saturation of the detector.

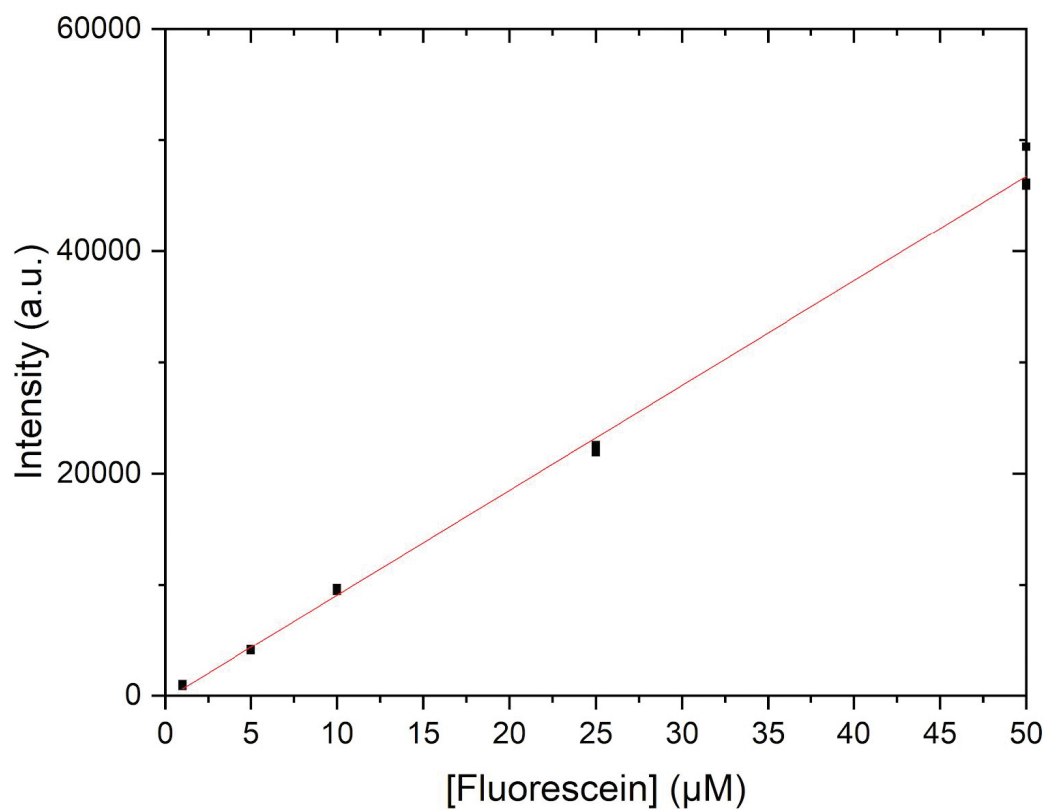


Figure B.6: **Calibration curve for fluorescein in the blood compartment buffer.**

Fit  $y = a + bx$ , where  $a = -308.81683 \pm 360.559$  and  $b = 941.38738 \pm 14.14011$ .  $R^2 = 0.99708$ . 100 μM data not included due to saturation of the detector.

### B.3 Control experiments

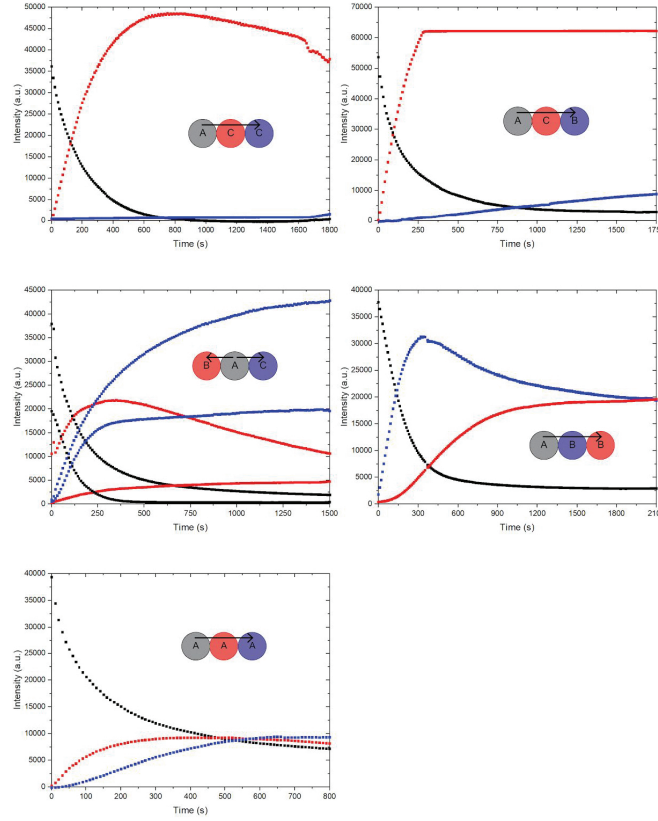


Figure B.7: **Control experiments.** Graphed data for each of the control experiments detailed in the paper. The configuration of the droplet triplets is shown as a diagram, where the colour corresponds to the data, and A corresponds to the intestinal space compartment, B corresponds to the enterocyte compartment and C corresponds to the blood compartment. The direction of fluorophore diffusion in each triplet is shown with arrows.

## B.4 Heating platform

The heating platform used to maintain the on-chip assays at a physiological temperature of 37 °C was designed to fit into the stage of Nikon Ti2-E and Ti2-U inverted microscopes, and was conceptually based on a platform previously used by us.<sup>244</sup> The heating platform is made of brass and uses resistive heaters and a proportional-integral-derivative (PID) controller to maintain programmed temperatures. The brass platform base was machined to include a viewing aperture (25.4 mm by 12.7 mm), allowing for consistent heating and visualisation of the microfluidic devices. Brass was used since it is resistant to corrosion and has low thermal conductivity. A lid was constructed from acrylic glass after initial tests showed that temperature measurements of the heating platform were not stable due to overhead draft from the laboratory ventilation system. The lid has a viewing port with the same dimensions as the mantle viewing port. Figure B.8 shows a scale three-dimensional drawing. The PID controller uses a PID control system to maintain a setpoint temperature on the mantle. The mantle uses 3 inch by 1 inch resistive heating foils that output 5 W/sq. in. of heat (35475K442, 28 V AC, McMaster). The foils are connected to a step down transformer (Hammond Manufacturing) which is connected to the output of a PID controller (CSI32K-C24, Omega Engineering). A type K surface thermocouple is used by the PID controller to monitor the temperature ( $\pm 0.4$  °C accuracy, SA3-K Fast Response Self Adhesive Thermocouple, Omega Engineering). Fridge magnets were used to clamp the glass slide containing the microfluidic device to the surface of the heating platform.

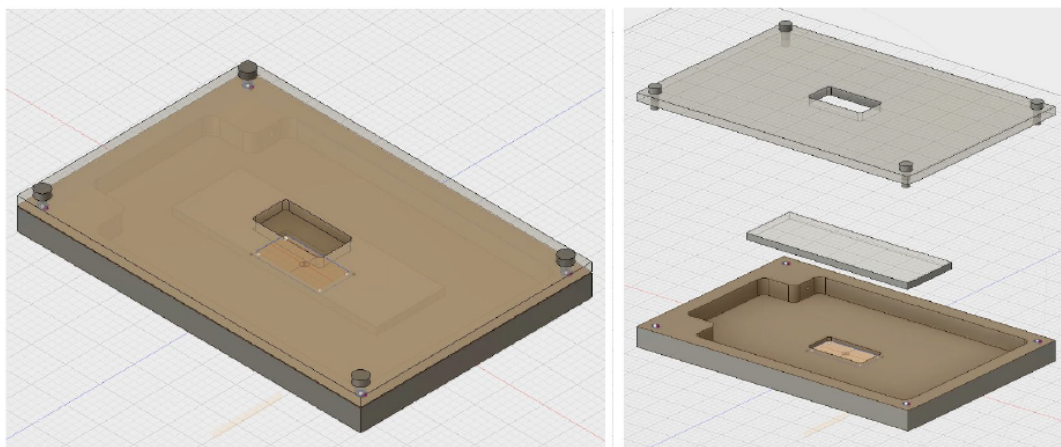


Figure B.8: **Three-dimensional constructed (left) and exploded (right) view of the heating platform.** The middle piece in the exploded view denotes a microfluidic device. The heating mantle itself is shown in brown and is constructed in brass. The lid is shown as clear since it is constructed in acrylic glass. Images are to scale.

The heating platform was calibrated using an ice water bath to determine whether the surface thermocouple was in good working condition. This was done by submerging the probe in ice water and leaving it for 10 min to stabilise. After 10 min the measured value of the ice water on the controller was 0 °C for the surface thermocouple. Since the heating foils do not cover the entire surface of the mantle, the platform was also heated to 37 °C and 50 °C and observed with a thermal camera (FLIR) to determine the temperature variability on the surface of the heating platform. Figure B.9 shows that the temperature variability is low.

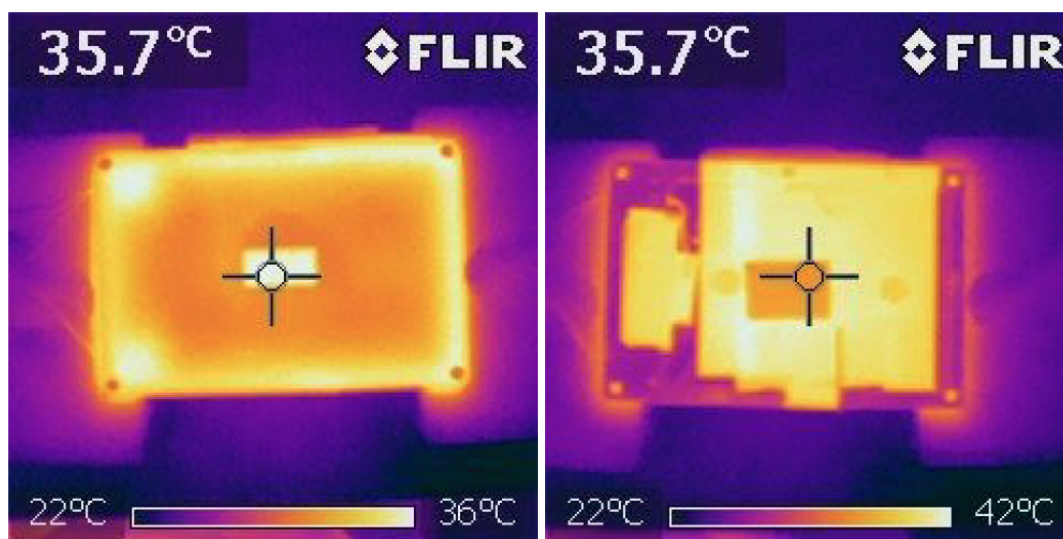


Figure B.9: **Thermal camera images of the heating platform containing a microfluidic device both when the platform is covered (left) and uncovered (right).** The heating platform was heated to 37 °C and the images show relative temperature readings between 22 °C and 36 °C as a colour scale. The lack of colour variation indicates that there is consistent temperature on the heating platform and on the microfluidic device.

The heating period of the mantle was determined by programming the mantle to heat and log temperature readings over the course of 30 min at 5 s intervals. The mantle was set to heat up to 30 °C, 37 °C and 50 °C and Figure B.10 shows the temperature readings we measured. The elapsed time before the readings stabilised (deviation of  $\pm 0.1$  °C) was 900 s, or approximately 15 min, of heating. All experiments in the paper were performed after temperature stabilisation of the heating platform.

## Heating Stability Measurements for 30C, 37C, and 50C

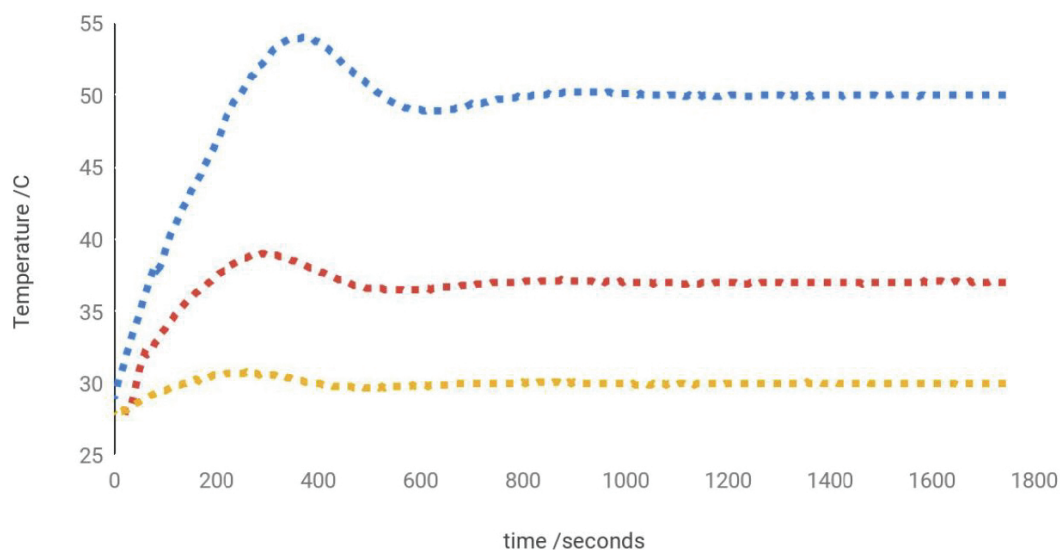


Figure B.10: **Heating platform temperature readings.** Taken every 5 s over 30 min after setting the temperature to 30 °C (yellow data), 37 °C (red data), and 50 °C (blue data). PID control parameters are  $P = 10$ ,  $I = 45$ ,  $D = 0$ , cycle time = 2 s and damping factor = 2.

## B.5 Video of device operation

File name: Device in Operation.mp4

Example of flow stoppage and droplet triplet selection using the OB1 pressure pump. Squalene is the carrier phase, and the content of the droplets is  $10 \text{ mg mL}^{-1}$  DPhPC in aqueous buffer (10 mM HEPES, pH = 7.6, 200 mM KCl). This video was

collected at room temperature with 180 mbar of pressure on the oil inlet and 140 mbar of pressure on each of the aqueous inlets. The video was captured at 30 fps with a Phantom V710L camera on a Nikon Eclipse Ti2-U inverted microscope.



# **Appendix C**

## **Electronic Supplementary**

### **Information: Biomimetic artificial cells to model the effect of membrane asymmetry on chemoresistance**

Included in this appendix is the electronic supplementary information (ESI) for the work shown in Chapter 5, originally published in Chemical Communications under the title: *Biomimetic artificial cells to model the effect of membrane asymmetry on chemoresistance*.<sup>13</sup>

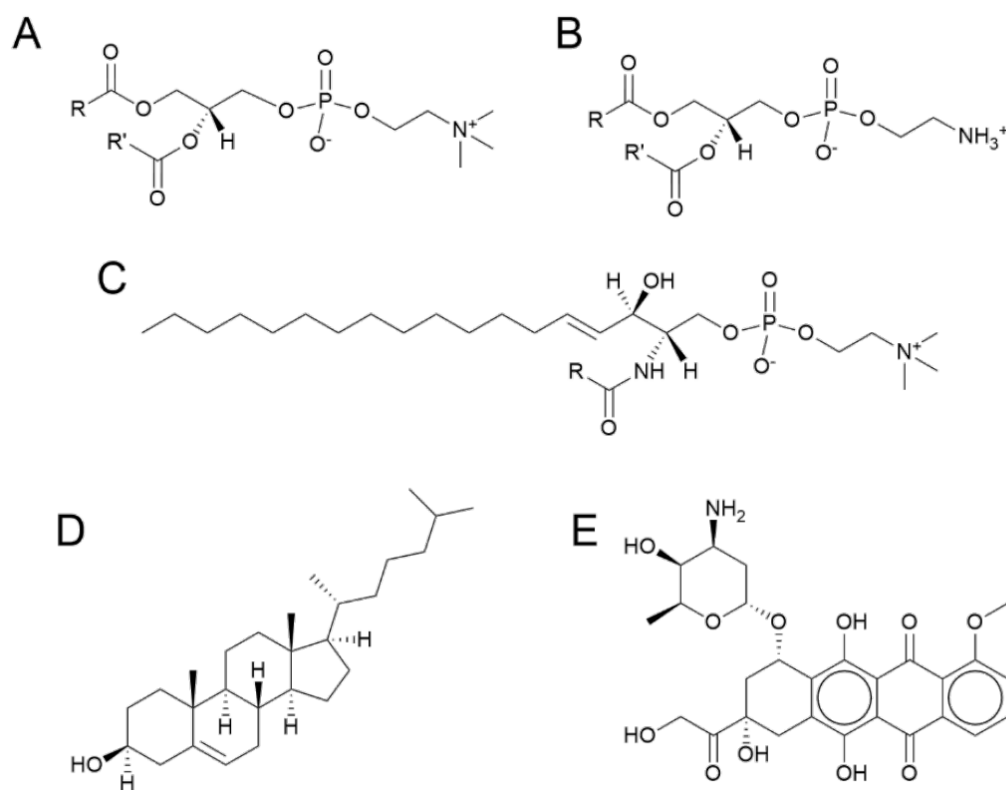


Figure C.1: **Chemical structures of compounds used.** General structures are shown for phospholipids, with **A)** being PC, **B)** being PE, and **C)** being SM. All of the phospholipids used are naturally derived, meaning that a mixture of several lipid chain lengths are present and substituted at R and R'. **D)** Structure for cholesterol, which is found between the lipid tails in biological membranes and enhances bilayer rigidity **E)** Structure for doxorubicin, a chemotherapy drug.

Table C.1: **Detailed compositions of lipid formulations.** The table shows the exact concentrations of lipids for each leaflet in asymmetric, blend and symmetric DIBs.

Bilayer type	Lipid	Outer leaflet ( $\mu\text{g/mL}$ )	Inner leaflet ( $\mu\text{g/mL}$ )
<b>Asymmetric</b>	<b>PC</b>	2015	830
	<b>PE</b>	830	2015
	<b>SM</b>	240	0
	<b>CHOL</b>	210	210
<b>Blend</b>	<b>PC</b>	1719	1126
	<b>PE</b>	1126	1719
	<b>SM</b>	180	60
	<b>CHOL</b>	210	210
<b>Symmetric</b>	<b>PC</b>	1423	
	<b>PE</b>	1423	
	<b>SM</b>	120	
	<b>CHOL</b>	210	

## C.1 Materials and methods

Egg 1- $\alpha$ -phosphatidylcholine (PC, >99%) and egg sphingomyelin (SM, >99%) were purchased from Avanti Polar Lipids. Egg 1- $\alpha$ -phosphatidylethanolamine (PE) was purchased as a reference standard from European Pharmacopoeia. Cholesterol (CHOL, Sigma grade), 4-(2-hydroxyethyl)-1-piperazineethane sulfonic acid (HEPES, BioPerformance certified grade) and KCl (molecular biology grade) were purchased from Sigma. Doxorubicin HCl (>95.0%) was purchased from TCI America. Aqueous buffer consisted of HEPES (10 mM, pH = 7.4) and KCl (140 mM). To insert DOX into the aqueous droplets, first a 10 mM solution of DOX was prepared by dissolving the doxorubicin HCl in dimethylformamide (DMF). Prior to each experiment, solutions were placed in a vacuum desiccator overnight to remove the DMF, and subsequently reconstituted in buffer at a concentration of 1 mM.

## C.2 Droplet and bilayer size measurements

Relative curvature, bilayer size, and droplet volume were all determined manually in NIS Elements. This process is time consuming, and this in combination with the field of view of the microscope enabling only one droplet pair to be observed at one time, means that throughput of data analysis is lower than the throughput of DIB formation allowed by the microfluidic platform. Automation of image analysis would considerably speed up this process and enable collection of larger data sets.

Channel height ( $h_{\text{channel}}$ ,  $53 \pm 1 \mu\text{m}$ ) was determined by analysing the SU-8 on silicon master wafer with a profilometer (Dektak XT).

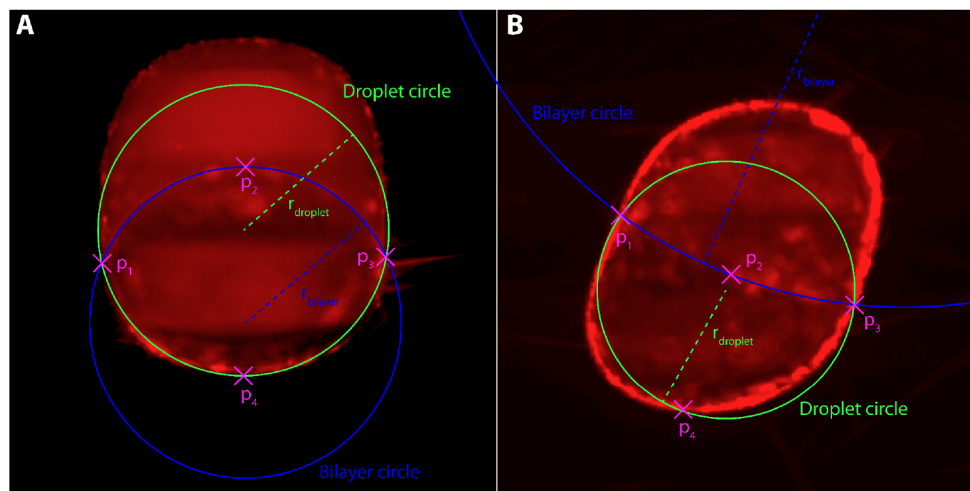
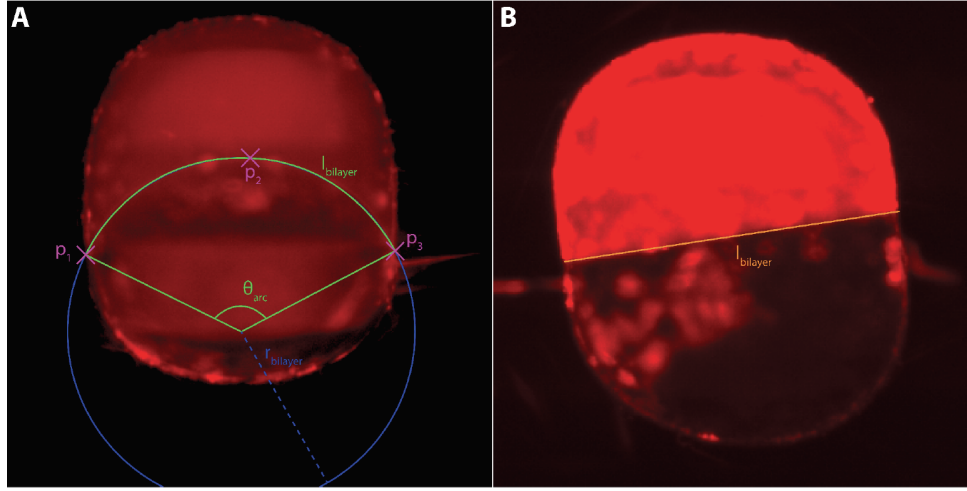


Figure C.2: **Relative curvature measurements.** For the bilayer radius (blue,  $r_{\text{bilayer}}$ ), a circle intersecting 3 points ( $p_1$ ,  $p_2$ ,  $p_3$ ) was drawn, corresponding to the left edge ( $p_1$ ), center ( $p_2$ ), and right edge of the bilayer ( $p_3$ ) respectively. For the droplet radius (green,  $r_{\text{droplet}}$ ), a circle intersecting 3 points ( $p_1$ ,  $p_4$ ,  $p_3$ ) was drawn, corresponding to the left intersection with the bilayer ( $p_1$ ), the edge opposite the bilayer ( $p_4$ ), and the right intersection with the bilayer respectively ( $p_3$ ). **A)** Shows an asymmetric bilayer and **B)** shows a symmetric bilayer. The relative curvature was calculated by the following method for each droplet pair at 4 min:

$$\text{Relative curvature} = \frac{r_{\text{droplet}}}{r_{\text{bilayer}}}$$



**Figure C.3: Bilayer size measurements.** **A)** Method for measuring bilayer length in asymmetric and blend DIBs. Bilayer length was calculated by creating a circle (blue) that intersects 3 points ( $p_1$ ,  $p_2$ ,  $p_3$ ) corresponding to the left edge ( $p_1$ ), center ( $p_2$ ), and right edge ( $p_3$ ) of the bilayer respectively to find the radius ( $r_{bilayer}$ ) of the bilayer. From the center of the circle, the angle ( $\theta_{arc}$ ) between point  $p_1$  to point  $p_3$  was measured. The bilayer's length ( $l_{bilayer}$ ) was then calculated as the length of an arc (green) using:  $l_{bilayer} = \frac{2\pi r_{bilayer} \theta_{arc}}{360^\circ}$ . **B)** Method for measuring bilayer length (orange,  $l_{bilayer}$ ) in symmetric DIBs. Bilayers were approximately linear, and were therefore measured as a line segment from the left to the right edge of the bilayer. The bilayer area ( $A_{bilayer}$ ) was subsequently calculated from bilayer length ( $l_{bilayer}$ ) obtained by either method as an oval with a height equal to that of the microfluidic device channel ( $h_{channel}$ ):  $A_{bilayer} = \pi l_{bilayer} h_{channel}$ . Bilayer area was determined at 0 min, 1 min, 6 min, and 11 min, based on the most rapid rate of change in bilayer area occurring during the first minute of each experiment. The bilayer area at time points between these were calculated by linear interpolation.

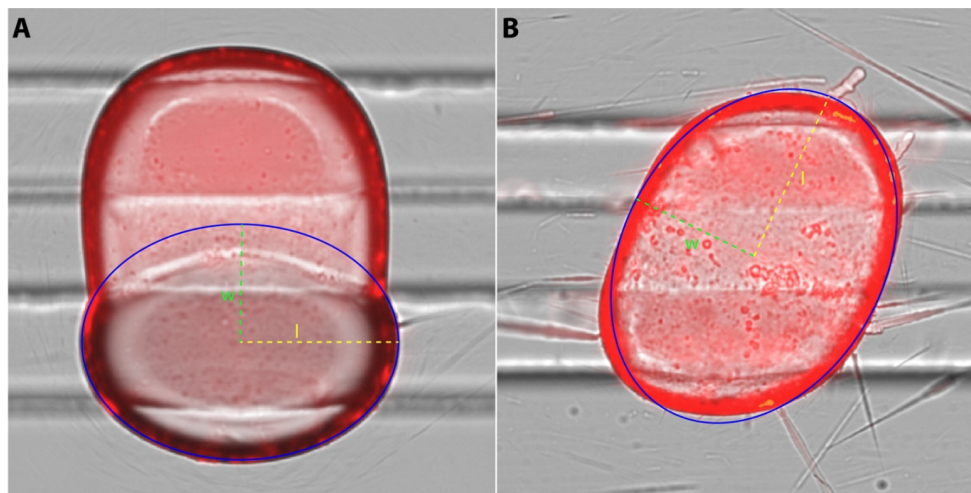


Figure C.4: **Droplet volume measurements.** **A)** Method for calculating droplet volume ( $V_{droplet}$ ) in asymmetric and blend DIBs. Acceptor droplet dimensions were measured as an oval (blue) with width  $w$  (green) and length  $l$  (yellow). The volume was then calculated as an ovoid with a height equal to the channel height ( $h_{channel}$ ) using:  $V_{droplet} = \frac{4}{3}\pi lwh_{channel}$ . **B)** Method for measuring droplet volume ( $V_{droplet}$ ) in symmetric DIBs. The dimensions of the entire droplet pair were measured with an oval with width  $w$  (green) and length  $l$  (yellow). The acceptor droplet volume (bottom droplet) was then calculated as half of an ovoid with a height equal to the channel height ( $h_{channel}$ ) using:  $V_{droplet} = \frac{4}{3}\pi lwh_{channel}$ . Droplet volumes were determined at 1 min, 6 min, and 11 min. The volume at 0 min was treated as the same as at 1 min. The change in volume over the first minute is negligible compared to the measurement error. The droplet volume at time points between those determined were calculated by linear interpolation.

### C.3 Time lapses of bilayer curvature

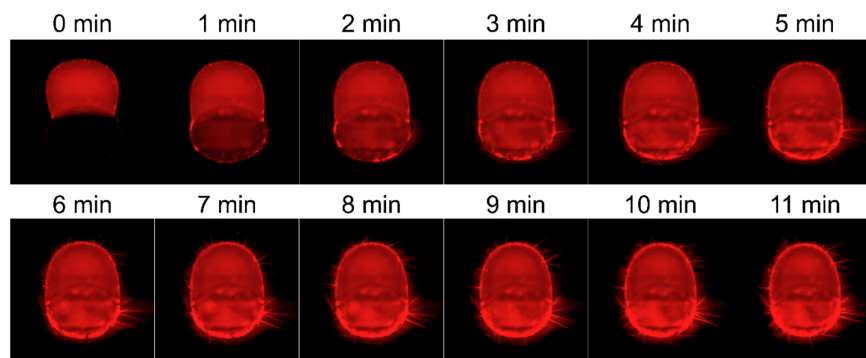


Figure C.5: **Evolution of asymmetric bilayer curvature over time.** Time lapse of diffusion and bilayer curvature for asymmetric DIBs, as shown in Figure 5.3. Bilayer size and curvature change as the bilayer equilibrates over the first 4 min. Following complete bilayer equilibration, bilayer curvature does not change.

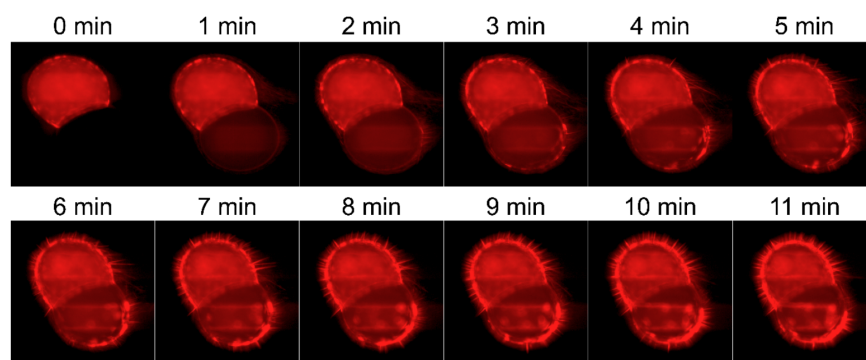


Figure C.6: **Evolution of blend bilayer curvature over time.** Time lapse of diffusion and bilayer curvature for blend DIBs, as shown in Figure 5.3. Bilayer size and curvature change as the bilayer equilibrates over the first 4 min. Following complete bilayer equilibration, bilayer curvature does not change.



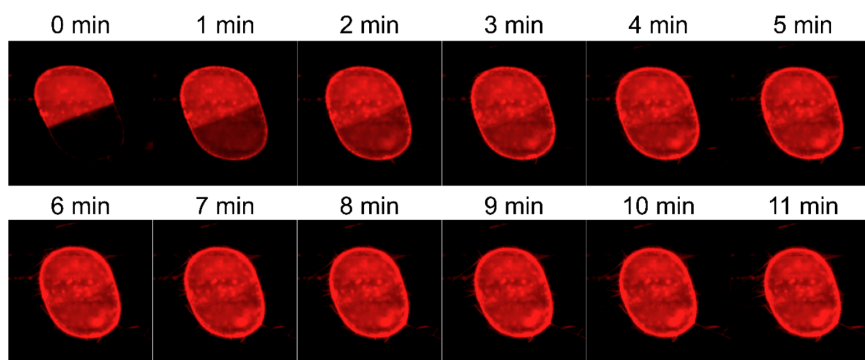


Figure C.7: **Evolution of symmetric bilayer curvature over time.** Time lapse of diffusion and bilayer curvature for symmetric DIBs, as shown in Figure 5.3. Bilayer size and curvature change as the bilayer equilibrates over the first 4 min. Following complete bilayer equilibration, bilayer curvature does not change.

Table C.2: **Interfacial tension data for lipid solutions.** Data was collected on a DataPhysics TBU 90E goniometer by the pendant drop method using two liquid phases. The droplet phase was the buffer solution, and the surrounding phase was the lipid mixture in squalene. Droplets were allowed to equilibrate for 5 min before image capture. Surface tension was calculated from pendant drop images using OpenDrop 3.3.0 (n = 3 in all cases).

Bilayer type	Outer leaflet interfacial tension (mN/m)	Inner leaflet interfacial tension (mN/m)
Asymmetric	$0.789 \pm 0.006$	$15.567 \pm 1.012$
Blend	$0.781 \pm 0.001$	$4.190 \pm 2.016$
Symmetric	$0.785 \pm 0.026$	

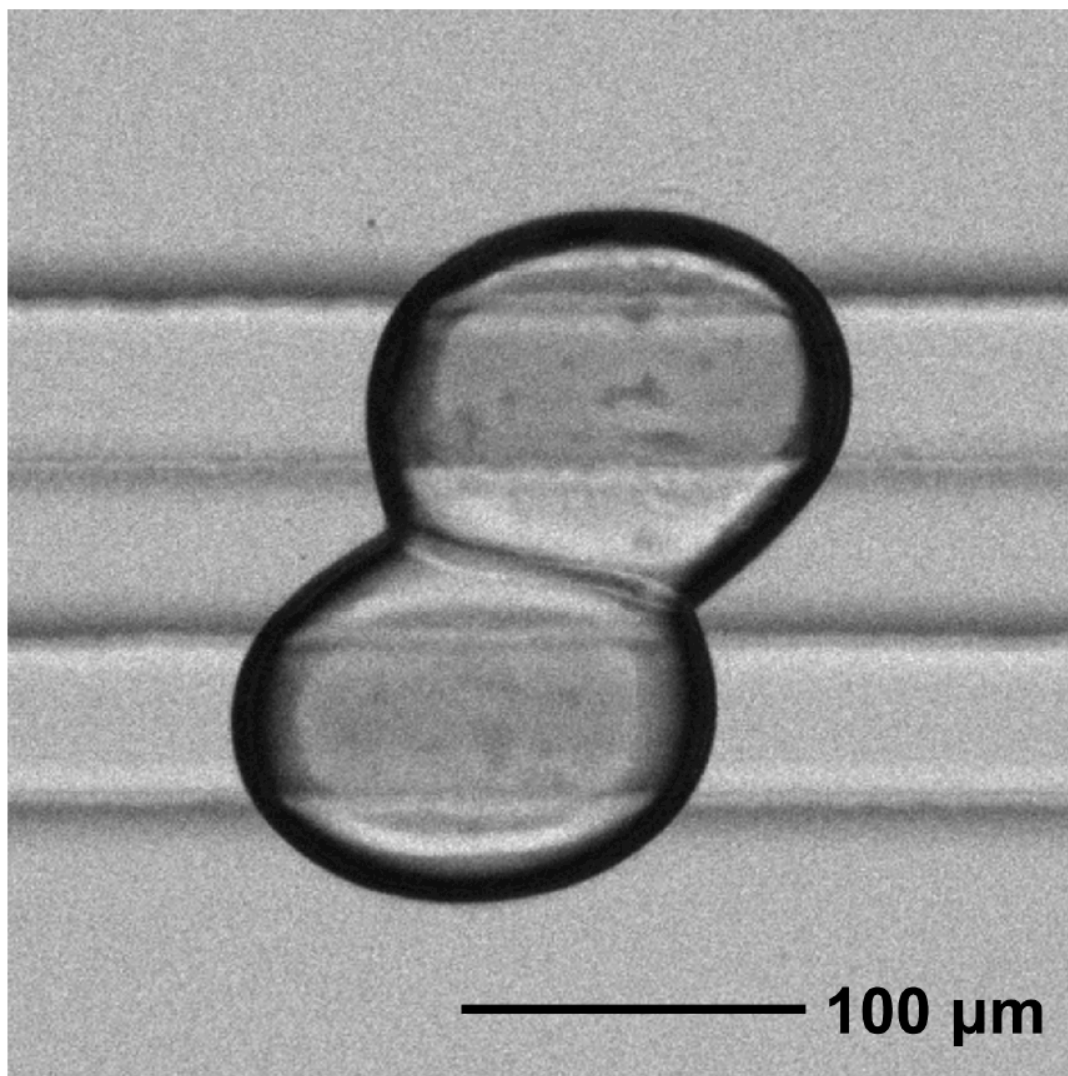


Figure C.8: **Effect of SM on bilayer curvature.** Representative image showing that an asymmetric distribution of PE (which occupies a conical space) and DOPC (which occupies a cylindrical space) was insufficient to drive formation of bilayers exhibiting curvature. Outer leaflet concentration (top droplet) was  $2015 \mu\text{g mL}^{-1}$  DOPC,  $830 \mu\text{g mL}^{-1}$  PE and  $210 \mu\text{g mL}^{-1}$  CHOL. Inner leaflet concentration (bottom droplet) was  $830 \mu\text{g mL}^{-1}$  DOPC,  $2015 \mu\text{g mL}^{-1}$  PE and  $210 \mu\text{g mL}^{-1}$  CHOL.

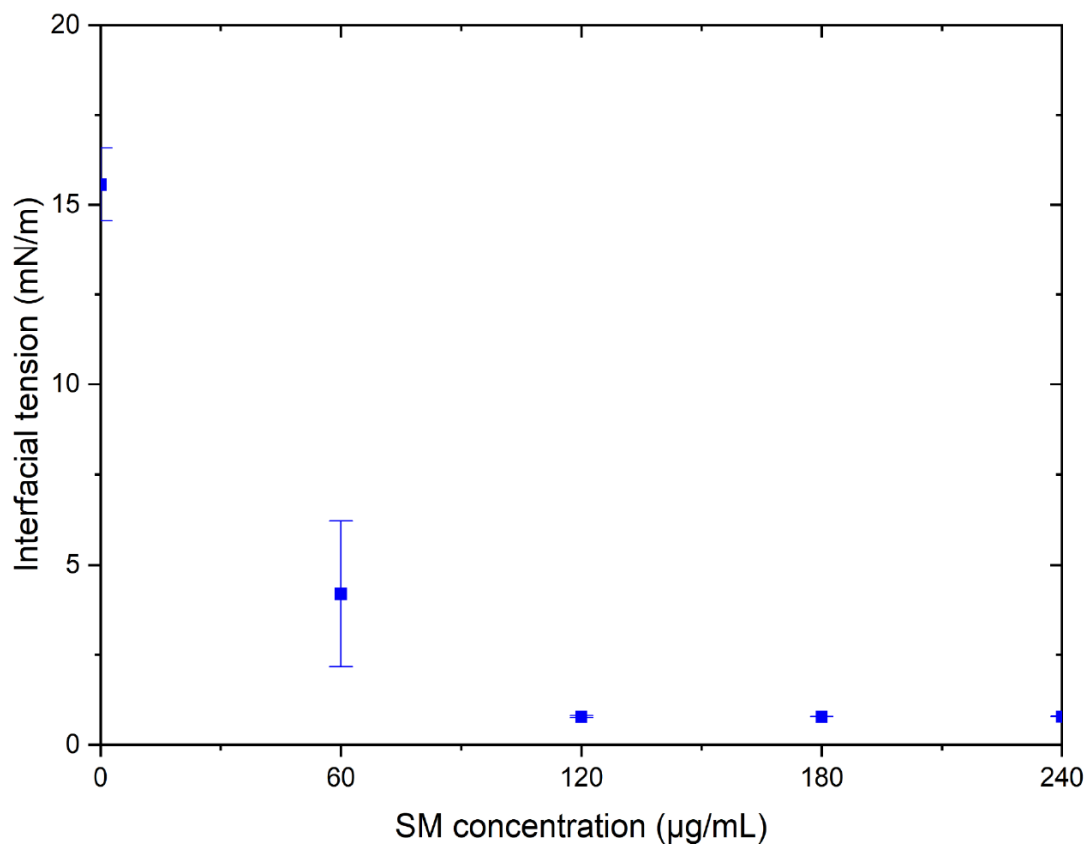


Figure C.9: **Relationship between interfacial tension and SM concentration.** SM appears to be the largest contributor to the curvature exhibited by asymmetric and blend DIBs, and this appears to be driven by the profound drop in interfacial tension found when using even small amounts of SM. The contribution of PC and PE ratios to the changing interfacial tensions were ignored based on the lack of curvature in asymmetric bilayers seen in Figure C.8.

## C.4 Original fluorescence images

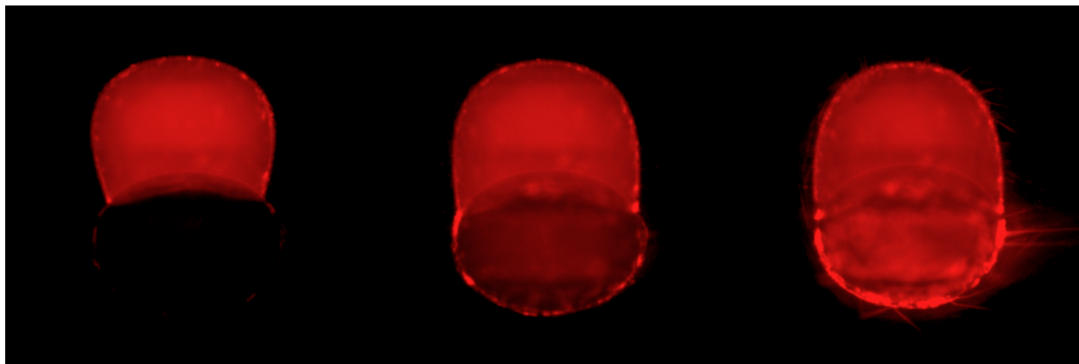


Figure C.10: **RGB images for the asymmetric bilayers shown in Figure 5.3.** In the original figure, a conversion from RGB to CMYK colourspace has been applied. For scale and annotations, see Figure 5.3 in the main text. From left to right: 0 min, 1 min, 4 min.

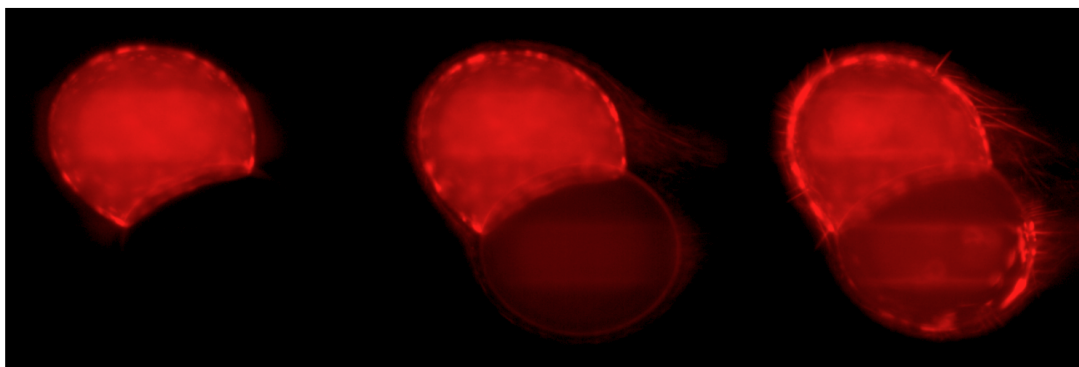


Figure C.11: **RGB images for blend bilayers shown in Figure 5.3.** In the original figure, a conversion from RGB to CMYK colourspace has been applied. For scale and annotations, see Figure 5.3 in the main text. From left to right: 0 min, 1 min, 4 min.

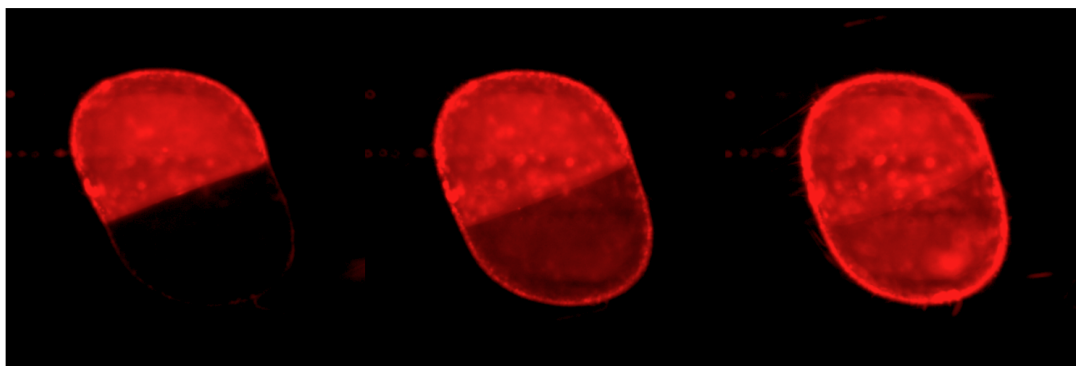


Figure C.12: **RGB images for symmetric bilayers shown in Figure 5.3.** In the original figure, a conversion from RGB to CMYK colourspace has been applied. For scale and annotations, see Figure 5.3 in the main text. From left to right: 0 min, 1 min, 4 min.

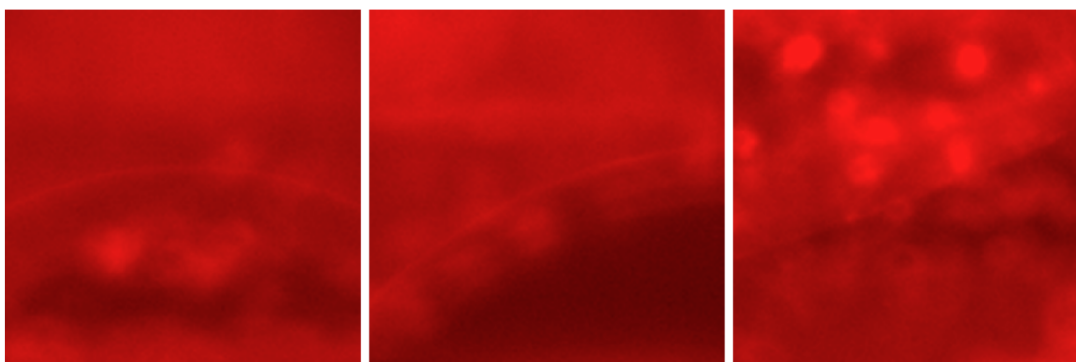


Figure C.13: **Original RGB images for expansions shown in Figure 5.3.** In Figure 5.3, a conversion from RGB to CMYK colourspace has been applied. Post processing for visibility was also applied in Figure 5.3, with brightness decreased and contrast increased. For scale and annotations, see Figure 5.3 in the main text. From left to right: asymmetric, blend, symmetric.

## C.5 Fluorescence intensity measurements and flux calculations

For measurement of fluorescence intensity, a noise-free region of interest was selected on the acceptor droplet. This was preferentially selected on the rail, but if not possible, a point between the rails was selected. The intensity for each time point ( $I_t$ ) was normalised ( $I_{norm,t}$ ) by subtracting the background (intensity at  $t = 0$ ,  $I_0$ ), and scaling by the droplet volume at time  $t$  ( $V_t$ ) over initial droplet volume ( $V_0$ ) to account for changes in concentration due to evaporation:

$$I_{norm,t} = \frac{(I_t - I_0)V_t}{V_0}$$

Percent absorbed was calculated for the normalized intensity at each time point ( $I_{norm,t}$ ) as a fraction of the peak normalized intensity ( $I_{norm,max}$ ). Absorbed percentage was converted to concentration ( $C_t$ ) by multiplying by the estimated concentration at equilibrium (0.5 mM due to the initial donor droplet concentration of 1 mM, and the equivalent donor and acceptor droplet volumes):

$$C_t = \frac{I_{norm,t}}{I_{norm,max}} 0.5mM$$

To calculate flux for each time point ( $J_t$ ), the rate of concentration change from that time ( $C_t$ ) to the next time point ( $C_{t+1}$ ) was calculated. This in turn was divided by

the bilayer area at that time ( $A_t$ ) and the size of the time step ( $\Delta t$ ):

$$J_t = \frac{C_{t+1} - C_t}{(A_t \Delta t)}$$

A curve was fitted to concatenated flux data from all replicates for each experimental condition (asymmetric, blend, symmetric). The data was fitted to a first order exponential decay in OriginPro 2021 of the form:

$$y = y_0 + A_1 e^{-x/t_1}$$

Where  $y_0$  is the offset from baseline,  $A_1$  is the initial value before offset,  $x$  is the time, and  $t_1$  is the mean lifetime. Peak flux, or initial flux ( $J_{max}$ ) for each experimental condition was calculated from the fitted equation as:

$$J_{max} = y_0 + A_1$$

Calculated flux ( $J_t$ ) is highly dependent on bilayer size, dependent upon droplet volume ratios from donor to acceptor, and to a lesser extent dependent on volume changes over time. Hence we normalise for this in our data analysis. However, the larger error calculated in  $P_{app}$  and curvature for the blend bilayers may be due to the larger degree of variability observed in interfacial tension measurements for the inner leaflet of these blend bilayers (see Table C.2). This may be due to improper membrane



packing.

## **C.6 Acknowledgements**

Dr Elvira's position is funded through the Canada Research Chair program and the Michael Smith Foundation for Health Research Scholar program in partnership with the Pacific Alzheimer Research Foundation. Funding for this work was provided through the Natural Sciences and Engineering Research Council of Canada (NSERC) Discovery Grant program, the Canada Foundation for Innovation John R. Evans Leaders Fund (CFI-JELF), the British Columbia Knowledge Development Fund (BCKDF), and the NSERC Research Tools and Instruments program. We would like to thank Dr Ned Djilali for use of his lab space and equipment for carrying out interfacial tension measurements.